Ph.D. DISSERTATION

High On/Off Ratio Devices with Broadband Photoresponse based on Surface Functionalized and Defect Controlled Optoelectronic Materials

By

Kootak Hong

August 2018

SEOUL NATIONAL UNIVERSITY

COLLEGE OF ENGINEERING

DEPARTMENT OF MATERIALS SCIENCE AND ENGINEERING

High On/Off Ratio Devices with Broadband Photoresponse based on Surface Functionalized and Defect Controlled Optoelectronic Materials

Advisor: Prof. Ho Won Jang

by

Kootak Hong

A thesis submitted to the Graduate Faculty of Seoul National University in partial fulfillment of the requirements for the Degree of Doctor of Philosophy

Department of Materials Science and Engineering

August 2018

Approved

by

Chairman of Advisory Committee: Miyoung Kim

Vise-Advisory Committee: Ho Won Jang

Advisory Committee: Jin Young Kim

Advisory Committee: Chong-Yun Kang

Advisory Committee: Soo Young Kim

Abstract

High On/Off Ratio Devices with Broadband Photoresponse based on Surface Functionalized and Defect Controlled Optoelectronic Materials

Kootak Hong

Department of Materials Science and Engineering

The Graduate School

Seoul National University

Photodetectors, which convert optical signals into electrical signals, are essential components for various fields. Recently, broadband photodetection from ultraviolet (UV) to near infrared (NIR) become central to modern science and technology, as the light with a wavelength of 400 nm to 1000 nm has notable advantages such as harmless characteristics, free frequency usage fee, high transmission rate, and high transmission capacity. However, it is difficult to develop high performance broadband photodetectors due to the lack of proper materials which have the ability

to absorb of incident radiation over broad wavelength range with excellent optoelectronic transfer efficiency and high reliability. In this respect, careful investigation of methods for how materials can show high on/off ratio under the wide range of wavelength should be carried out for developing high performance broadband photodetector. Therefore, this study focuses on design of high on/off ratio devices with broadband photodetection from UV to NIR to develop high performance and reliable broadband photodetectors.

By surface functionalization, Ag-decorated vanadium dioxide (VO_2) nanorod arrays (NRs)-based broadband photodetector are realized experimentally. Efficient broadband photodetection via localized surface plasmon resonance (LSPR) assisted photo-induced metal-insulator transition (MIT) occurs in Ag-decorated VO_2 NRs. The porous nanostructure can enable VO_2 to have a high specific area to be illuminated and to be well-decorated with Ag nanoparticles along the whole surface. Due to LSPR, strong electromagnetic coupling, which occurs at the interface between Ag nanoparticles and VO_2 NRs, provokes daylight-induced MIT in VO_2. MIT-driven broadband photodetection with the high response has not been observed in bare VO_2 dense planar thin films and this will open up the new strategy for a new functionalization in strongly correlated materials.

By controlling of defect migration, reliable high On/Off ratio ($I_{on}/I_{off} = 10^4$) $CH_3NH_3PbI_3$ broadband photodetectors with transport layer-free simple metal/semiconductor/metal lateral structure are demonstrated. At high external bias, low On/Off ratios and spikes in dark current and photocurrent are observed due to the charged defect migration. The charged defect migration can be effectively inhibited at low external bias, and thus the $CH_3NH_3PbI_3$-based photodetectors show

high I_{on}/I_{off} ratios and spike-free dark current and photocurrent. In addition, prevention of the prepoling in the $CH_3NH_3PbI_3$ films by operating at the low external bias results in pronouncedly enhanced signal-to-noise ratios even under low intensity incident light. These results strongly propose that inhibiting the migration of charged defect ions in $CH_3NH_3PbI_3$ films is a key in developing reliable high performance $CH_3NH_3PbI_3$-based devices.

Our approaches to enhance broadband photodetection performance of devices will open up the way to future devices. This study serves as a valuable proof-of-concept for next generation optoelectronic devices with fast response, low power consumption, high performance. and high relibility.

Keywords: Broadband photodetector, Vanadium dioxide, Metal-insulator transition, Plasmonic nanoparticles, Surface Functionalization, Hybrid perovskite, Defect ion migration, Hysteresis

Student Number: 2013-20632

Table of Contents

Abstract i

Table of Contents iv

List of Tables vii

List of Figures viii

Chapter 1 1

1.1. Background 1

1.2. Objectives of this study 3

Chapter 2 5

2.1. Introduction to photodetectors 6

2.1.1. The electromagnetic spectrum 8

2.2.2. Basic working principles of photodetection 11

2.2.3. Device architectures 15

2.2.4. Figure of merit parameters for photodetector 19

2.2. Current issues in photodetectors 24

2.2.1. Limits of conventional photodetectors and previous studies 24

2.2.2. Broadband photodetectors 27

2.3. Reference 33

Chapter 3 38

3.1. Introduction 39

3.2. Experimental procedures 45

3.2.1. Film preparation and device fabrication 45

3.2.2. Film characterization 45

3.2.3. Finite-difference time-domain (FDTD) simulation 46

3.2.4. Device characterization 46

3.3. Results and Discussion 50

3.3.1. Morphology of Ag-decorated VO_2 nanorod arrays 50

3.3.2. Electrical properties of Ag-decorated VO_2 nanorod arrays 53

3.3.3. Finite-difference time domain simulations 60

3.3.4. Enhanced broadband photoresponse performance of Ag-decorated VO_2 nanorod arrays and photo-induced metal-insulator transition 67

3.4. Conclusion 92

3.5. Reference 93

Chapter 4 101

4.1. Introduction 102

4.2. Experimental procedures 109

4.2.1. Materials preparation 109

4.2.2. Device fabrication 109

4.2.3. Device characterization 110

4.3. Results and Discussion 113

4.3.1. Device fabrication and optimization 113

4.3.2. Figure of merits of Pt/$CH_3NH_3PbI_3$/Pt photodetector 120

4.3.3. *I-V* hysteresis 127

4.3.4. Transient photoresponse characteristics 135

4.3.5. Poling effect 139

4.3.6. Schematic illustration of mechanisms 143

4.4. Conclusion 148

4.5. Reference 149

Chapter 5.....154

Summary.....154

List of Publications.....156

List of Presentation 158

Abstract (in Korean) 160

List of Tables

Table 3.1. Comparison of the figure-of-merits for broadband photodetectors and vanadium oxide based photodetector from previous reports and the present work.83

Table 3.2. Comparison of the power consumption per unit area and switching time of smart windows. 85

Table 4.1. Comparison of the device performances, including responsivity and detectivity, between our lateral MSM structure and previously reported lateral structured devices. The performances of our device are comparable to previously reported lateral structured ones. 126

List of Figures

Figure 2.1. Photodetectors convert optical signals into electrical signals. (a) Various commercial photodetectors (b) Typical phototransient curve of photodetectors.....6

Figure 2.2. Schematic of various applications of photodetectors. Figure from Ref. [8]. 7

Figure 2.3. Electromagnetic spectrum 10

Figure 2.4. The wavelength of light used by each application. Figure from Ref. [9]. 10

Figure 2.5. Excitation transition in photodetectors. (a) Interband transition from the valence band to the conduction band (b) Impurity to band transition (c) Intersubband 14

Figure 2.6. Schematic illustration for device architecture and typical band diagram when each device is under illumination: (a) photodiode, (b) phototransistor, and (c) photoconductor. Figures from Ref. [11-13]. 18

Figure 2.7. Definition of response time and recovery time 23

Figure 2.8. Definition of linear dynamic range (LDR).....23

Figure 2.9. Detectivity curves for various commercial photodetector. Figure from Ref. [15].....26

Figure 2.10. Broadband photodetector can detect spectral ranges from UV to NIR convert optical signals into electrical signals. 31

Figure 2.11. Application of Broadband photodetectors and broadband photodetector market size.....31

Figure 2.12. Band gap of various semiconductors materials. There are few materials that can absorb NIR with high optoelectronic transfer efficiency. 32

Figure 3.1. Schematic diagram showing electronic and structural degrees of freedom and novel physical phenomena. Transition metal oxides show metal-insulator transition, superconductivity, and ferroelectricity due to incompletely filled *d*- or *f*-orbitals. Figures from Ref. [31-34].....42

Figure 3.2. Materials exhibiting MIT and their critical temperature for MIT. Figure from Ref. [35].....42

Figure 3.3. Band structure and electrical resistance of vanadium dioxide (VO_2) before and after MIT. Figure from Ref. [36]. 43

Figure 3.4. Metal-insulator transition (MIT) driven by various external stimuli. Figures from Ref. [37-39].....43

Figure 3.5. Schematic illustration for localized surface plasmon resonance. 44

Figure 3.6. Glancing angle deposition method using electron beam evaporator. ...48

Figure 3.7. Measurement set-up for photoresponse of devices. 49

Figure 3.8. Schematic illustration for the fabrication process of Ag-decorated porous VO_2 nanorod arrays (NRs) 52

Figure 3.9. (a) Cross-sectional SEM and (b) TEM images of the Ag-decorated porous VO_2 NRs. (c) High magnification TEM image of an Ag nanoparticles on a

VO_2 nanorod. (e) Selected area diffraction pattern of the VO_2 NRs. 52

Figure 3.10. (a) Normalized electrical resistance of the devices as a function of bias (b) Electrical resistance of the devices as a function of bias. 56

Figure 3.11. (a) Dark *I-V* characteristics of Ag-decorated porous VO_2 NRs and (b) double logarithmic and (c) log(I/V) versus $V^{1/2}$ plots of the dark *I-V* curve. 57

Figure 3.12. (a) Schematic diagram of devices. Thermographic images of the Ag-decorated porous VO_2 NRs at various applied external biases. (b) 0 V, (c) 1 V, (d) 2 V, (e) 3 V, (f) 5 V, (g) 7 V, and (h) 10 V 58

Figure 3.13. (a) Electrical resistance of the Ag-decorated porous VO_2 NRs as a function of temperature, measured with external biases of 1 V and 5 V. (b) Derivative of the resistance vs. temperature plot for applying external bias at 1 V and 5 V.....59

Figure 3.14. Top view of electric field distribution Ag NP/VO_2 systems under the incident light of wavelength (a) 405 nm, (b) 663 nm, and (c) 1000 nm. Cross-sectional view of electric filed distribution Ag NP/VO_2 systems under the incident light of wavelength (d) 405 nm, (e) 663 nm, and (f) 1000 nm. 64

Figure 3.15. (a) Electric field distribution in the Ag-decorated porous VO_2 NRs and (b) the Ag-decorated dense planar VO_2 thin films. TEM images of (c) Ag-deocrated porous VO_2 NRs and (d) Ag-decorated VO_2 dense planar thin films used for FDTD simulations.....65

Figure 3.16. Simulated transmittance spectra from 200 nm to 1600 nm. 66

Figure 3.17. (a) *I-V* characteristics of the Ag-decorated porous VO_2 NRs under various intensities of white light. (b) The photocurrent of Ag-decorated porous VO_2

NRs measured with external bias of 10 V plotted as a function of light intensity. The graph is fitted by the power law $I_{photo} \propto L_{light}^{0.51}$ 78

Figure 3.18. The dark and photo *I-V* characteristics under the illumination of white light 5 mW cm^{-2}: (a) Bare dense planar VO_2 thin film, (b) Ag-decorated dense planar VO_2 thin film, and (c) bare porous VO_2 NRs. 79

Figure 3.19. The R_{dark}/R_{photo} of the devices as a function of light intensity.....80

Figure 3.20. (a) The transient photocurrent of our devices with incident light of various wavelengths. (b) Spectral responsivity and EQE of the device based on the Ag-decorated porous VO_2 NRs. 81

Figure 3.21. (a) The responsivity, (b) external quantum efficiency, and (c) detectivity of the Ag-decorated porous VO_2 NRs under 532 nm laser illumination as a function of light intensities. (d) Time resolved photoresponse of the Ag-decorated porous VO_2 NRs. 82

Figure 3.22. (a) Photo-switching characteristics of the device under alternating dark and light illumination (white light, 5 mW cm^{-2}). (b) The long-term stability test of the Ag-decorated porous VO_2 NRs in air for 200 days. 84

Figure 3.23. (a) The *I-V* characteristics of the Ag-decorated VO_2 porous NRs in various gas ambient. (b) The photo transient curve of the Ag-decorated porous VO_2 NRs in gas various ambient. 84

Figure 3.24. The resistance of the Ag-decorated porous VO_2 NRs with thickness of 250 nm in the dark and under the illumination as a function of temperature. 86

Figure 3.25. Top view and cross-sectional view SEM images of Ag-decorated porous VO_2 NRs deposited less than 100 nm. The completely destroyed nanostructure of Ag-decorated porous VO_2 NRs were observed. Dark and photo *I-V* characteristics of 100 nm thick of (c) Ag-decorated porous VO_2 NRs and (d) SiO_2/Si substrate.....87

Figure 3.26. Top and cross-sectional view SEM images of Ag-decorated porous VO_2 NRs. (a,b) 150 nm, (c,d) 250 nm, (e,f) 350 nm, and (g,h) 700 nm-thick Ag decorated porous VO_2 NRs. 88

Figure 3.27. The R_{dark}/R_{photo} of the devices with the thicknesses of Ag-decorated porous VO_2 NRs ranging from 150 nm to 700. 89

Figure 3.28. (a) A typical high magnification TEM image of VO_2 nanorod and (b) Monoclinic M_1 $\mathbf{011}$ (red rectangle) zone axis FFT. (c) A typical high magnification TEM image of Ag-decorated VO_2 nanorod. (d) Tetragonal R$\mathbf{111}$ (orange rectangle) zone axis FFT. 90

Figure 3.29. Schematics for the electronic structure of the Ag-decorated porous VO_2 NRs (a) in the dark and (b) under the illumination.....91

Figure 4.1. Crystal structure of halide perovskite (ABX_3). 104

Figure 4.2. Schematic diagram showing the various application of halide perovskites. Figures from Ref. [27-31].....105

Figure 4.3. Optical properties of halide perovskites: (a) high absorption coefficient and light harvesting characteristics (b) good band alignment with TiO_2 and Au in photovoltaic devices, (c) long carrier diffusion length (d) fast carrier mobility (e, f)

slow recombination rate. Figures from Ref. [32-36]. 106

Figure 4.4. Power conversion efficiency deteriorate in solar cell by defect migration. Figures from Ref. [19, 23]. 107

Figure 4.5. (a) Schematics of ion drift in perovskites during positive and negative poling, respectively, showing that the accumulation of ions in the perovskite near the electrodes induced p- and n-doping. (b), Energy diagram of the p–i–n structure after poling (WF = work function). (c) Calculated migration path indicating a slightly curved path and local relaxation/tilting of the octahedra. (d) Calculated activation energies for ionic defect migration in $CH_3NH_3PbI_3$. Figures from Ref. [15, 18]. . 108

Figure 4.6. Schematic illustration for fabrication process of $CH_3NH_3PbI_3$ ($MAPbI_3$) thin films and $CH_3NH_3PbI_3$ -based photodetector. 112

Figure 4.7. Measurement set-up for photoresponse of $CH_3NH_3PbI_3$-based photodetector. 112

Figure 4.8. Schematic diagram of $MAPbI_3$-based perovskite photodetector and crystal structure of $MAPbI_3$ perovskite. 115

Figure 4.9. XRD data from crystallized $MAPbI_3$ films annealed at various temperatures. The shapes and peak positions did not change significantly with crystallization, regardless of annealing temperature. 116

Figure 4.10. SEM images of crystallized $MAPbI_3$ film on SiO_2/Si wafer. The crystallization of the $MAPbI_3$ film was performed at annealing temperatures of (a) 70, (b) 90, (c) 110, and (d) 130 °C. 117

Figure 4.11. The AFM measurements of prepared $MAPbI_3$ with various annealing

temperatures. The root-mean square (RMS) roughness of the $MAPbI_3$ films annealed at (a) 70 °C (R_{rms} =103.87 nm) (b) 90 °C (R_{rms} =99 nm), (c) 110 °C (R_{rms} =76.71 nm), and (d) 130 °C (R_{rms} =118 nm), respectively. 118

Figure 4.12. Absorption spectra of $MAPbI_3$ film annealed at various temperatures. The absorption edge and the intensity of absorbance spectra are almost same for the all samples. 119

Figure 4.13. Device performance plotted against external bias. The highest on/off ratio was obtained at 0.1 V (lowest dark current and highest photocurrent). The highest detectivity was obtained at 1 V (relatively low dark current and high photocurrent). 123

Figure 4.14. The noise current analysis of the fabricated perovskite-based photodetector. The noise current shows the frequency-independent behavior in the dark, indicating that the shot noise was dominant in our fabricated devices. 124

Figure 4.15. (a) The response and recovery time analysis of the fabricated perovskite-based photodetectors. The response time and recovery time is shorter than 90 and 20 ms, respectively. (b) The stability test in rough vacuum condition over 14 days. (c) Photocurrent and responsivity properties with respect to wavelength.... 125

Figure 4.16. Dark and photocurrent hysteresis curves in (a) log scale and (b) linear scale with various sweep voltage rates. 131

Figure 4.17. (a) The flat-band diagram and equilibrium state of the $Pt/MAPbI_3/Pt$ device without external bias. (b) Schematic diagram of ion drift in the $MAPbI_3$ film with forward and reverse bias. The negatively charged defect ions make a p-type

self-doping region and the positively charged defect ions make an n -type self-doping region under the external electric field, result in p-i-n or n-i-p homojunctions.....132

Figure 4.18. (a) Dark and (b) photo *I-V* curves with different temperatures at a scan rate of 100 mV s^{-1}. The dark *I-V* clearly shows the temperature-dependent hysteretic behavior by electronic transport. The dark and photo *I-V* curves under (c) 123 K, (d) 139 K, (e) 161 K, (f) 190 K, (g) 232 K, and (h) 298 K. 133

Figure 4.19. The log (current density) plotted against 1000T to summarize the hysteric behavior of Figure 4.18. The higher current density values in reverse scan (5 → 0 V) originate from the formation of built-in potential. The hysteric behavior of photocurrent is negligible because the transport of photogenerated carrier is more dominant than electrical transport. 134

Figure 4.20. *I–t* characteristics of fabricated perovskite photodetector with various external biases. (a) Transient photocurrent plotted against time with various external biases. The dark current behavior at the beginning of each measurement with V_{ex} of (b) 0.1, (c) 0.2, (d) 0.3, (e) 0.4, (f) 0.5, (g) 1, (h) 3, (i) 5, and (j) 10 V. Significant spikes were revealed at 0.5–10 V.....137

Figure 4.21. (a) Multiple *I–t* characteristics of fabricated device in the dark and under illumination at various external biases. (b) Current behavior in the dark plotted against time is magnified data from (a). 138

Figure 4.22. Device characteristics both before and after poling. *I–t* curves (a) before poling with external biases of −0.1 and 0.1 V and (b) after poling (−1 and 1 V poling) with external biases of −0.1 and 0.1 V.....141

Figure 4.23. *I–t* characteristics both before and after poling at various incident light intensities and wavelengths. 142

Figure 4.24. Energy-band diagram of $MAPbI_3$-based photodetector (a) before poling in the dark, (b) before poling under illumination. The solid red dots and solid blue dots indicate the positively and negatively charged vacancies, respectively.....145

Figure 4.25. Energy-band diagram of $MAPbI_3$-based photodetector (a) After poling in the dark and (b) after poling under illumination. The solid red dots and solid blue dots indicate the positively and negatively charged vacancies, respectively.....146

Figure 4.26. Changes of built-in potential in the dark and under illumination.....147

Chapter 1

1.1. Background

From the beginning of time, light is essential to all living things in the Earth and mankind has wanted to control and use light for its convenient life. Optoelectronic devices, which can generate, detect, control, and interact with light, are the results of the desires. Among the optoelectronic devices, photodetectors, which can convert incident light into electrical signals, are essential electronic component used in various fields in our lives including imaging, communication, environmental monitoring, chemical/biological detection, day- and night-time surveillance. Therefore, for a photodetector with better performance, it has been extensively studied for decades.

Recently, with the advent of new technology, such as visible light communication, holographic data storage, the internet of things, there is an increasing demand for a device capable of broadband photodetection from ultraviolet to near-infrared (400~1000 nm), which is harmless to the human and enables high transmission rate and capacity. So far, previous reports on photodetectors were mainly related with special wavelength photodetectors. Therefore, studies on developing high performance broadband photodetectors are required. To detect light up to near-infrared region, the band gap of the active materials in photodetectors should be less 1.24 eV or less, but there are few materials exhibiting good optoelectronic transfer efficiency with good

reliable performance.

Although synthesizing new materials capable of broadband photodetection may be one possible way, this approach is complicated and has drawbacks in terms of cost, fabrication. Therefore, to design the photodetector with wide spectral sensitivity, different approaches are needed to expand the detectable wavelength range and obtain enhanced optoelectronic efficiency of materials.

1.2. Objectives of this study

This thesis focuses on design the high on/off ratio devices with broadband photodetection of incident light of wavelength from 400 nm to 1000 nm. For simple fabrication, low cost, and better investigation for physical properties of optoelectronic materials, the devices investigated in this thesis were fabricated in the form of photoconductor. In order to obtain higher broadband photoresponse performance, surface functionalization and defect control methods are employed. The enhanced and reliable photoresponse performance of the devices, which were investigated in this thesis, was studied systematically using various experiments including current-voltage (*I-V*) measurement, transient photocurrent measurement, x-ray diffraction (XRD), ultraviolet-visible (UV-Vis) photospectrometer, thermographic camera, scanning electron microscopy (SEM), transmission electron microscopy (TEM), atomic force microscopy (AFM) and finite-difference time domain (FDTD) simulations. These experimental results substantiate that high performance broadband photoresponse can be realized by surface functionalization and defects control. Based on these experimental results, high on-off ratio devices with broadband photodetection were developed.

Chapter 2 describes basic introduction to photodetectors and current issues in developing photodetectors. First, physical properties of light and working principle of photodetectors including photoelectric effect and photothermal effect will be discussed. And then, the device architecture and figure-of-merit parameters to evaluate the performance of photodetectors such as on/off ratio, responsivity, detectivity, external quantum efficiency will be presented. Finally, limits of

commercial photodetectors and previously studied photodetectors and current issues and a short review of developing higher performance broadband photodetectors will be discussed.

In Chapter 3, broadband photodetection by daylight-induced metal-to-insulator transition in Ag-decorated vanadium dioxide (VO_2) nanorod arrays are presented. With Ag nanoparticles (NPs) decoration, the electric fields are generated at the interface between Ag NPs and VO_2 under the illumination due to localized surface plasmon resonance (LSPR). The generated electric fields at the interface between Ag NPs and VO_2 NRs affect electronic state of VO_2, and thus, visible light-induced metal-to-insulator transition, which has not seen in dense planar VO_2 thin films, was observed in Ag-decorated VO_2 NRs. As the electric fields, which originate from LSPR, can be generated under a wide range of wavelengths, the MIT in Ag-decorated VO_2 NRs occurred under a wide range of wavelength. Therefore, broadband photodetection of Ag-decorated VO_2 NRs was available from 400 nm to 1000 .nm

In Chapter 4, reliable broadband photodetection performance of hybrid perovskite-based device are described. Due to the low activation energy for formation and migration of defects, hybrid perovskite-based devices suffer from performance degradation. With inhibition of ionic defect migration, hybrid perovskites-based devices show high on/off ratios and reliable photoresponse performance. Moreover, it is revealed that the electrical history of the device such as poling significantly affects device performance and should be controlled for reliable operation.

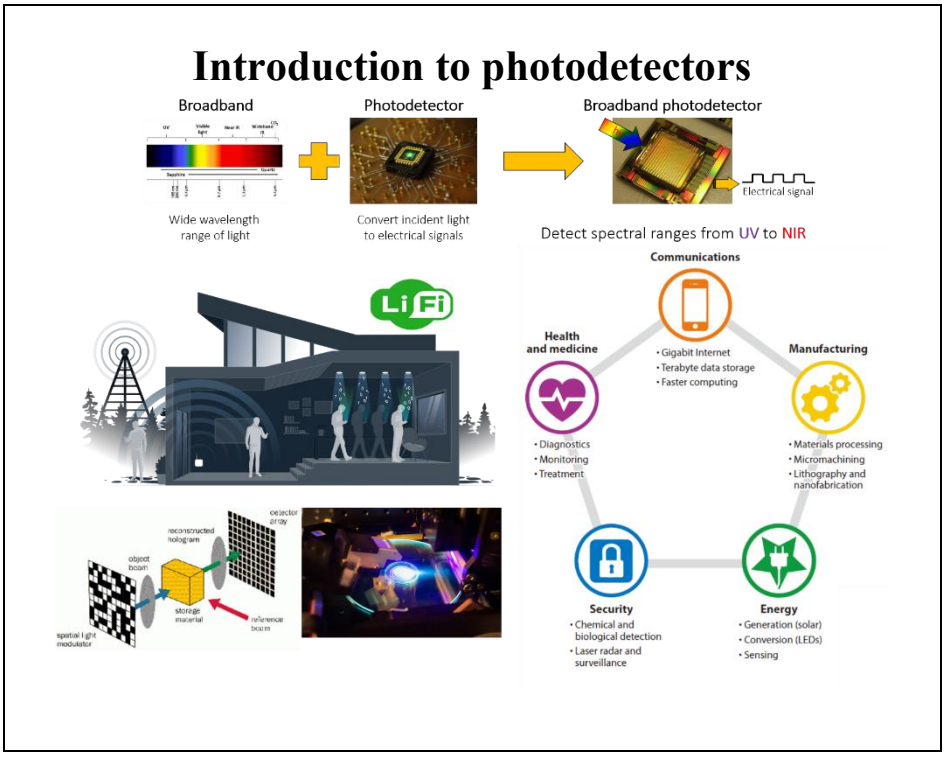
Introduction to photodetectors
Broadband
Photodetector
Broadband photodetector
Electrical signal
Wide wavelength range of light
Convert incident light to electrical signals
Detect spectral ranges from UV to NIR
LiFi
Communications
• Gigabit Internet
• Terabyte data storage
• Faster computing
Health and medicine
• Diagnostics
• Monitoring
• Treatment
Manufacturing
• Materials processing
• Micromachining
• Lithography and nanofabrication
Security
• Chemical and biological detection
• Laser radar and surveillance
Energy
• Generation (solar)
• Conversion (LEDs)
• Sensing
reconstructed hologram
object beam
storage material
reference beam
spatial light modulator

2.1. Introduction to photodetectors

Photodetectors, which convert light signals into electrical signals, are one of the essential and widely used electronic devices (Figure 2.1). They significantly affect our daily lives and can easily find widespread applications in industrial and scientific area including environmental monitoring, optical communications, remote control, missile defense, day- and night-time surveillance, chemical/biological sensing, and medical diagnosis (Figure 2.2).[1-5] Recently, as the internet of things, visible light communication, and data storage using light become core technologies for the future, photodetectors become more important since as they can supply enormous amounts of information about the environment and the state of the object.[6,7]

This section begins with the introduction to the classification, properties and applications of light. Then, the basic working principles of photodetection and device architecture are introduced. Finally, the figure of merit parameters that make it possible to evaluate the performance of photodetectors are discussed.

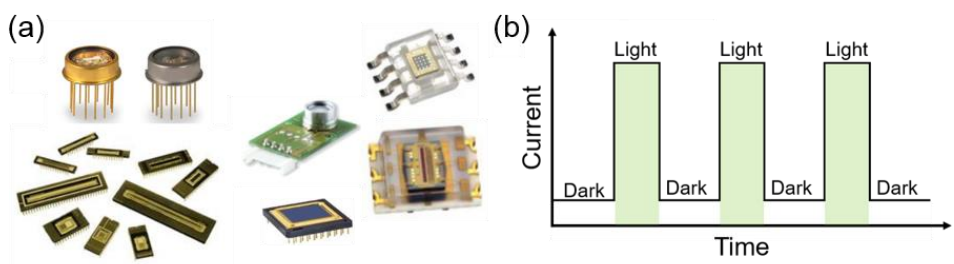

Figure 2.1. Photodetectors convert optical signals into electrical signals. (a) Various commercial photodetectors (b) Typical phototransient curve of photodetectors.

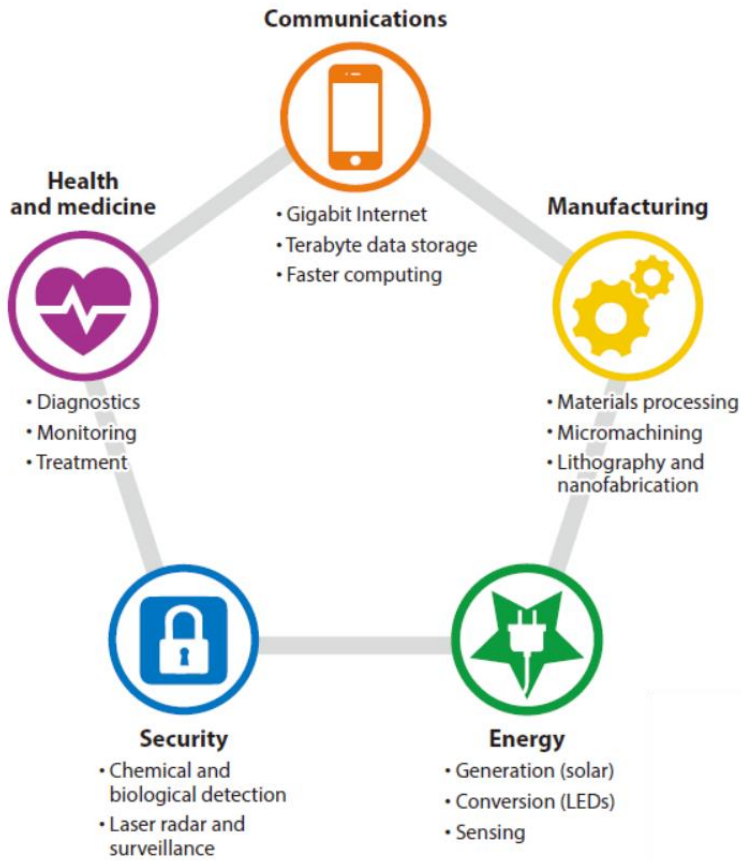

Figure 2.2. Schematic of various applications of photodetectors. Figure from Ref. [8].

2.1.1. The electromagnetic spectrum

There have been many efforts made for comprehensive description of light for centuries. In classical pictures of light, light is considered as a wave. Such phenomena as interference, diffraction, refraction, and reflection can be explained by the theory of waves. The electromagnetic wave consists of oscillating electric and magnetic fields which are perpendicular to direction of propagation, travelling at speed c in the direction normal to their plane of oscillation. The speed of light can be expressed as

$$c = \lambda\nu$$

where λ is the wavelength and ν is the frequency of oscillation.

However, photoelectric effect and Compton scattering can be explained by the wave of light, when light interacts with matter during absorption and emission. It becomes necessary to describe light as a group of indivisible quanta of radiation called photons, each travelling at speed c and have a distinct energy which can be expressed as

$$E = h\nu$$

where h is Planck's constant (6.63×10^{-34} Js, 4.14×10^{-15} eVs). In semi-classical picture of light, light consists of a large number of photons, and its properties and interaction with matter become a statistical calculation.

The visible light, which we use to see, is a very small part of electromagnetic waves. Electromagnetic waves are categorized by wavelengths into radio (10^8 nm), microwaves (10^6 nm), infrared (10^4 nm), visible (400-700 nm), ultra violet (10^2 nm),

x-rays (10^{-1} nm), and γ-rays (10^{-3} nm) as shown in Figure 2.3. When an electromagnetic wave have photon energy below 10^{-3} eV, wave-like behaviors are apparent in electromagnetic waves. Whereas, with decreasing of wavelength of electromagnetic waves, electromagnetic waves show more pronounced particle-like behaviors. Therefore, photodetectors for below IR regions use photoelectric effect, which are related with particle nature of electromagnetic waves, whereas photodetectors for above IR regions use photothermal effect, which are related with wave-like behavior of electromagnetic waves.

The electromagnetic waves have different properties depending on wavelength, such as how they interact with matters and their applications (Figure 2.4). For examples, radio waves are mainly used for communication and wireless coupling signal transmitting. Due to low attenuation losses in silica, infrared waves are used for fiber optic communication. Infrared radiation in fiber optics. X-rays and γ-rays are classified as ionizing radiation since their high energy photons can ionize atoms, causing chemical reactions. Although exposure to these rays in daily life can be very harmful, they are very useful in medical imaging and radiation therapy.[9]

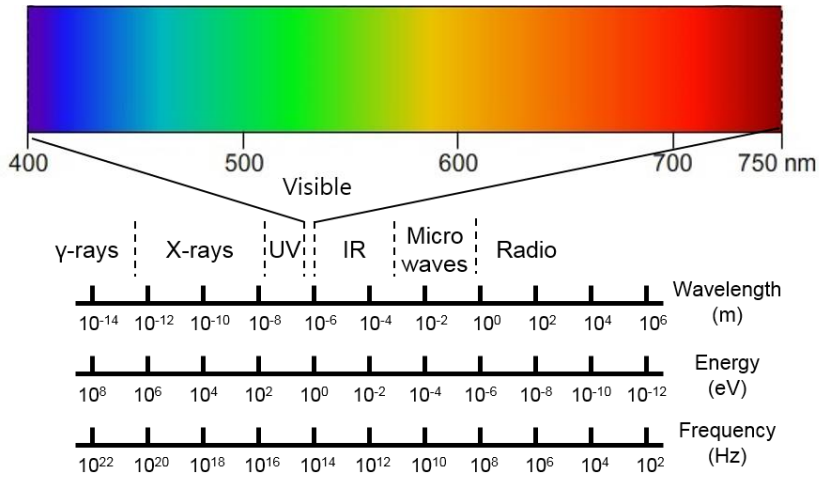

Figure 2.3. Electromagnetic spectrum

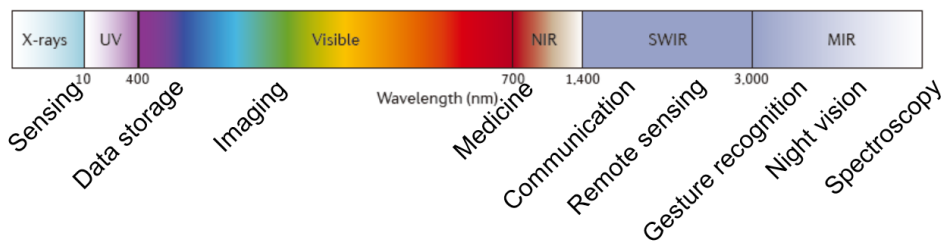

Figure 2.4. The wavelength of light used by each application. Figure from Ref. [9].

2.2.2. Basic working principles of photodetection

All the photodetectors make use of the effects of the interaction of light with materials. There are two main working principles how photodetectors detect light: photoelectric effects and thermal effects. While photodetectors based on photoelectric effects are mainly used for detecting from ultraviolet (UV) to near infrared (NIR) region, photodetectors based on photothermal effects are used for detecting far IR region.[10] In this section, working principles of photodetectors based on photoelectric effects and photothermal effects.

Working principles of photodetector based on photoelectric effects

The photoelectric effects means the direct interaction between photons and electrons in materials. The conversion process of photodetector based photoelectric effects can be divided in to three main steps.

1. Photosensitive materials in device (usually semiconductors) absorb the incident light (optical signal) and the carriers are generated.

2. The photogenerated carriers are transported into the electrodes. The transport of photogenerated carrier can be amplified depending on the device architecture.

3. The extracted carriers flow into the external circuit. The flow of photogenerated carriers are current which is the electrical signals converted from incident light.

To provoke photoelectric effect by incident light, an electronic transition should be occurred in photosensitive materials. The incident light can be detected by photon

detector, if its energy is larger than the energy of the relevant transition within the photosensitive materials in the device. The relation between detectable incident light and the energy of relevant transition can be expressed as

$$\lambda \leq \frac{hc}{\Delta E}$$

where λ is wavelength of incident light, h is Planck's constant, c is light velocity, and ΔE is the energy of the relevant transition. There are three representative transition and they can be explained with band structure of materials as shown in Figure 2.5. When photosensitive materials absorb the incident light which has photon energy larger than band gap, interband transition occurs in which electrons in valence band move into conduction band (Figure 2.5a). The conductivity changes resulting from interband are called intrinsic photoconductivity, as interband transition is related with intrinsic electrical properties, especially band gap energy. The photon energy less than band gap energy can induce electronic transition. When deep levels are generated by impurities, electrons can move from impurity level to either the valence band or conduction band. The impurity centers are trap sites that have the form of a free electron-bound hole or free hole-bound electron. The impurity states are typically shallow states located near from the opposite band edge (Figure 2.5b). Another possible transition is intersubband transition (Figure 2.5c). The electrons and holes are excited between the subbands within the conduction band. The conductivity changes due these transition are called extrinsic photoconductivity as external factors, such as impurity, doping concentration, morphology, influence the photoconductivity of materials.

Working principles of photodetector based on photothermal effects

While photon photodetectors are mainly used for detecting from UV to NIR region, thermal photodetectors are used for detecting far IR region as there is no a discrete energy cutoff in thermal effects. The operating mechanism of thermal photodetectors can be described as following: First, the incident light induces a temperature change in the active materials in thermal photodetectors. As the active materials in the device show temperature dependent electrical properties, the dissipated energy causes some other physical parameters to change. The photoresponse of thermal photodetectors is normally related to the intensity of the incident light, rather than wavelengths of incident light, as there is no a discrete energy cutoff in thermal effects.

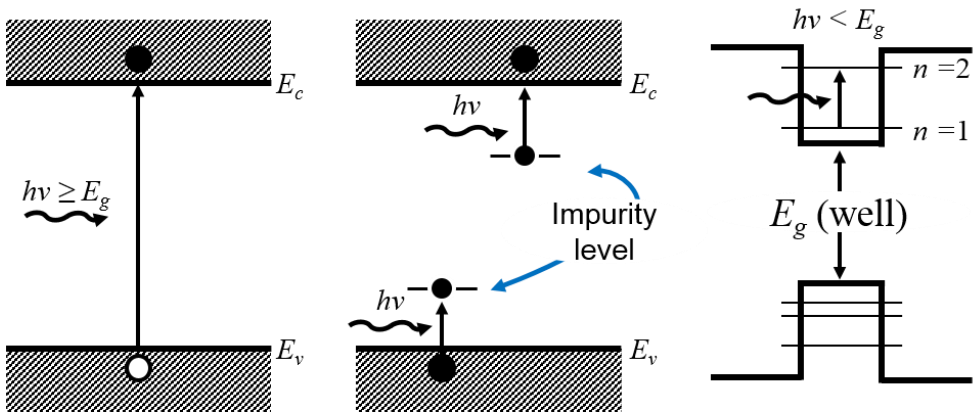

Figure 2.5. Excitation transition in photodetectors. (a) Interband transition from the valence band to the conduction band (b) Impurity to band transition (c) Intersubband

2.2.3. Device architectures

Based on the device architecture, photodetectors can be categorized into photodiodes, phototransistor, and photoconductor. Each type of photodetectors have their own operating mechanism due to the device architecture. In this section, device architectures of photodiodes, phototransistor, and photoconductor are described. Moreover, the operating mechanism, advantages and disadvantages depending on device architecture are also discussed.

Photodiode

Photodiodes are usually based on p-n or p-i-n junction. When photodiodes are illuminated, photogenerated carriers within depletion region are separated and transported to electrodes by built-in electric fields. Therefore, a photovoltaic-like vertical configuration is widely adopted as photogenerated carriers are easily separated and charge recombination can be reduced (Figure 2.6a). Photodiodes can be operated by low driving voltage and exhibit low dark current and fast response speed. However, the disadvantages of photodiodes are resulted from depletion region. Since depletion region is very narrow in photosensitive layer and it is significantly influenced by the doping concentration and impurities in photosensitive layer. The external quantum efficiency of photodiodes is normally less than 100 % due to the insufficient absorption of light and recombination of photogenerated carriers. As a point of fabrication, photodiodes have drawbacks. For the better separation of photogenerated carrier, photodiodes need charge transport layers, which are expensive and make fabrication process become difficult. Moreover, photodiodes

need expensive transparent electrodes, as incident light pass through the electrode when light enters the active layer.

Phototransistor

Phototransistors use the transistor gain action in conjuction with the carrier generation due to light absorption. To reduce the noise current and amplify the electrical signal, phototransistors have a gate electrode and a dielectric layer are added to the devices, as shown in Figure 2.6b. With reduced dark current and noise current, phototransistors exhibit enhanced figure of merit such as responsivity and gains. With incorporating with cheap and high mobility semiconductors, phototransistor can be fabricated easily. However, phototransistors exhibit a strongly exhibit a nonlinear response, slow response speed, and cannot detect light of weak intensity.

Photoconductor

Photoconductors are device whose resistance changes under the illumination. Compared with photodiodes and phototransistors, photoconductors have simple structure with the photosensitive channel between the two lateral metal electrodes, as shown in Figure 2.6c. The operating mechanism can be explained by photoconductive effect. When the photoconductor are under illumination, photogenerated carriers in the photosensitive channel are separated and collected by electrodes by external bias. Contrary to photodiodes and phototransistor, photoconductor can be fabricated easily due to the simple structure without

transparent electrodes and charge transport layers. With this simple structure, photoconductors are adopted in flexible optoelectronics and they have advantages as a point of materials selection. However, due to long channel length, photoconductors show slow photoresponse and low photosensitivity.

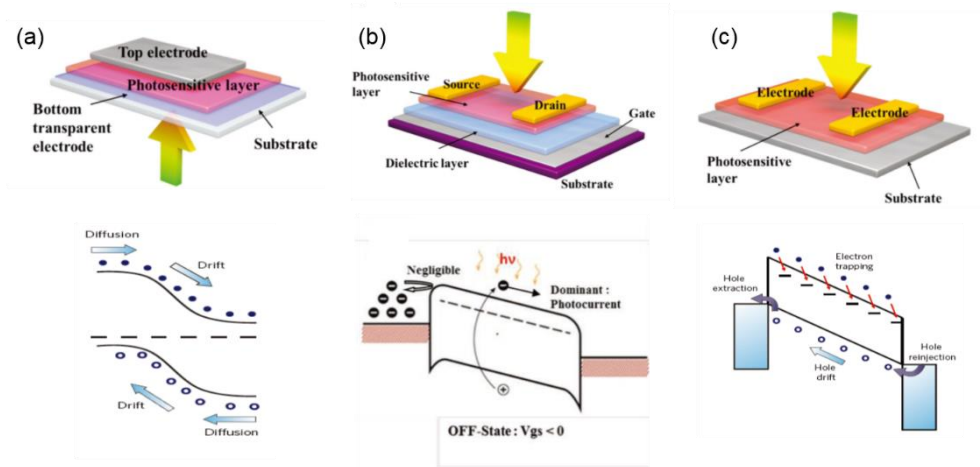

Figure 2.6. Schematic illustration for device architecture and typical band diagram when each device is under illumination: (a) photodiode, (b) phototransistor, and (c) photoconductor. Figures from Ref. [11-13].

2.2.4. Figure of merit parameters for photodetector

In order to evaluate photoresponse performance, several parameters are used. Although certain applications require different features, the most important and essential parameters for photodetector and their definitions are listed below.[11,14]

On/Off ratio and Photosensitivity

On/Off ratio and photosensitivity of photodetectors are defined as the ratio of the photocurrent and dark current or the resistance in the dark and under the illumination. They are expressed as

$$\text{On/Off ratio} = \frac{I_{photo}}{I_{dark}} = \mathrm{R}_{dark}/\mathrm{R}_{photo}$$

$$\text{Photosensitivity} = \frac{\Delta I}{I_{dark}} \times 100\ (\%) = \frac{\Delta \mathrm{R}}{\mathrm{R}_{photo}} \times 100\ (\%)$$

where I_{photo} is the photocurrent, I_{dark} is the dark current, ΔI is I_{photo} - I_{dark}, R_{dark} is the resistance in the dark, R_{photo} is the resistance under the illumination, and ΔR is R_{dark} - R_{photo}.

Responsivity

Responsivity (R_λ) is the ratio of photocurrent to incident light intensity. It indicates how efficiently the device convert optical signals into electrical signals. R_λ can be expressed as

$$R_\lambda = \frac{I_{\text{photo}}}{AL_{light}} \text{ (A/W)}$$

where A is the effective area of the device, L_{light} is the incident light intensity. As R_λ is proportional to the quantum yield of the photodetector, it is important that the photodetector has a high responsivity value.

External Quantum Efficiency

Quantum efficiency for photodetector is the photon-electron conversion efficiency. To rule out the effective change of the incident photon flux on the photocurrent, external quantum efficiency (EQE) is one of useful figure of merit parameters to estimate the wavelength-dependent photoresponse of photodetector. EQE of photodetector can be expressed as

$$\text{EQE} = \frac{R_\lambda hc}{\lambda q} \times 100 \text{ (\%)}$$

where h is Planck's constant, c is the velocity of light, λ is wavelength of incident light, and q is the elementary charge.

Detectivity (D^*)

Although the responsivity of a photodetector gives a measure of the output signal of the detector for a given optical input signal, it does not give any information about the sensitivity of the device. The sensitivity of the OPDs can be defined as the minimum detectable optical input power meaning a signal-to-noise ratio of unity.

Noise equivalent power (NEP) is defined as the minimum impinging optical power that a detector can distinguish from noise.

$$D^* = \frac{(A\Delta f)^{1/2}}{(R/i_n)} \text{ (cm Hz}^{1/2}\text{ W}^{-1}\text{ or Jones)}$$

where Δf is the electrical bandwidth and i_n is the noise current. When the shot noise is the main component of photodetector noise, the expression of D^* can be simplified as

$$D^* \approx \frac{J_{photo}/L_{light}}{(2qJ_{dark})^{1/2}} = \frac{R_\lambda A^{1/2}}{(2qI_{dark})^{1/2}} \text{ (cm Hz}^{1/2}\text{ W}^{-1}\text{ or Jones)}$$

where J_{photo} is the photocurrent density, J_{dark} is the dark current density f is the electrical bandwidth and i_n is the noise current. When the dark current is dominated by the shot noise, D* can be expressed as

Rise time (t_r) and decay time (t_d)

Rise time (t_r) is defined as the time for the current to rise from 10 % to 90 % of the peak value during illumination, whereas decay time (t_d) is also defined as the time for the current to decay from 90 % to 10 % of the peak value after turning off the light (Figure 2.7). For the application of photodetectors, a fast rise and decay speed are normally desired characters.

Linear dynamic range

Linear dynamic range (LDR) provides a linear relationship between I_{photo} and

L_{light}.in certain range. The wide LDR is desired characteristics for photodetector, especially high contrast applications, because it means the device can detect and calculate the light signal accurately. LDR can be expressed as

$$\text{LDR} = 20\log\frac{J_{upper}}{J_{lower}} = 20\log\frac{J^*_{photo}}{J_{dark}} \text{ (dB)}$$

where J is current density, J^*_{photo} is the photocurrent density measured at 1 mW cm^{-2}, and J_{dark} is dark current density. The upper and lower limit of the LDR can be determined by the current value that deviates from linearity (Figure 2.8).

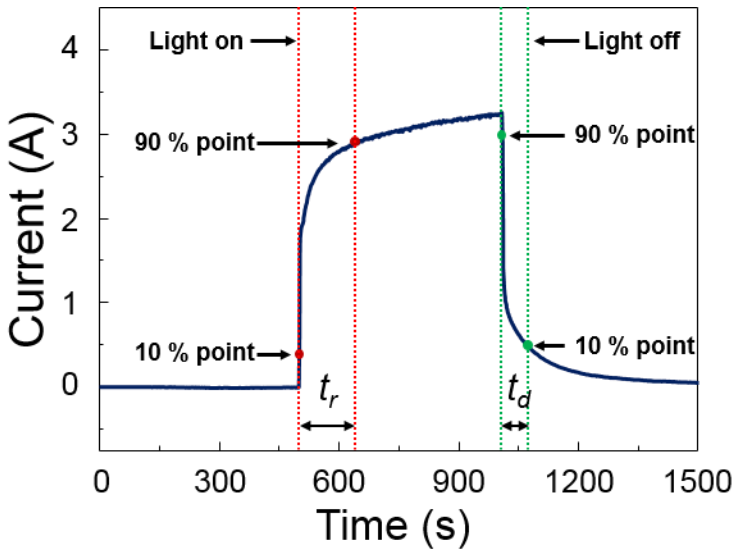

Figure 2.7. Definition of response time and recovery time

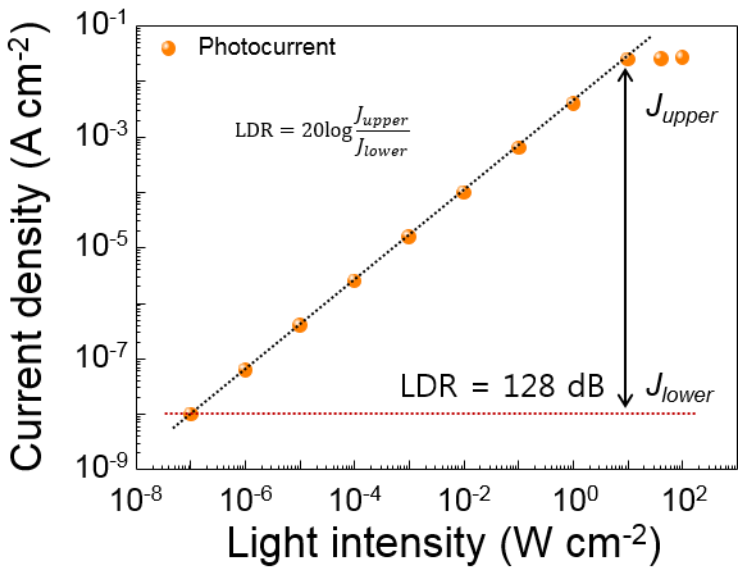

Figure 2.8. Definition of linear dynamic range (LDR)

2.2. Current issues in photodetectors

2.2.1. Limits of conventional photodetectors and previous studies

The commercial photodetectors normally use GaN, Si, and InGaAs as active materials to detect UV (250-400 nm), visible light (450-800 nm), NIR (900-1700 nm), respectively. The detectivities of typical Si-based photodetectors are about 2×10^{12} Jones (or $cmHz^{1/2}$ W^{-1}). However, for high sensitivity, the commercial photodetectors should be operated in low temperature (less than 100 K) and cooled down to reduce the dark current.[15] Moreover, conventional photodetectors show performance degradation when they are under the illumination of ultraviolet with energies much higher than the semiconductor bandgap energy. For next generation optoelectronics, it is desired to have room-temperature photodetecting systems with higher performance in terms of speed, efficiency, wider detection range, or low power consumption as well as low cost, simple fabrication, and complementary metal–oxide–semiconductor (CMOS) integrability and low cost.

In order to overcome the limits of conventional photodetecting systems, significant efforts have been made in searching for new materials for photodetection and enhancing photodetection performance of materials by controlling their nanostructure and chemical composition. Most of previous studies have focused on developing and enhancing the photoresponse performance of special wavelength (narrowband) photodetectors.[16-20] The special wavelength photodetectors show photoresponse under certain single wavelength or the incident light of a narrow range

and they are used for specific applications in light detecting and optoelectronic integrated circuits. The representative materials and techniques for special wavelength photodetectors were summarized here: UV photodetector based metal oxide semiconductors like ZnO, Ga_2O_3, and TiO_2;[18,-22] metal chalcogenides based photodetector (PbS, CdS, CdSe, and CdTe);[23-25] organic photodetectors;[26-28] detectors that use nanostructure, such as colloid quantum dots, nanoparticles, nanorods, nanowires, and nanoplatelets, to improve photoresponse performance due to superior charge transport and reduced charge recombination;[29-31] the superconducting nanowire single photon detector,[32] etc. despite Nevertheless, the special wavelength photodetectors still have problems Despite of rapid progress in special wavelength photodetectors, performance dependence on the environment (vacuum, temperature, and oxygen adsorption/desorption) makes it difficult to obtain high performance devices.[23]

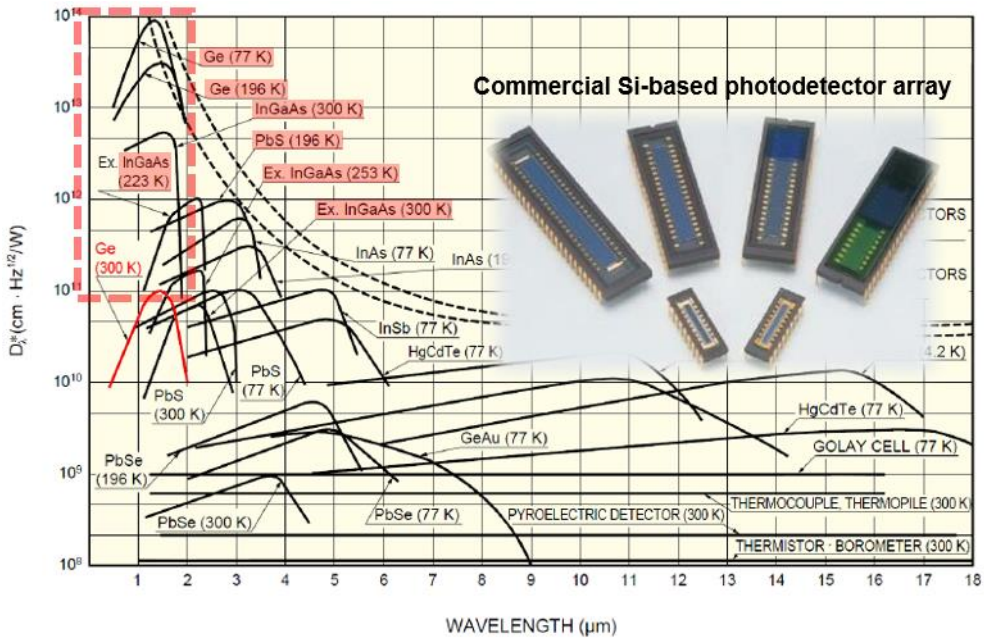

Figure 2.9. Detectivity curves for various commercial photodetector. Figure from Ref. [15].

2.2.2. Broadband photodetectors

Recently, broadband photodetection becomes a key issue due to demands on video imaging, biomedical imaging, day-and night-time surveillance, UV-visible-NIR communication, wide spectral switches, and memory storage using single photodetector.[6,11,33,34] For example, Light-Fidelity (Li-Fi), which is one of the state-of-the art technologies for wireless communication between devices, requires broadband photodetection systems as Li-Fi uses UV-visible-NIR to transmit data. As Li-Fi uses UV-visible-NIR to transmit data, it has many advantages such as harmless characteristics of visible light, free frequency-usage fee, high transmission rate, and high transmission capacity. Therefore, the broadband photodetector is expected to be a promising candidate and necessary component for public ubiquitous data communication technology in the near future and the broadband photodetector market is expected to grow rapidly. Nowadays, research and development in photodetectors have been mainly focused on realizing miniaturized design with high sensitivity, wide spectra response, fast speed, and excellent stability. In this section, several research issues for developing higher performance broadband photodetectors are discussed.

Issues in broadening the detectable wavelengths

As mentioned in section 2.2.1., previous studies were mostly related with special wavelength photodetectors because there is few appropriate candidates which can absorb incident light over broad wavelength range with excellent photoresponse performance. For example, in the case of metal oxide semiconductors which have

been mainly studied for narrowband photodetectors, there are very few materials with a bandgap energy 1.24 eV or less that can absorb up to 1000 nm of incident light and the materials shows poor optoelectronic transfer efficiency due to high recombination rate and short carrier diffusion length. Therefore, various materials such as organic materials, colloidal quantum dots, and two-dimensional (2D) materials have been employed.[35-39] However, none of them realizes broadband detection range, high sensitivity, and ultrafast speed.

In order to obtain high performance broadband photodetection, the active materials in photodetectors have to interact with a wide range of wavelengths to show a high on/off ratio. Therefore, broadening the range of wavelength that active materials can interact with is a key issue. To extend the detectable wavelength, one possible way is combining with functional materials which can influence the active materials and interact smaller photon energy than bandgap energy of active materials.[40] For example, 2D materials exhibit broadband photoreseponse when it combined with quantum dots to form a hybrid system for photodetction.[38] Plasmonic nanoparticles can be another functional materials which enhance the light-matter interaction and extend the detectable wavelength of photosensitive materials.[41-43] Due to the strong coupling with plasmonic nanoparticles and light, photosensitive materials can detect the wider wavelength of incident light and optical properties of photosensitive materials can be modulated. Coupling with microcavities can also broaden the range of wavelength at which light-matter interaction can occur. As the optical field inside a resonant cavity increases, active materials coupled with cavities can absorb a wider range of wavelength. For example, graphene sheet integrated with a high finesse planar optical cavity shows higher photoresponse due to enhanced light-matter

interaction.[44,45] Moreover, the effect of coupling of functional materials and microcavities can be maximized in the nanostructured active materials due to large surface-to-volume ratio and porous structure.

Issues in enhancing optoelectronic transfer efficiency

Generally, the photosensitive materials with a narrow band gap that can absorb a wide wavelength range show poor optoelectronic transfer efficiency due to short charge diffusion length and high recombination rate of photogenerated carriers. The optoelectronic transfer efficiency can be improved by using photosensitive materials synthesized in the form nanostructure. Due to the quantum size effects, large surface-to-volume ratio, and anisotropic geometry, longer charge diffusion length and superior charge transport can be observed in nanostructured materials.[46-48] Therefore, nanostructured materials show excellent photoresponse performance.

The optoelectronic transfer efficiency can be also improved by making a heterojunction with functional layers. Due to the built-in potential generated in heterojunction, especially p-n junction or type-Ⅱ junction, the photogenerated electron-hole pairs are well separated and the devices show higher performance. Fast response and recovery can be realized by junction controlled photocarriers separation process.

Issues in reliable performance

Reliable performance of device is as important as the high performance and high

sensitivity of the device. The photodetectors studied so far showed performance dependence on the environment. As mentioned above, commercial Si-based photodetectors should be worked in low temperature for high detectivitiy. The nanowire-based photodetectors, which have been intensively studied, show high detectivity at room temperature, but they exhibit poor performance in oxygen deficient environment because their operating mechanism is related with oxygen absorption/desorption.[23] For reliable operation of photodetectors, little dependence on the operating environment is required.

Defects in photosensitive materials are also factors affecting device reliability.[49] It is well known that defects in photosensitive materials act as recombination or trap site for photogenerated carriers. Furthermore, defects can be migrated by external bias and generate built-in potential which can screen the external bias and interrupt the separation of photogenerated electron-hole pairs. For reliable operation of broadband photodetectors, little dependence on the operating environment is required and defects in photosensitive materials should be well controlled.

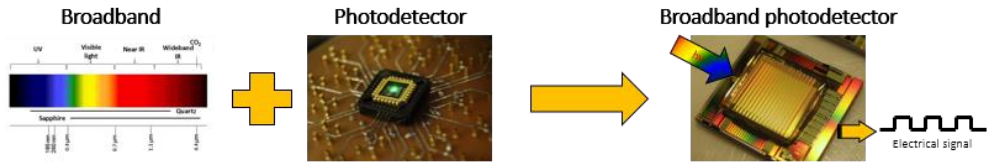

Figure 2.10. Broadband photodetector can detect spectral ranges from UV to NIR convert optical signals into electrical signals.

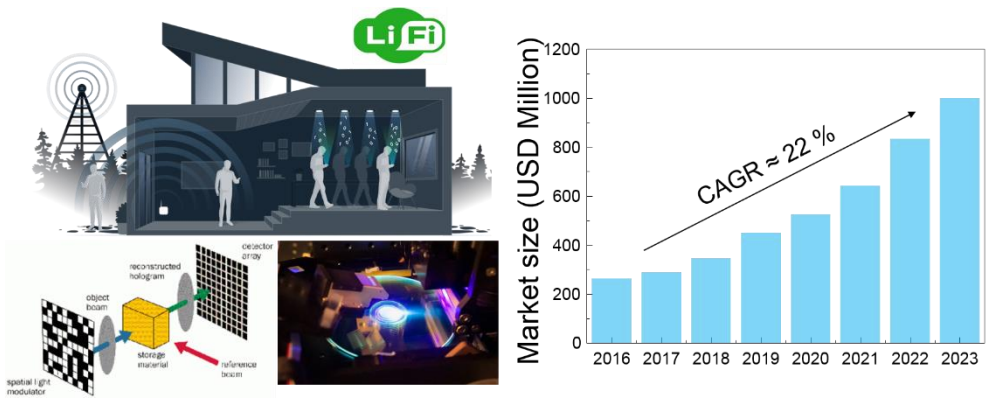

Figure 2.11. Application of Broadband photodetectors and broadband photodetector market size.

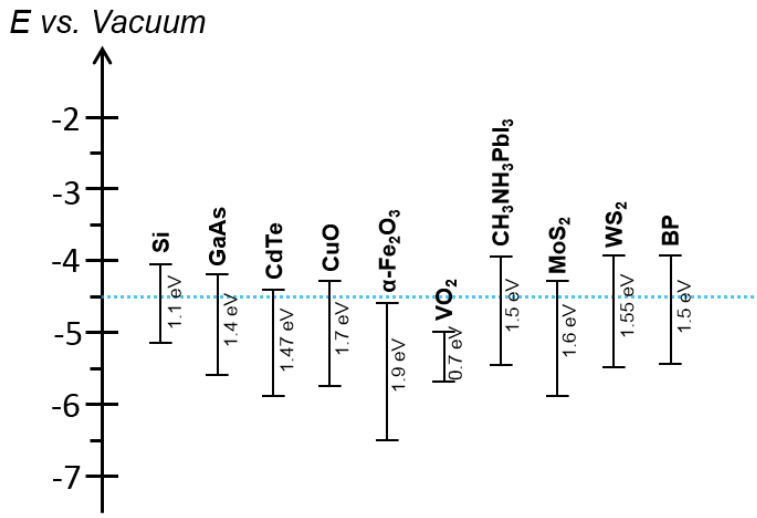

Figure 2.12. Band gap of various semiconductors materials. There are few materials that can absorb NIR with high optoelectronic transfer efficiency.

2.3. Reference

[1] J.-J. Wang, F.-F. Cao, L. Jiang, Y.-G. Guo, W.-P. Hu, L.-J. Wan, *J. Am. Chem. Soc.* **2009**, *131*, 15602.

[2] H. Kind, H. Yan, B. Messer, M. Law, P. Yang, *Adv. Mater.* **2002**, *14*, 158.

[3] J. S. Jie, W. J. Zhang, Y. Jiang, X. M. Meng, Y. Q. Li, S. T. Lee, *Nano Lett.* **2006**, *6*, 1887.

[4] T. Yang, K. Sun, X. Liu, W. Wei, T. Yu, X. Gong, D. Wang, Y. Cao, The *J. Phys. Chem. C* **2012**, *116*, 13650.

[5] G. Chen, B. Liang, X. Liu, Z. Liu, G. Yu, X. Xie, T. Luo, D. Chen, M. Zhu, G. Shen, Z. Fan, *ACS Nano*, **2014**, *8*, 787.

[6] Q. Hong, Y. Cao, J. Xu, H. Lu, J. He, J.-L. Sun, *ACS Appl. Mater. & Interfaces* **2014**, *6*, 20887.

[7] J.-M. Jeon, Y.-S. Shim, S. D. Han, D. H. Kim, Y. H. Kim, C.-Y. Kang, J.-S. Kim, M. Kim, H. W. Jang, *J. Mater. Chem. A* **2015**, *3*, 17939.

[8] J. M. Rondinelli, E. Kioupakis, *Ann. Rev. Mater. Res.* **2015**, *45*, 491.

[9] F. P. García de Arquer, A. Armin, P. Meredith, E. H. Sargent, *Nat. Rev. Mater.* **2017**, *2*, 16100.

[10] A. Rogalski, *Prog. Quant. Electron.* **2003**, *27*, 59.

[11] J. Zhou, J. Huang, *Adv. Sci.* **2018**, *5*, 1700256.

[12] G. Konstantatos, E. H. Sargent, *Nat. Nanotechnol.* **2010**, *5*, 885.

[13] W. Choi, M. Y. Cho, A. Konar, J. H. Lee, G.-B. Cha, S. C. Hong, S. Kim, J. Kim, D. Jena, J. Joo, S. Kim, *Adv. Mater.* **2012**, *24*, 5832.

[14] L. Dou, Y. Yang, J. You, Z. Hong, W.-H. Chang, G. Li, Y. Yang, *Nat. Commun.* **2014**, *5*, 5404.

[15] W. Zeller, H. Efstathiadis, G. Bhowmik, P. Haldar, N. K. Dhar, J. Lewis, P. Wijewarnasuriya, Y. R. Puri, A. K. Sood, *Int. J. Eng. Res. & Technol*. **2015**, *8*, 23

[16] J. H. Jun, H. Seong, K. Cho, B.-M. Moon, S. Kim, *Ceram. Int.* **2009**, *35*, 2797.

[17] Z. Liu, F. Li, S. Li, C. Hu, W. Wang, F. Wang, F. Lin, H. Wang, *Sci. Rep.* **2015**, *5*, 14420.

[18] C. Tian, D. Jiang, B. Li, J. Lin, Y. Zhao, W. Yuan, J. Zhao, Q. Liang, S. Gao, J. Hou, J. Qin, *ACS Appl. Mater. & Interfaces* **2014**, *6*, 2162.

[19] H. Chen, K. Liu, L. Hu, A. A. Al-Ghamdi, X. Fang, *Mater. Today* **2015**, 18, 493.

[20] L. Sang, M. Liao, M. Sumiya, *Sensors* **2013**, *13*, 10482.

[21] U. M. Nayef, K. A. Hubeatir, Z. J. Abdulkareem, *Optik* **2016**, *127*, 2806.

[22] L. X. Qian, X. Z. Liu, T. Sheng, W. L. Zhang, Y. R. Li, P. T. Lai, *AIP Advances* **2016**, *6*, 045009.

[23] K. Deng, L. Li, *Adv. Mater.* **2014**, *26*, 2619.

[24] Y. Pei, R. Pei, X. Liang, Y. Wang, L. Liu, H. Chen, J. Liang, *Sci. Rep.* **2016**, *6*, 21551.

[25] A. De Iacovo, C. Venettacci, L. Colace, L. Scopa, S. Foglia, *Sci. Rep.* **2016**, *6*, 37913.

[26] M. Kielar, O. Dhez, G. Pecastaings, A. Curutchet, L. Hirsch, *Sci. Rep.* **2016**, *6*, 39201.

[27] K.-J. Baeg, M. Binda, D. Natali, M. Caironi, Y.-Y. Noh, *Adv. Mater.* **2013**, *25*, 4267.

[28] J. Miao, F. Zhang, Y. Lin, W. Wang, M. Gao, L. Li, J. Zhang, X. Zhan, *Adv. Opt. Mater.* **2016**, *4*, 1711.

[29] P. Martyniuk, A. Rogalski, *Prog. Quant. Electron.* **2008**, *32*, 89.

[30] F. H. Wang, C. E. Tsai, *IEEE* J. Sel. Top, Quant. Electron. **2017**, *23*, 58.

[31] D.-D. Wang, C.-W. Ge, G.-A. Wu, Z.-P. Li, J.-Z. Wang, T.-F. Zhang, Y.-Q. Yu, L.-B. Luo, *J. Mater. Chem. C* **2017**, *5*, 1328.

[32] G. N. Gol'tsman, O. Okunev, G. Chulkova, A. Lipatov, A. Semenov, K. Smirnov, B. Voronov, A. Dzardanov, C. Williams, R. Sobolewski, *Appl. Phys. Lett.* **2001**, *79*, 705.

[33] X. Hu, X. Zhang, L. Liang, J. Bao, S. Li, W. Yang, Y. Xie, *Adv. Funct. Mater.* **2014**, *24*, 7373

[34] H. Wang, D. H. Kim, *Chem. Soc. Rev.* **2017**, *46*, 5204

[35] X. Gong, M. Tong, Y. Xia, W. Cai, J. S. Moon, Y. Cao, G. Yu, C.-L. Shieh, B. Nilsson, A. J. Heeger, *Science*, **2009**, *325*, 1665.

[36] S. A. Mcdonald, G. Konstantatos, S. G. Zhang, P. W. Cyr, E. J. D. Klem, L.

Levina, E. H. Sargent, *Nat. Mater.* 2005, *4*, 138.

[37] G. Konstantatos, I. Howard, A. Fischer, S. Hoogland, J. Clifford, E. Klem, L. Levina, E. H. Sargent, *Nature*, **2006**, *442*, 180.

[38] Y. Liu, R. Cheng, L. Liao, H. Zhou, J. Bai, G. Liu, L. Liu, Y. Huang, X. Duan, *Nat. Commun.* **2011**, *2*, 579.

[39] Y. Zhang, T. Liu, B. Meng, X. Li, G. Liang, X. Hu, Q. J. Wang, *Nat. Commun.* **2013**, *4*, 1811.

[40] J.-C. Lin, V. T. Tra, D.-S. Tsai, T.-T. Lin, P.-C. Huang, W.-L. Hsu, H. J. Wu, R. Huang, N. V. Chien, R. Yoshida, J.-Y. Lin, Y. Ikuhara, Y.-P. Chiu, S. Gwo, D. P. Tsai, J.-H. He, Y.-H. Chu, *Adv*. *Mater*. **2016**, 28, 764.

[41] G. Xu, C.-M. Huang, P. Jin, M. Tazawa, D.-M Chen, *J. Appl. Phys*. **2008**, *104*, 053101.

[42] G. Xu, C.-M. Huang, P. Jin, M. Tazawa, D.-M Chen, *J. Appl. Phys*. **2008**, *104*, 053102.

[43] C. Clavero, *Nat. Photon.* **2014**, *8*, 95.

[44] M. Engel, M. Steiner, A. Lombardo, A. C. Ferrari, H. V. Lohneysen, P. Avouris, R. Krupke, *Nat. Commun,* **2012**, *3*, 906

[45] M. Furchi, A. Urich, A. Poslischil, G. Lilley, K. Unterrainer, H. Detz, P. Klang, A. M. Andrews, W. Schrenk, G. Strasser, T. Mueller, *Nano Lett.* **2012**, *12*, 2773.

[46] S. Jizhong, X. Leimeng, L. Jianhai, X. Jie, D. Yuhui, L. Xiaoming, Z. Haibo,

Adv. Mater. **2016**, *28*, 4861.

[47] H. Zhou, J. Zeng, Z. Song, C. R. Grice, C. Chen, Z. Song, D. Zhao, H. Wang, Y. Yan, *J. Phys. Chem. Lett.* **2018**, *9*, 2043.

[48] W. Deng, L. Huang, X. Xu, X. Zhang, X. Jin, S.-T. Lee, J. Jie, *Nano Lett*. **2017**, *17*, 2482.

[49] K. C. Kwon, K. Hong, Q. V. Le, S. Y. Lee, J. Choi, K.-B. Kim, S. Y. Kim, H. W. Jang. *Adv. Funct, Mater*. **2016**, *26*, 4213.

Daylight-Induced Metal-Insulator Transition in Surface Functionalized VO_2 and Application to Broadband Photodetectors

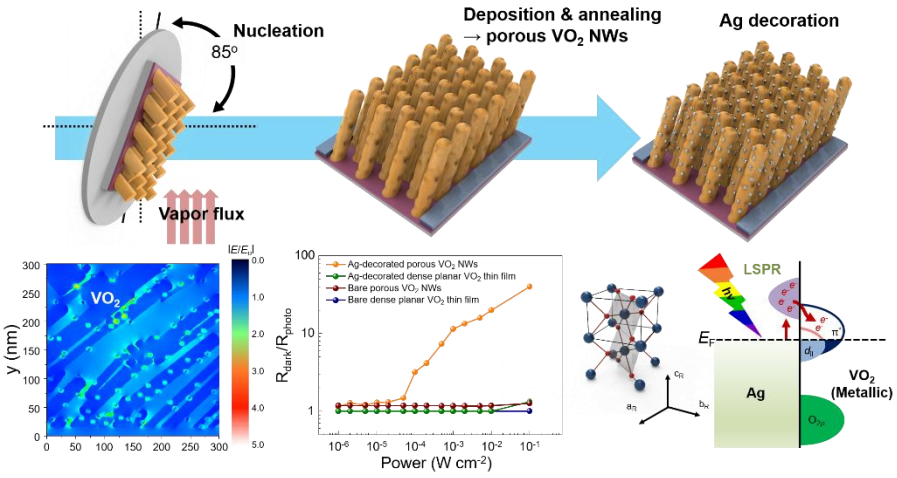

3.1. Introduction

Correlated materials exhibit remarkable physical properties, such as superconductivity,[1,2] colossal magnetoresistance,[3] and metal-insulator transition (MIT),[4-8] all of which are profoundly affected by electron-electron interaction (Figure 3.1). Understanding these remarkable physical phenomena is essential for condensed matter physics and it can provide clues to overcome the limits of conventional electronic devices. Vanadium dioxide (VO_2), one of the most fascinating strongly correlated materials, shows first-order reversible MIT near room temperature (critical temperature T_c = 68 ºC for bulk single crystal) in a few picoseconds (Figure 3.2).[9-13] Across the MIT, insulating monoclinic VO_2 below the T_c changes into metallic rutile VO_2 above the T_c, accompanied by abrupt changes of electrical conductivity,[4-11] and optical transmittance,[12,13] especially in the infrared region. The MIT in VO_2 can be triggered by various external ambient parameters, such as temperature,[14] electric field,[15,16] strain,[17,18] and gas adsorption/desorption through electron-electron interaction (Figure 3.3).[19,20] Therefore, various efforts have been made to incorporate VO_2 into diverse electronics and multifunctional devices such as transistors,[9] memories,[14,16] strain sensors,[18] gas sensors,[19,20] and smart windows (Figure 3.4).[21]

As VO_2 can absorb a wide range of wavelengths from visible to infrared light due to its narrow band gap (0.7 eV),[12,13] VO_2 is fascinating materials for optoelectronics, especially photodetectors and smart window. Photo-induced in VO_2 may provide unique routes to overcome limits of conventional optoelectronics by showing the required characteristics for future optoelectronics such as fast response and recovery

time, broadband photoresponse, and lower power consumption. However, there have been few reports on photo-induced MIT using single wavelength high power pump laser[10,11] or indirect methods such as the joule heating effect of infrared irradiation,[22] or oxygen adsorption/desorption under UV laser irradiation.[23,24] It is difficult to provoke MIT in VO_2 by daylight exposure because the number of required photogenerated carriers for MIT in VO_2 is negligible due to their high recombination rate.[25,26]

One possible way to overcome these hurdles is to integrate VO_2 with functional layers or nanoparticles (NPs) that assist VO_2 to respond to the incidence of light. Localized surface plasmon resonance (LSPR), which is resonant oscillation of conduction electrons stimulated by the incidence of light (Figure 3.5),[27,28] can modulate electron-electron interaction in VO_2 by light itself regardless of operating conditions. Moreover, incorporation of plasmonic NPs with semiconductors can change the optical properties of them through coupling with light.[29,30] By depositing one of the plasmonic NPs, silver nanoparticles (Ag NPs) on the VO_2 surface, electric field enhancement near from the interface between Ag NPs and VO_2 can trigger photo-induced MIT in VO_2 and a wide range of light wavelengths can provoke photo-induced MIT because LSPR at the interface between Ag NPs and VO_2 can be excited by broadband light ranging from ultraviolet to near infrared.

In this chapter, we report the daylight-induced MIT in Ag-decorated porous VO_2 nanorod arrays (NRs) and their application to broandband photodeteoctors. To our best knowledge, this is the first report on broadband photoresponse of VO_2 by visble light induced MIT. The porous nanostructures and the extremely large surface-to-volume ratio of porous VO_2 NRs result in a larger specific area for the illumination,

a larger number of decorated Ag NPs and a well distribution of Ag NPs throughout the porous VO_2 NRs when compared to those of dense planar VO_2 thin films. With Ag NPs decoration, the electric fields are generated at the interface between Ag NPs and VO_2 under the illumination due to LSPR and provoke photo-induced MIT under the illumination of AM 1.5G 0.1 sun condition. The MIT in Ag-decorated porous VO_2 NRs occurred under a wide range of wavelengths and, therefore, broadband photodetection of Ag-decorated porous VO_2 NRs were available from 400 nm to 1000 nm.

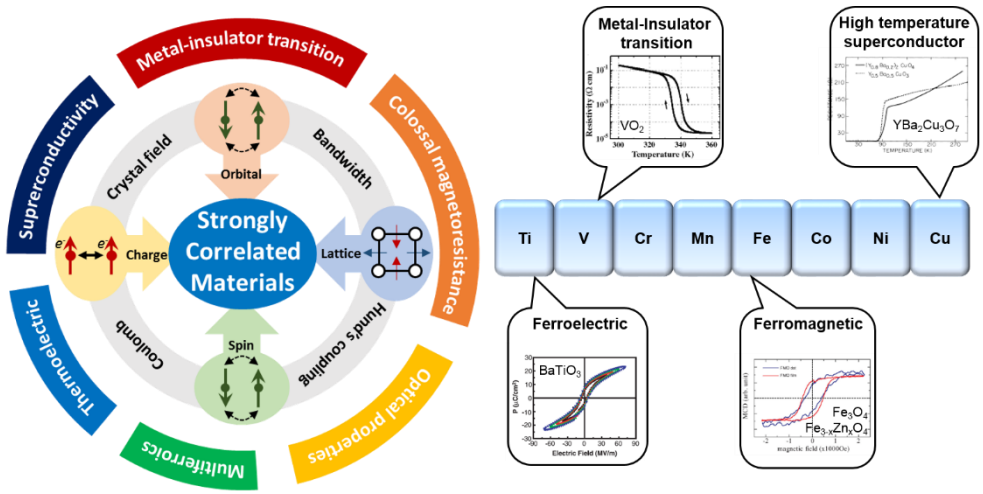

Figure 3.1. Schematic diagram showing electronic and structural degrees of freedom and novel physical phenomena. Transition metal oxides show metal-insulator transition, superconductivity, and ferroelectricity due to incompletely filled *d*- or *f*-orbitals. Figures from Ref. [31-34].

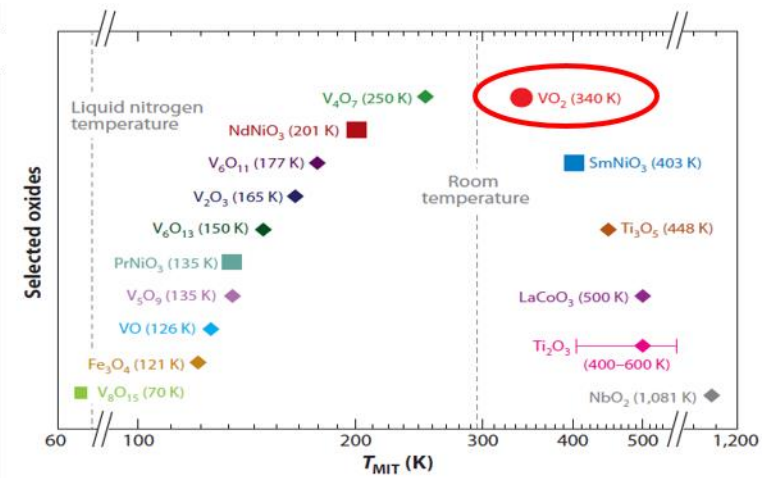

Figure 3.2. Materials exhibiting MIT and their critical temperature for MIT. Figure from Ref. [35].

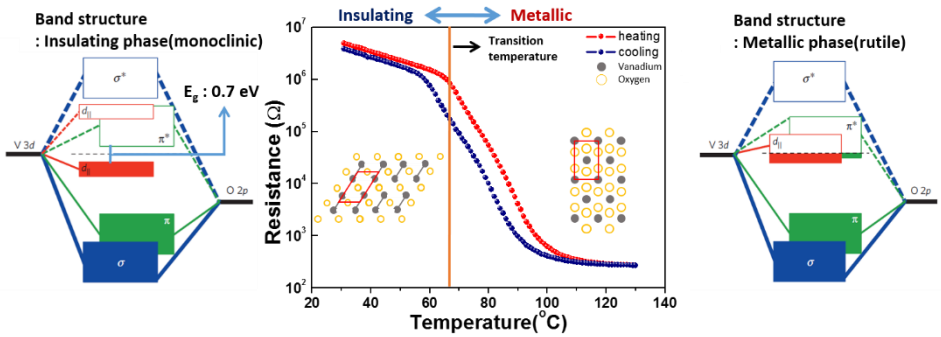

Figure 3.3. Band structure and electrical resistance of vanadium dioxide (VO_2) before and after MIT. Figure from Ref. [36].

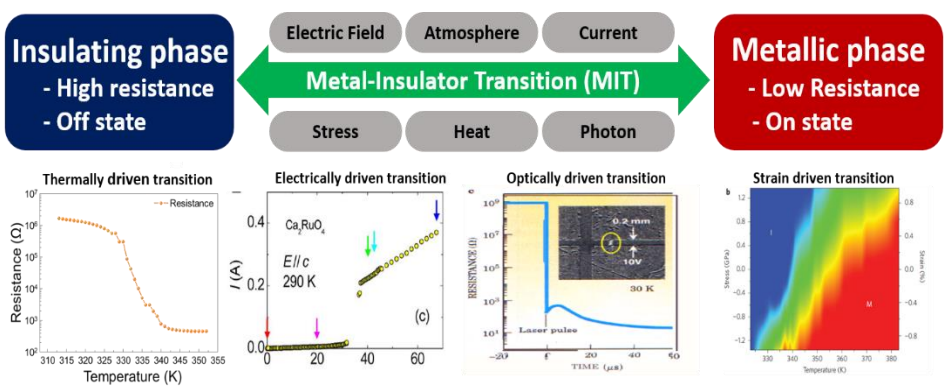

Figure 3.4. Metal-insulator transition (MIT) driven by various external stimuli. Figures from Ref. [37-39].

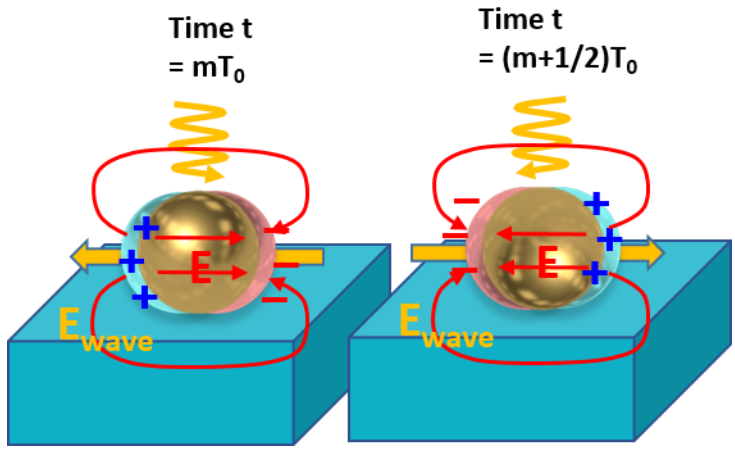

Figure 3.5. Schematic illustration for localized surface plasmon resonance.

3.2. Experimental procedures

3.2.1. Film preparation and device fabrication

As shown in Figure 3.6, Ag-decorated porous VO_2 NRs were prepared by e-beam evaporation with glancing angled deposition method. 2-5 nm V_2O_5 grains and Ag pellets of 99.99% purity (Kojundo Chemistry) were utilized for the deposition. Before deposition, SiO_2/Si substrates (1 μm/550 μm) were cleaned in acetone, ethanol, and isopropanol via sonication followed by drying in a nitrogen atmosphere. The 85° tilted substrate was located 50 cm from the crucible. The base pressure, e-beam voltage, and deposition temperature were 10^{-6} Torr, 7.4 kV, and room temperature, respectively and the deposition rate was kept at about 1.0 Å s^{-1}. After deposition, as-deposited porous V_2O_5 NRs was annealed at 500 ºC under reducing conditions to obtain porous polycrystalline VO_2 NRs. Pt/Ti (70 nm/30 nm) films were deposited on the nanorods array as electrodes using a shadow mask. To decorate Ag NPs on the surface of porous VO_2 NRs, a 1 nm thick (mass thickness) Ag film, which subsequently aggregated into well-spaced Ag nanoparticles, was deposited on the whole area of the device at the original position (0˚) with an evaporation rate of 0.05 Å s^{-1}.

3.2.2. Film characterization

The morphological and structural characterization of the Ag-decorated porous VO_2 NRs were conducted with a field emission scanning electron microscope (FESEM, MERLIN-COMPACT) using an acceleration voltage of 15 kV. Cross-sectional

transmission electron microscope (TEM) specimens of Ag-decorated porous VO_2 NRs on SiO_2/Si substrate were prepared by conventional methods of mechanical polishing followed by ion milling with Ar ions.

3.2.3. Finite-difference time-domain (FDTD) simulation

The electric field distribution near the interface between Ag NPs and VO_2 thin films was calculated using a commercial software program, FDTD solution (Lumerical Solutions Inc., version 8.16.982). The simulation condition was composed of a perfectly matched layer (PML) boundary condition and symmetric boundary condition according to the simulation configuration. Total-field scattered-field was imported as a light source in the 200 to 2000 nm wavelength domain. Transmittance was calculated via frequency-domain field and power monitor. The meshing condition was set to the automatic non-uniform mode, and the refinement was set to conformal variant 1. The mesh size was selected 0.025 nm for the films and 0.5 nm for the nanostructures. The calculation region was 18 × 18 nm^2 for top view of Ag/VO_2 interface, 12 × 12 nm^2 for Ag/VO_2 cross-sectional view and 300 × 300 nm^2 Ag-decorated porous VO_2 N Rs and Ag-decorated dense planar VO_2 thin films, respectively.

3.2.4. Device characterization

Photoresponse properties of the bare dense planar VO_2 thin films, Ag-decorated dense planar VO_2 thin films, bare porous VO_2 NRs, and Ag-decorated porous VO_2

NRs were measured in our homemade 4-probe station. An Agilent 4156C semiconductor parameter analyzer was used to apply a scanning bias and to test the output current simultaneously (Figure 3.7). The steady-state photocurrent curves were measured under simulated AM 1.5G irradiation (5 mW cm^{-2}) using a Xenon lamp with various filters (Oriel 66902). The electrical tests were mainly performed in air wherein various intensities of white light (AM 1.5G, from 10 μW cm^{-2} ~ 10 mW cm^{-2}) were incident through a fiber in a chamber. To evaluate whether the environment affects device performance, the measurements were also performed in N_2, Ar, O_2, and under vacuum (10 mTorr). To evaluate the device performance parameters, the on/off ratio, photosensitivity, responsivity, and external quantum efficiency were calculated by the following equations: The on/off ratio is the ratio of the resistance of devices in the dark to the resistance of device under the illumination. It is expressed by $R_{dark}/R_{photo} = I_{photo}/I_{dark} = J_{photo}/J_{dark}$, where R_{dark} is the resistance of the device in the dark, R_{photo} is the resistance of device under illumination, I_{photo} is the photocurrent, I_{dark} is the dark current, J_{photo} is the photocurrent density, and J_{dark} is the dark current density. Responsivity (R_λ) defined as the ratio of the photocurrent to the incident light on the effective area. It is given by $R_\lambda = I_{ph}/AL$, where A is the effective area and L is the incident light intensity. External quantum efficiency (EQE) is expressed EQE = $(R_\lambda \times h \times c)/(\lambda \times e)$, where R_λ is responsivity, h is Planck's constant, c is the velocity of light, λ is the light wavelength, and e is the electron charge. Photosensitivity is defined as $100 \times (R_{dark}/R_{photo} - 1)$.

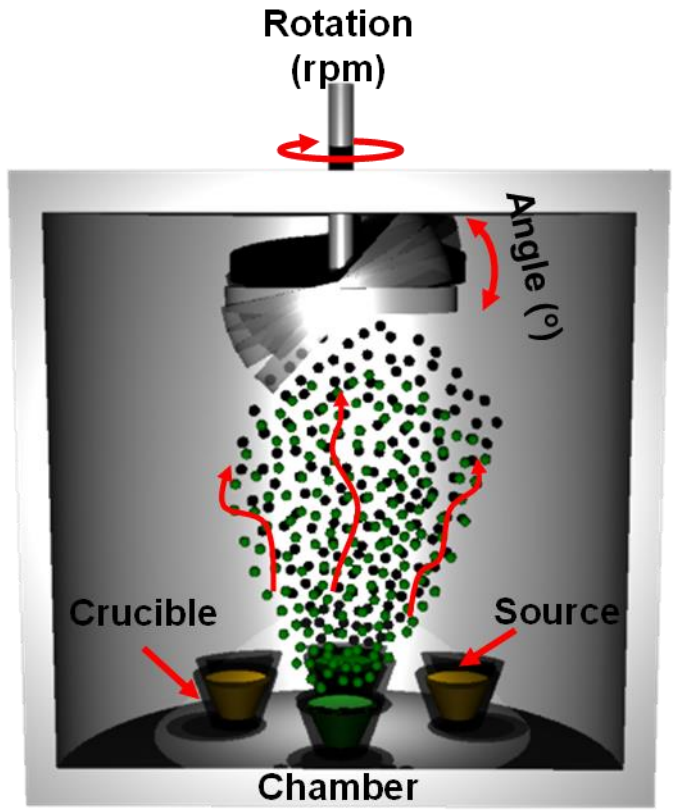

Figure 3.6. Glancing angle deposition method using electron beam evaporator.

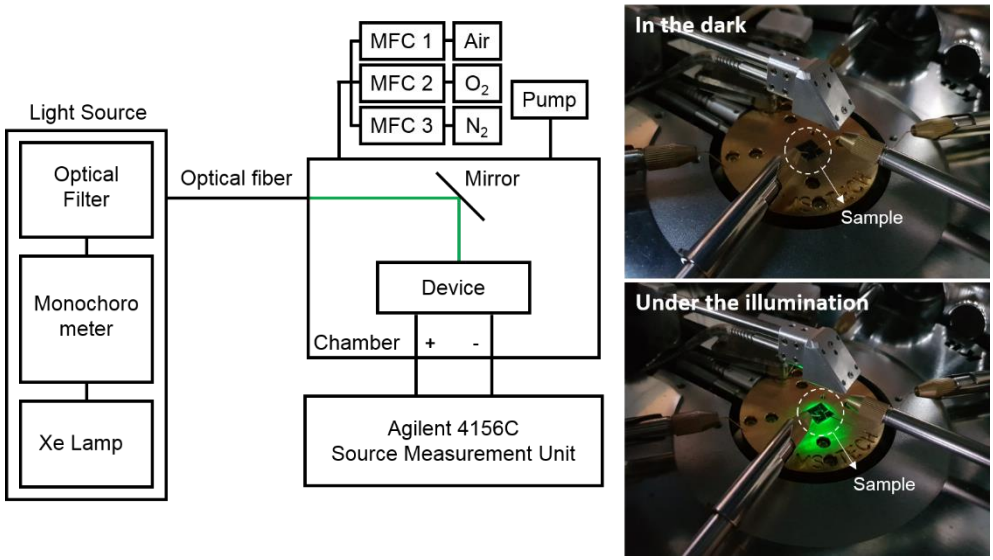

Figure 3.7. Measurement set-up for photoresponse of devices.

3.3. Results and Discussion

3.3.1. Morphology of Ag-decorated VO_2 nanorod arrays

The schematic diagram for the fabrication procedure of our photodetector based on Ag-decorated porous VO_2 NRs, is illustrated in Figure 3.8. To prepare porous VO_2 NRs, a glancing angle deposition technique was used, which has been adopted for decades to make porous thin films with a variety of 1D nanostructures such as zigzag nanocolumns, nanoblades, and nanorods.[40] By controlling deposition angle and rotation speed of substrate, morphology, porosity, and physical properties can be tailored to appropriate shapes for various applications including sensors,[40,41] and optical filters.[42] Sun *et al*. reported that the deposition angle should be higher than 80° to obtain a uniform and regular arrangement of VO_2 nanorods from a V_2O_5 source.[43] Therefore, to fabricate VO_2 NRs, a 250 nm thick layer of amorphous V_2O_5 NRs was deposited at 85° onto a predefined area using a shadow mask on a SiO_2/Si substrate using an electron beam (e-beam) evaporator. To obtain porous VO_2 NRs, the as-deposited thin films were annealed at reducing ambient. After annealing, top electrodes were deposited onto the porous VO_2 NRs residing on the SiO_2/Si substrates. Pt/Ti (70/30 nm) electrodes were fabricated using an e-beam evaporator through a shadow mask. Finally, a 1 nm thick (mass thickness) Ag film was deposited on the whole area of the device using an e-beam evaporator.

The scanning electron microscope (SEM) image in Figure 3.9a shows the cross-section of Ag-decorated porous VO_2 NRs on the substrate. The average diameter of the Ag-decorated porous VO_2 nanorods was about 50 nm , and the nanorods were separated from each other by vertically elongated pores, which extend to nearly over

the full thickness of the film. These pores cause the VO_2 NRs to exhibit a larger surface area for Ag NPs decoration than dense planar VO_2 thin films. Cross-sectional transmission electron microscopy (TEM) image of the Ag-decorated porous VO_2 NRs in Figure 3.9b confirms the distribution of Ag NPs over the whole surface of VO_2 nanorods, including the sidewalls. As shown in Figure 3.9c, high resolution TEM image of the Ag-decorated porous VO_2 NRs reveals that Ag NPs on the VO_2 nanorods are polycrystalline with (111) being the preferred orientation and no interfacial compounds were found near the interface between Ag NP and VO_2 NRs. The ring shape of the diffraction patterns of the selected area (Figure 3.9d) shows the polycrystalline nature of the VO_2 NRs after annealing.

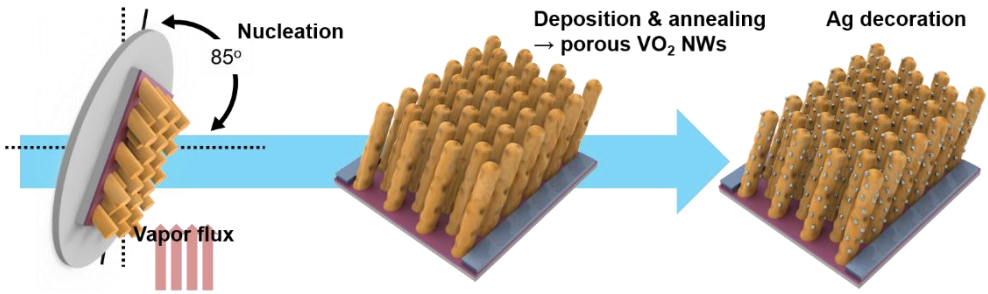

Figure 3.8. Schematic illustration for the fabrication process of Ag-decorated porous VO_2 nanorod arrays (NRs)

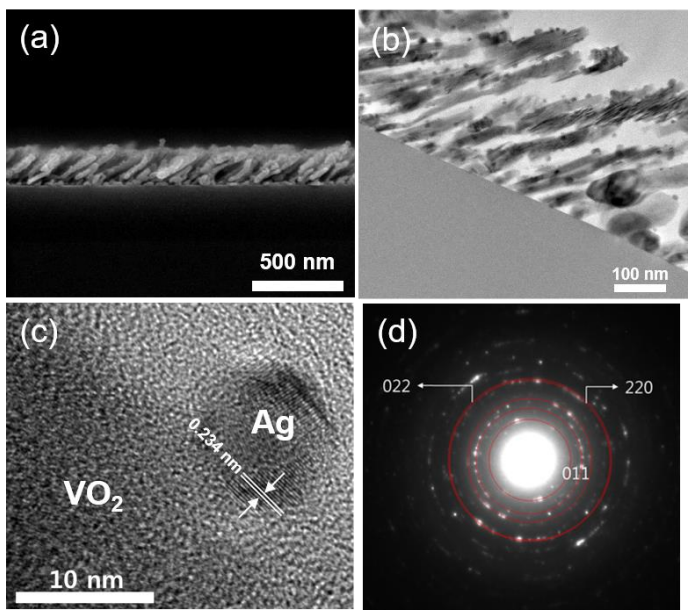

Figure 3.9. (a) Cross-sectional SEM and (b) TEM images of the Ag-decorated porous VO_2 NRs. (c) High magnification TEM image of an Ag nanoparticles on a VO_2 nanorod. (e) Selected area diffraction pattern of the VO_2 NRs.

3.3.2. Electrical properties of Ag-decorated VO_2 nanorod arrays

To investigate how the nanostructures and Ag NPs decoration affect the electrical properties of the devices, the normalized electrical resistance of the device with various external biases (V_{ex}) from 1 V to 10 V at room temperature in the dark was plotted as shown in Figure 3.10a. Bare porous VO_2 NRs of the same thickness, Ag-decorated and bare dense planar VO_2 thin films based photodetectors were also prepared in a similar procedure in order to compare them to our device. The four types of devices showed different levels of resistance at V_{ex} of 1 V, as a result of different porosity and the depletion region that was formed between Ag and VO_2 (Figure 3.10b). The devices based on dense planar VO_2 thin films with and without Ag decoration showed a negligible resistance change of less than 3 %, even at V_{ex} of 10 V. In contrast, the devices based on Ag-decorated and bare porous VO_2 NRs showed severe resistance drops of up to 70 % with increasing applied bias. The resistance change of the Ag-decorated porous VO_2 NRs was 20 times higher than that of bare dense planar VO_2 thin films. To investigate which conduction mechanism causes the severe resistance change of the porous VO_2 NRs, a double logarithmic plot of the current-voltage (*I-V*) characteristics in the dark and linear fitting were performed at low voltage and high voltage region (Figure 3.11a-b). In the dark *I-V* characteristics under low external bias ($V_{ex} < 0.5$ V) and high external bias ($V_{ex} > 0.5$ V), the slopes of the fitted lines in the double logarithmic plot were 1.01 and 1.51, respectively. These results indicate that the conduction behavior under low external bias follows Ohm's law ($I \propto V$), whereas the conduction behavior under

high external bias does not follow; in particular, the deviation of the plot from a slope of 1.0 indicates that conduction occurs by a mechanism other than Ohm's law. The high external bias region was replotted to further investigate the conduction mechanism (Figure 3.11c). The plot of $\log(I/V)$ versus $V^{1/2}$ is linear and matches well with the Poole-Frenkel emission mechanism.[44] The result indicates that the porous VO_2 NRs contain traps, especially at the narrow necks between VO_2 nanorods, where the charge carriers can be trapped in these trapping sites. With a high external bias, the charges have enough energy to overcome the energy barrier of the traps and severe resistance drop can occur in the porous VO_2 NRs. Although Joule heating effect can be one of the reasons for the severe resistance drop in the porous VO_2 NRs, thermographic images show that the increase in film temperature by Joule heating was negligible (Figure 3.12). The Ag-decorated porous VO_2 NRs showed larger resistance changes than the bare porous VO_2 NRs. The disparity demonstrates that Ag NPs decoration can enhance the resistance change of devices because Ag NPs make the energy barrier between VO_2 nanorods become higher due to the formation of depletion region between Ag and VO_2.

Since the resistance change of the tested devices is a result of an enhanced number of effective carriers, the critical temperature for MIT of devices can be changed. To this end, the resistance of the devices was measured with applied external bias at 1 V and 5 V with varying temperature, and the derivatives of the resulting resistance-temperature curve are shown in Figure 3.13a-b, respectively. At an applied external bias at 1 V, the resistance of the device changed by a factor of $\sim 10^2$ due to thermally induced MIT and hysteretic loops occur due to resistance changes in the VO_2 thin films during heating and cooling. From the derivatives of the resistance-temperature

curve, the T_c of the device was determined to be 68.8 °C at an applied bias of 1 V, which is similar with the reported T_c of bulk or unstrained VO_2 thin films (68 °C). However, with an applied bias of 5 V, the derivatives of the resistance-temperature curve indicates that MIT occurs at a T_c of 58.7 ºC though the devices showed a smaller resistance change by a factor of 47.01. The smaller resistance changes during MIT and the lower T_c are due to the dominance of Poole-Frenkel conduction in the insulating state of porous VO_2 NRs. This finding of the bias dependent T_c in the porous VO_2 NRs can open up a new pathway to lower the T_c of VO_2.

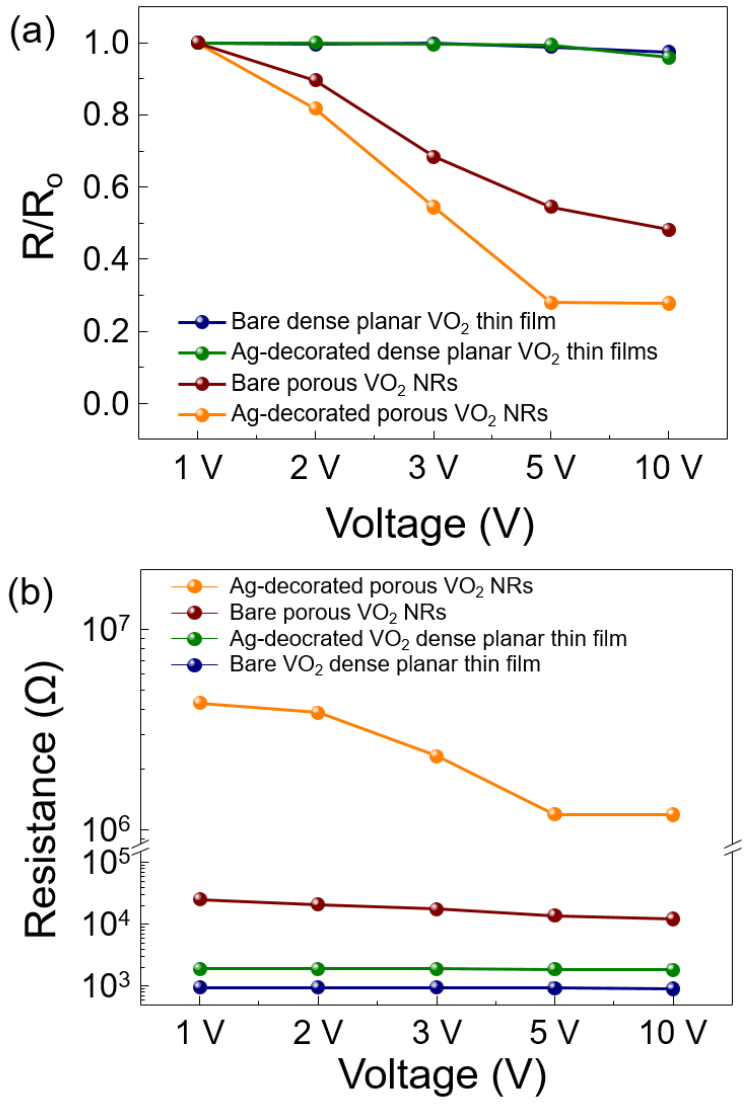

Figure 3.10. (a) Normalized electrical resistance of the devices as a function of bias (b) Electrical resistance of the devices as a function of bias.

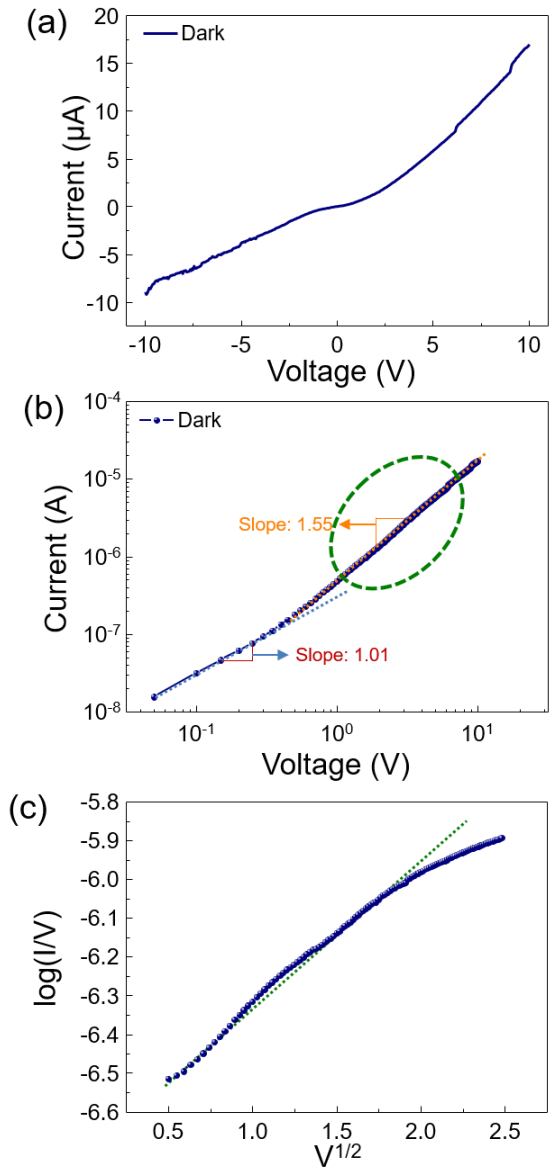

Figure 3.11. (a) Dark *I-V* characteristics of Ag-decorated porous VO_2 NRs and (b) double logarithmic and (c) log(*I*/*V*) versus $V^{1/2}$ plots of the dark *I-V* curve.

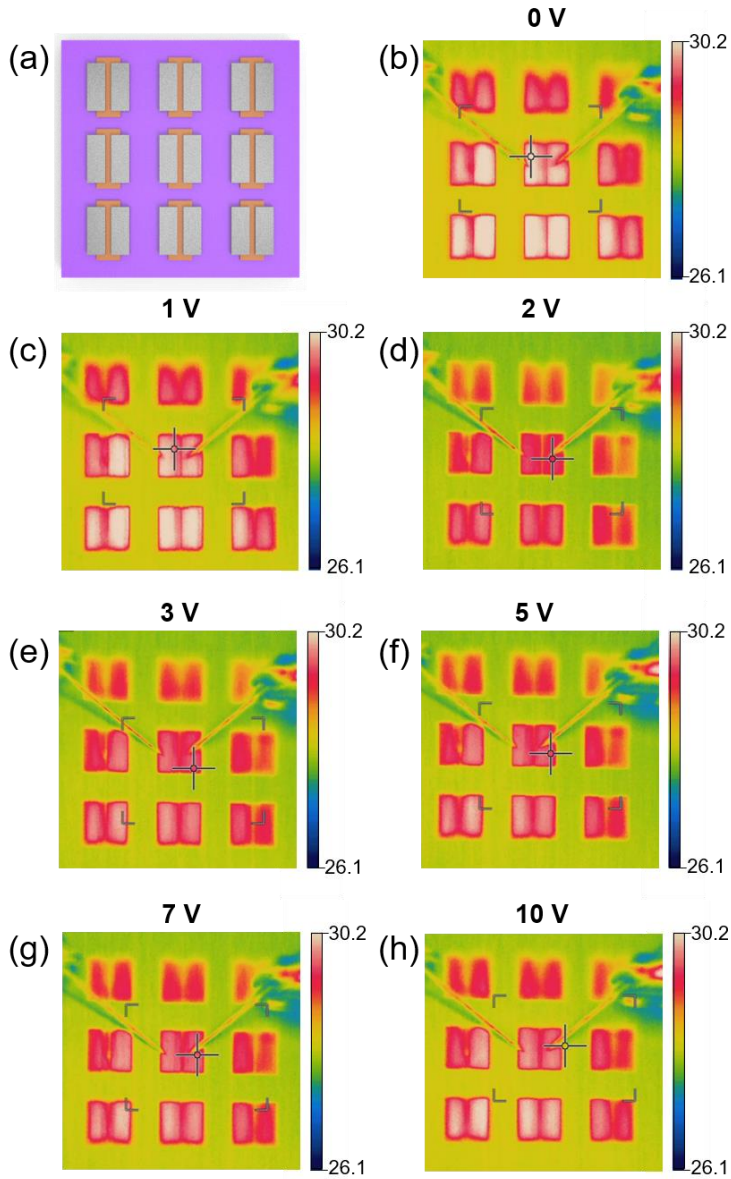

Figure 3.12. (a) Schematic diagram of devices. Thermographic images of the Ag-decorated porous VO_2 NRs at various applied external biases. (b) 0 V, (c) 1 V, (d) 2 V, (e) 3 V, (f) 5 V, (g) 7 V, and (h) 10 V

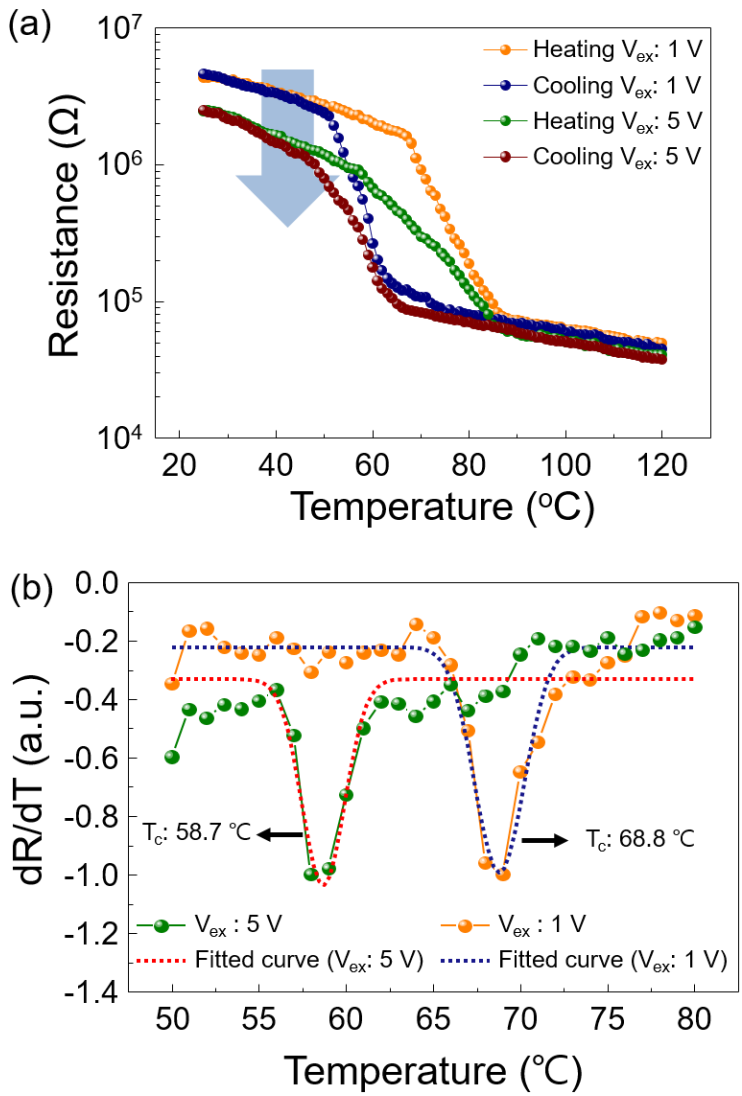

Figure 3.13. (a) Electrical resistance of the Ag-decorated porous VO_2 NRs as a function of temperature, measured with external biases of 1 V and 5 V. (b) Derivative of the resistance vs. temperature plot for applying external bias at 1 V and 5 V.

3.3.3. Finite-difference time domain simulations

FDTD simulations on Ag/VO_2 systems

The optical properties of dense planar VO_2 thin films with plasmonic metal nanoparticles, such as Ag and Au, have been reported based on the Maxwell-Garnett theory, which is widely applied for interpreting the optical properties of composite materials.[29,30] However, the Maxwell-Garnett theory is inadequate for interpretation of porous Ag-decorated VO_2 NRs as the theory does not consider effect of nanostructures in thin films. Therefore, to understand the LSPR effect and consider the nanostructure effects on thin films, we have employed finite-difference time-domain (FDTD) simulations to calculate the near field distribution between Ag NPs and porous VO_2 NRs. Before conducting FDTD simulations on between Ag NPs and porous VO_2 NRs, we performed FDTD simulations on the Ag NP/VO_2 systems at exposure to various wavelengths (405 nm ~ 1000 nm) of incident light to calculate the electric field distribution of the LSPR at the interface of Ag NPs and VO_2 layer. Figure 3.14a-f show the top view and cross-sectional view of the simulated electric field distribution of the Ag NP/VO_2 systems under the incident light with wavelength of 405 nm (Figure 3.14a-d), 663 nm (Figure 3.14b-e), and 1000 nm (Figure 3.14c-f). When the Ag NP/VO_2 systems were illuminated by the incident light of 405 nm, the magnitude of field enhancement is negligible and the enhanced electric field is sparsely distributed at the incident surface of Ag NP rather than at the interface between Ag NP and VO_2 layer. However, when the wavelength of incident light is 663 nm (Figure 3.14b-e), and 1000 nm (Figure 3.14c-f), electric field distribution of the LSPR at the interface of Ag NP and VO_2 layer was significantly enhanced. The

maximum field enhancement ($|E/E_0|$) at 663 nm and 1000 nm are 5.654 and 10.81, respectively, which are 2.5 and 5 times higher than that at 405 nm. The enhanced electric field at the interface of Ag NP and VO_2 indicates plasmon derived strong electron-electron coupling between Ag NP and VO_2 films. It is large enough to provoke MIT in VO_2 layer as enhanced electric field can affect electron-electron interaction in VO_2 layer. The simulation results expect that a redshift of the surface plasmon resonance wavelength (λ_{SPR}). The considerable plasmon resonance frequency shift of Ag NP and high electric field enhancement in specific domain according to the wavelength highly supports that the strong electron-electron coupling occurs at the interface of Ag NP and VO_2 layer under the wide range of wavelengths. The above analysis provides a theoretical platform, photo-induced MIT in Ag NP/VO_2 systems can be provoked by a wide range of wavelengths, and shows the capability of daylight-induced MIT in Ag NP/VO_2 systems and their application in broadband photodetectors and smart windows.

FDTD simulations on Ag-decorated VO_2 nanord arrays

Based on FDTD simulation results of Ag NP/VO_2 systems, further simulations on porous VO_2 NRs were conducted. Due to the large surface-to-volume ratio and porosity of VO_2 NRs, Ag NPs can be well distributed on their overall surface, whereas only the top surface of dense planar VO_2 thin films can be decorated by Ag NPs. As a result, porous VO_2 NRs are expected to experience more field enhancement in a large area from LSPR than dense planar VO_2 thin films. To verify this hypothesis, electric field distributions in Ag-decorated porous VO_2 NRs was

simulated and compared with the case of Ag-decorated dense planar VO_2 thin films under incident light of 663 nm. The simulation results are displayed in Figure 3.15a and Figure 3.15b. The results were simulated based on TEM images of Ag-decorated porous VO_2 NRs and Ag-decorated dense planar VO_2 thin films (Figure 3.15c-d). The enhanced electric field in Ag-decorated porous VO_2 NRs is found on a larger area than that of dense planar VO_2 thin films due to a larger number of Ag NPs decorated on porous VO_2 NRs, This can be attributed to the top open surface of VO_2 NRs originating from elongated pores and a larger surface-to-volume ratio, enabling well-spread decoration of Ag NPs.

The transmittance spectra shown in Figure 3.16 were derived from the simulation of bare and Ag-decorated porous VO_2 NRs, and bare and Ag-decorated dense planar VO_2 thin films. Due to the porous nanostructure, the bare and Ag-decorated porous VO_2 NRs show higher transmittance than bare and Ag-decorated dense planar VO_2 thin films. Bare porous VO_2 NRs and bare dense planar VO_2 thin films show higher transmittance than Ag-decorated porous VO_2 NRs and Ag-decorated dense planar VO_2 thin films, respectively. The transmittance difference between Ag-decorated and bare VO_2 NRs or dense planar thin films means additional light absorption by LSPR. That allows us to determine how much Ag NPs decoration affect the broadband photoresponse on porous VO_2 NRs and dense planar VO_2 thin films, respectively. The difference in transmittance between Ag-decorated and bare porous VO_2 NRs is larger than that between Ag-decorated and bare dense planar VO_2 thin films at wavelengths from 400 nm to 1000 nm. The results above show that Ag-decorated porous VO_2 NRs are great candidates for broadband photodetectors

operated by photo-induced MIT due to the strong electron-electron interaction with Ag NPs and VO_2.

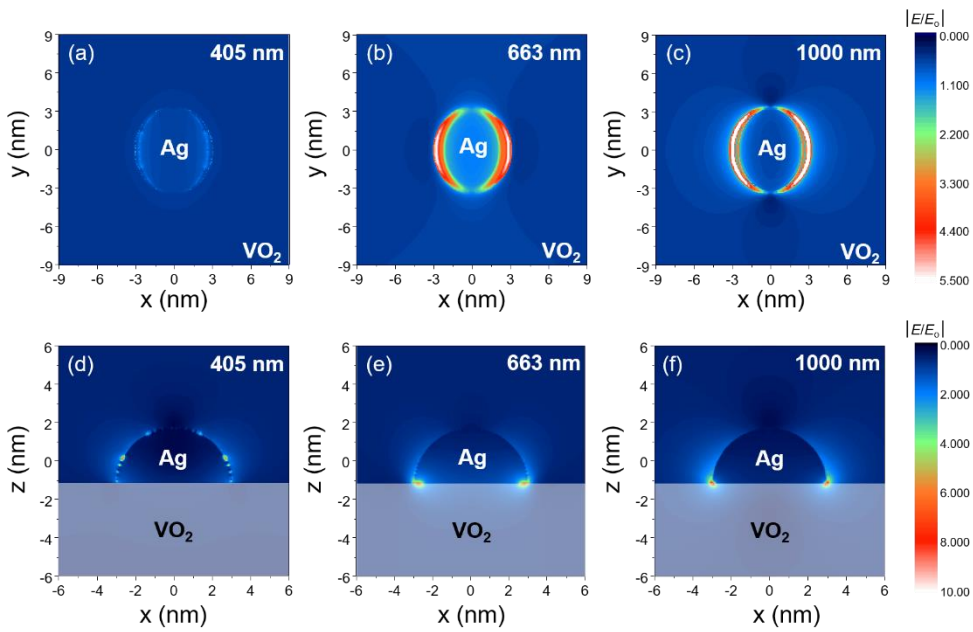

Figure 3.14. Top view of electric field distribution Ag NP/VO_2 systems under the incident light of wavelength (a) 405 nm, (b) 663 nm, and (c) 1000 nm. Cross-sectional view of electric filed distribution Ag NP/VO_2 systems under the incident light of wavelength (d) 405 nm, (e) 663 nm, and (f) 1000 nm.

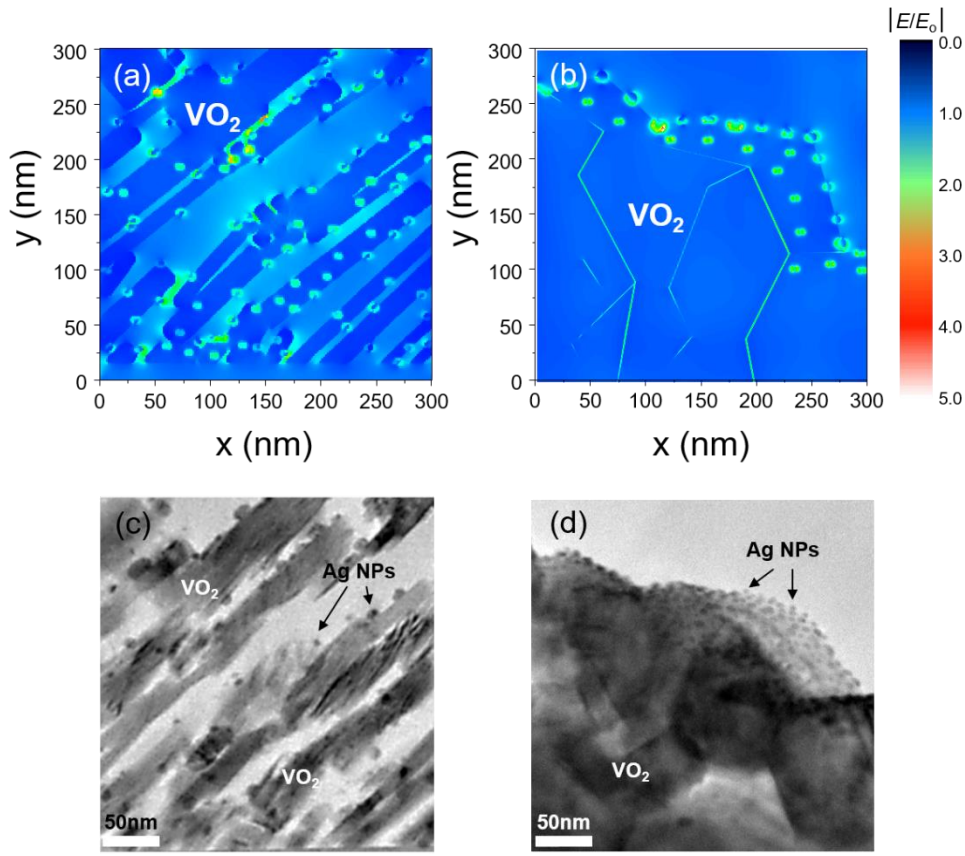

Figure 3.15. (a) Electric field distribution in the Ag-decorated porous VO_2 NRs and (b) the Ag-decorated dense planar VO_2 thin films. TEM images of (c) Ag-deocrated porous VO_2 NRs and (d) Ag-decorated VO_2 dense planar thin films used for FDTD simulations.

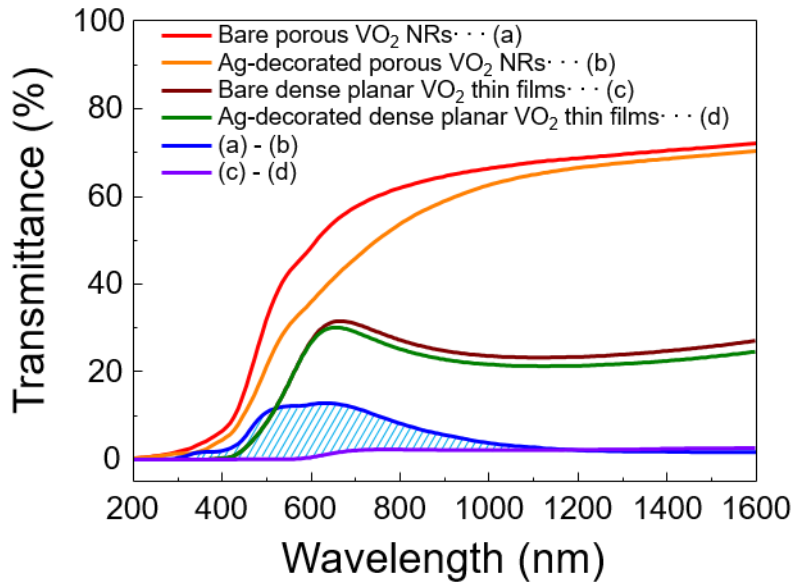

Figure 3.16. Simulated transmittance spectra from 200 nm to 1600 nm.

3.3.4. Enhanced broadband photoresponse performance of Ag-decorated VO_2 nanorod arrays and photo-induced metal-insulator transition

Enhanced photoresponse of Ag-decorated VO_2 nanorod arrays

To investigate photoresponse of our device, the photo and dark *I-V* characteristics of the Ag-decorated porous VO_2 NRs were measured in the dark and under white light illumination with various intensities from 10 μW cm^{-2} to 10 mW cm^{-2}, as shown in Figure 3.17a. The dark and photocurrent of the Ag-decorated porous VO_2 NRs show nonlinear and asymmetric *I-V* characteristics, which means unequal Schottky (rectifying) barriers are formed between two electrical contacts. These back-to-back Schottky contacts were affected by the Pt/VO_2 interface and some defects at the surface of the devices. The photocurrent of the device increased at applied bias larger than ±3 V because the Poole-Frenkel emission in the Ag-decorated porous VO_2 NRs became more severe in higher applied bias. At the same applied bias, the photocurrent increased gradually with the increase of light intensity. To determine the relationship between photocurrent and light intensities, the photocurrent measured at 10 V was plotted as a function of light intensity Figure 3.17b. The photocurrent can be fitted to the power law $I_{photo} \propto L^{0.51}$, where I_{photo} is the photocurrent and L is the light intensity. The dark and photo *I-V* characteristics of the reference samples were also measured in the dark and under the white light 5 mW cm^{-2}, respectively (Figure 3.18). Unlike the device based on Ag-decorated porous VO_2 NRs, other devices showed a negligible increase of photocurrent

compared with the dark current. Based on these results, it can be concluded that the intrinsic photogenerated carriers are too small to provoke MIT in VO_2, and Ag NPs should be decorated on the whole surface of VO_2 thin films. The ratio of the resistance of the device in the dark (R_{dark}) to the resistance of the device under white light illumination (R_{photo}) at the applied bias of 5 V is plotted as a function of light intensities as shown in Figure 3.19. The Ag-decorated porous VO_2 NRs showed slight increase R_{dark}/R_{photo} ratios until 50 μW cm^{-2}, whereas other devices showed negligible R_{dark}/R_{photo} ratios. Above 50 μW cm^{-2} of white light intensities, only the device based Ag-decorated porous VO_2 NRs showed a gradual increment of R_{dark}/R_{photo} as the intensity of light increases up to 10 mW cm^{-2}. The other devices still showed negligible increase of R_{dark}/R_{photo} less than 1.3. The ratio of resistance change by the light illumination with 10 mW cm^{-2} is 40.1 and this is similar to the ratio of resistance change by thermally induced MIT (47.01 as shown in Figure 13a). The result indicates that the white light illumination triggers MIT in the Ag-decorated porous VO_2 NRs. We emphasize that no results have been reported that photo-induced MIT in VO_2 is triggered by visible light at a low intensity of 10 mW cm^{-2} (AM 1.5G 0.1 sun condition). It can be concluded that the whole Ag-decorated porous VO_2 NRs in the device underwent photo-induced MIT above 10 mW cm^{-2}.

Broadband photoresponse

In order to compare experimental data with the FDTD simulation results, the broadband photoresponse of our devices was measured under the illumination of light wavelengths from 400 nm to 1000 nm, and white light (AM 1.5G 5 mW cm^{-2})

at V_{ex} of 5 V. Figure 3.20a shows the transient photoresponse results for our devices with exposure to incident light of various wavelengths from 400 nm to 1000 nm. The device based on Ag-decorated porous VO_2 NRs showed a higher photoresponse than other devices. To evaluate the broadband photoresponse ability of our device, responsivity (R_λ) and external quantum efficiency (EQE), which are two main figure-of-merits for broadband photodetectors, were plotted as a function of the wavelength of incident light as shown in Figure 3.20b. The broadband photoresponse of our device demonstrated the responsivities ranging from 46 A W^{-1} to 936 A W^{-1}. The device showed wavelength dependent R_λ, as the maximum field enhancement varies with wavelength in the FDTD simulation results. These results indicate that the R_λ of our device was influenced by the magnitude of the enhanced electric field of LSPR at the interface of Ag NPs and VO_2 thin films. The EQE of our device showed the range from 142 % to 1357 %. Since EQE is related to R_λ, the wavelength dependent EQE shows a similar tendency to responsivity.

Figure-of-merits of Ag-decorated porous VO_2 nanorod arrays based photodetector

To evaluate the performance of our device, R_λ, EQE, and detectivity (D^*) (see Experimental section for used equation) were also estimated under 532 nm laser illumination with various light intensities (Figure 3.21a-c). The value of R_λ, EQE, and D^* are 4.1×10^3 A W^{-1}, 9.6×10^5 %, and 1.4×10^{14} Jones, respectively. The rise time (t_r) and fall time (t_f), which are also key figure-of-merits, of the device were deduced from transient photocurrent measurement under the illumination with white light of 5 mW cm^{-2}, as shown in Figure 3.21d. The t_r and t_f of the device are defined as the

time required to reach 90% of the saturated value to the initial value, and vice versa. The t_r and t_f of our device were 1.44 ms and 4.97 ms, respectively. In order to compare the photoresponse performance of our device with that of previously reported two-dimensional materials-based broadband photodetectors, hybrid perovskites-based broadband photodetectors, which have been intensively researched in recent years, and vanadium oxide single nanorod-based photodetectors, R_λ, EQE, D^*, t_r, and t_f were summarized in Table 3.1. Our device based on Ag-decorated porous VO_2 NRs showed higher value of R_λ, EQE, and D^*, faster t_r, and t_f when compared with graphene,[45] MoS_2,[46] graphene oxide,[47] and hybrid perovskite[48-52] based broadband photodetector. For the previously reported vanadium dioxide based photodetectors,[23,24,26,53] the photodetectors could detect only a short range of wavelengths such as UV only or IR only photodetector and there have been no reports of broadband photodetector based on vanadium dioxide. However, our device can detect a wide range of wavelengths including visible light and show higher R_λ, EQE, and D^* and faster t_r and t_f than previously reported vanadium oxide based photodetector. The superior performance of our device resulted from a high on/off ratio, which originates from LSPR assisted photo-induced MIT. Based on these results, the Ag-decorated porous VO_2 NRs are believed to be promising candidates as materials for future optoelectronic devices.

Reliability and response speed are also important parameters to evaluate the performance of broadband photodetectors. The photosensitivity (see Experimental section for used equations) of Ag-decorated porous VO_2 NRs was measured at an applied bias of 5 V during repetitive on/off switching of light illumination of 5 mW cm^{-2}, as shown in Figure 3.22a. Our device showed reliable photosensitivity and

excellent photocurrent stability without performance degradation. The long-term stability test was also performed in air for 200 days (Figure 3.22b). The photosensitivity of the Ag-decorated porous VO_2 NRs was maintained the initial value without perceptible changes over the period. The working mechanism of previously reported single VO_2 nano- and micro-wire based UV photodetectors[23,24] as well as metal oxide NRs based photodetectors[54,55] is explained by O_2 adsorption/desorption. This mechanism will lead to performance degradation and poor reliability when the device is operated in oxygen deficient environments. In contrast, since the operating mechanism of our device is LSPR assisted photo-induced MIT in VO_2, reliable photoresponse performance of our device is expected regardless of its working environment. Therefore, we measured the dark and photo *I-V* characteristics, and photosensitivity of our device in various environments, such as N_2, O_2, air, and vacuum, with applied bias of 5 V under white light exposure of 5 mW cm^{-2} (Figure 3.23). The device did not show significant performance degradation under various working condition. These results demonstrate the reliability of our device and further support that the working mechanism of our device is photo-induced MIT with assistance of LSPR.

In addition, photo-induced MIT in VO_2 with the assistance of LSPR can serve as a valuable proof-of-concept for next generation smart windows. As VO_2 exhibit significant optical transmittance change across the MIT, there have been many reports on VO_2 based smart windows.[56-63] Most of previous studies are thermochromic smart windows, which are passively response to external environment,[47-52] and few electrochromic smart windows with high power consumption per unit area (> 10 W cm^{-2}).[52,63] On the other hand, using the photo-

induced MIT in VO_2 with the assistance of LSPR, an active smart window of low power consumption and fast switching can be realized. Comparing with previous reported smart windows (Table 3.2),[63-72] low power consumption (15 μW cm^{-2}) and fast switching for block state (1.4 ms) and transparent state (4.97 ms) can be expected if Ag-decorated porous VO_2 NRs are applied to smart windows. Moreover, MIT in the Ag-decorated porous VO_2 NRs can be triggered by visible light illumination, allowing smart windows actively respond to external environmental changes and block infrared light efficiently without loss of transmittance of visible light. Therefore, we expect that our strategy, photo-induced MIT with the assistance of LSPR, will paves a new route to realize a next generation smart window with active solar modulating ability, low power consumption, and fast switching speed.

Temperature dependence of resistance

The electronic state of materials can be determined by the temperature dependence of resistance.[73] In order to determine whether the photoresponse of our device results from photo-induced MIT, we measured the resistance of Ag-decorated porous VO_2 NRs in the dark and under illumination (white light 5mW cm^{-2}) with varying the temperature from 100 K to 300 K, as shown in Figure 3.24. In the dark, the resistance of Ag-decorated porous VO_2 NRs decreases with increasing temperature and showing the insulating behavior ($dR/dT < 0$). On the other hand, under illumination, the resistance of Ag-decorated porous VO_2 NRs drops to the low resistance state increases with increasing temperature, showing the metallic-like

behavior (dR/dT > 0). These results clearly show that photo-induced MIT occurs in Ag-decorated porous VO_2 NRs and MIT in VO_2 can be induced by visible light.

Thickness effects on photoresponse of Ag-decorated VO_2 nanorod arrays

With increasing the thickness of NRs, nanorods have longer length and larger diameter of nanorods, which indicates that the porosity, surface-to-volume ratio, and top open structure of NRs can change.[74] As Ag NPs are deposited thorough the top surface of porous VO_2 NRs, the thickness of porous VO_2 NRs can make impacts on the way in which Ag NPs are decorated with VO_2 nanorods and the photoresponse performance of the device. To investigate how the thickness of porous VO_2 NRs affects the photoresponse of the device, Ag-decorated porous VO_2 NRs with a thickness of 100 nm to 700 nm were prepared. For Ag-decorated VO_2 NRs less than 100 nm, the VO_2 nanorods become agglomeration and the porous nanostructure was completely destroyed (Figure 3.25a,b). Therefore, the Ag-decorated porous VO_2 NRs of less than 100 nm show similar dark and photo *I-V* characteristics to the SiO_2/Si substrate (Figure 3.25c,d). For Ag-decorated VO_2 NRs more than 100 nm, the sizes of the decorated Ag NPs are similar, but VO_2 nanorods with larger diameter can be observed and conglutination appears between VO_2 nanorods as the thickness of porous VO_2 NRs increases (Figure 3.26a-h).

Next, we examined the photoresponse characteristics of the Ag-decorated porous VO_2 NRs with the thicknesses more than 100 nm under illumination of varied light intensities. Figure 3.27 shows the R_{dark}/R_{photo} as a function of incident light intensities for 4 samples with the thicknesses of 150 nm, 250 nm, 350 nm, and 700 nm. The

photoresponse of the devices decreases with increasing thickness, and the device with thickness of 700 nm showed negligible photoresponse. The photocurrent of the device with thickness of 150 nm, 250 nm, 350 nm and 700 nm can be fitted to the power law $I_{photo} \propto L^{0.67}$, $I_{photo} \propto L^{0.51}$, $I_{photo} \propto L^{0.40}$, and $I_{photo} \propto L^{0.0004}$, respectively. The critical light intensities for photo-induced MIT of the devices with thickness of 150 nm, 250 nm, 350 nm devices were 134 μW cm^{-2}, 234 μW cm^{-2}, and 794 μW cm^{-2}, respectively. The critical light intensity for photo-induced MIT of each device was determined by Gaussian curve fitting to the derivatives of $\log(d(R_{dark}/R_{photo})/d(\log L)$. The change of photoresponse depending on the film thickness is related with the change of VO_2 nanorods diameter. When the diameter of VO_2 nanorods becomes thicker, it is difficult for electric fields, which are generated at the interface between Ag NPs and VO_2 nanorods, to influence the inside of the VO_2 nanorods. The enhanced shadow effect with increasing the thickness of thin film is another contributing factor for the reduced photoresponse because Ag NPs can be decorated on the top surface of VO_2 NRs. The partially decoration of Ag NPs on the surface of VO_2 nanorods, which originated from enhanced shadow effect with increasing the thickness of the thin film, is another contributing factor for the reduced photoresponse. Therefore, to obtain high photoresponsive Ag-decorated porous VO_2 NRs, VO_2 nanorods should have narrow diameters to be well-affected by LSPR, and Ag NPs should be well decorated throughout the VO_2 nanorods.

LSPR effects on photo-induced MIT: Phase transition in Ag-decorated VO_2 NRs

As the passage of a fast electron can excite localized plasmons in metallic nanoparticles,[75] the LSPR effect on photo-induced MIT in Ag-decorated VO_2 NRs was investigated using transmission electron microscope (TEM). Across the MIT, the crystal structure of VO_2 changes from monoclinic (insulating state) to tetragonal (metallic state) structure. Therefore, the effect of LSPR effect on MIT in VO_2 can be confirmed by the comparing crystal structure of VO_2 nanorod with and without Ag NP. Figure 3.28a shows the HRTEM image of VO_2 nanorod without Ag NP. For the structure analysis, we used fast Fourier transform (FFT) providing a diffraction pattern of the nm-scale area. Figure 3.28b is FFT of the red rectangle in Figure 3. 28a. As seen in Figure 3.28b, typical monoclinic diffraction pattern, which has a $[01\bar{1}]$ zone axis of the M_1 phase, can be observed. It means that the VO_2 nanorod exhibits insulating state. On the other hand, Figure 3.28d, which is FFT of the orange rectangle in Figure 3.28c (VO_2 nanorod with Ag NP), shows the tetragonal diffraction pattern of the T$[111]$ zone axis. It indicates that LSPR from Ag NP can provoke MIT in VO_2 nanorod. From the above results, it is clearly shown that LSPR from Ag NP can provoke photo-induced MIT in VO_2.

Schematic illustration of Mechanisms

Based on these results, the operating mechanism of our device can be explained by the brief band structure of VO_2 near the Fermi level, as shown in Figure 3.28a. When the VO_2 is at its electrically insulating state, VO_2 possesses a monoclinic crystalline structure. For the monoclinic phase of VO_2, there exist short and long distances between V atoms due to the formation of V-V dimers, which results in the

localization of *d*-orbital electrons. The short distances between V-V are 2.65 Å between the V-V dimers that split the nonbonding $3d_{\|}$ states into occupied $3d_{\|}$ (lower energy) and unoccupied $3d_{\|}^{*}$ states (higher energy). The long distances of V-V are 3.12 Å between zigzag chains of the V-V pairs that create $3d_{\pi}^{*}$ states that are upshifted above $3d_{\|}$ states and the Fermi energy (E_F). As a result, the monoclinic phase of VO_2 has a band gap of 0.7 eV.[5,24]

As Nakano *et al*. reported that electrostatic charging at a surface of VO_2 can trigger MIT in VO_2,[6] the electric field enhancement, which is generated at the interface of Ag NPs and porous VO_2 NRs under the illumination, can provoke photo-induced MIT. When the device is illuminated, a strong electric field is generated at the interface of Ag NPs and porous VO_2 NRs due to strong coupling that originates from LSPR. The enhanced electric field at the interface of Ag NPs and porous VO_2 NRs affects the electronic state of VO_2. When the electric fields generated by LSPR, are sufficient large to provoke MIT in VO_2, the electronic state of VO_2 changes from insulating state to metallic state as shown in Figure 3.28b. During MIT, the $3d_{\|}^{*}$ state and $3d_{\|}$ state merge and form the conduction band with $3d_{\pi}^{*}$ state. Consequently, the monoclinic insulating state of VO_2 is converted into the rutile structure of VO_2, which is a metallic phase. The parallel alignment of V atoms along c_R leads to *d*-orbital electrons being shared by all of the metallic V atoms, and the Fermi level is positioned on an overlapped region between $3d_{\pi}^{*}$ and $3d_{\|}$. Although plasmonic heating, originating from electron-phonon coupling, can be another possible mechanism, the incident light intensity used in this work (sub-mW cm^{-2} scale) is too weak to generate sufficient heat by the plasmonic nanoparticles for provoking MIT

in VO_2.[76,77] Therefore, it can be concluded that our device showed the metallic phase of VO_2 due to LSPR assisted photo-induced MIT in VO_2.

The novel physical properties of correlated oxides that originate from electron-electron interactions are difficult to apply in a practical device, yet they allow to go beyond the limits of conventional devices. Our approach to apply such novel physical properties of correlated oxide in a device will open up the way to future devices (i) by introducing functional layers or particles on the surface of correlated oxide that affect electronic-electronic interactions in correlated oxide and (ii) by preparing correlated oxide in form of nanostructured thin films to maximize the influence from the functional layer or particles.

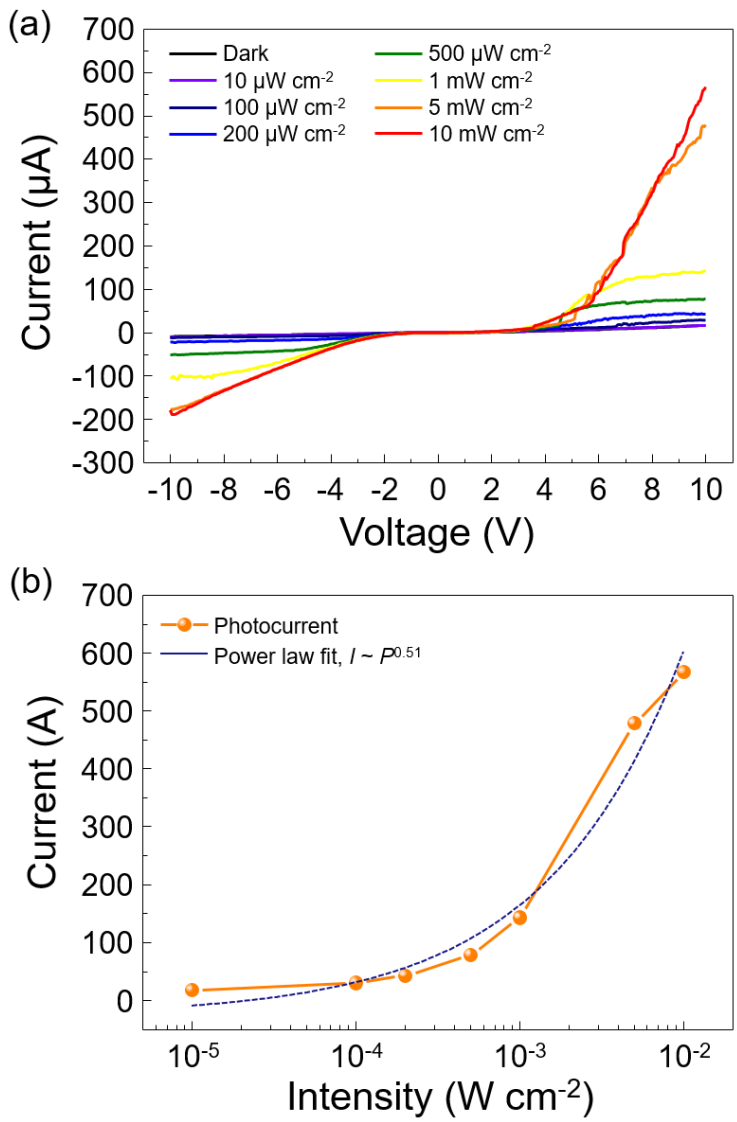

Figure 3.17. (a) *I-V* characteristics of the Ag-decorated porous VO_2 NRs under various intensities of white light. (b) The photocurrent of Ag-decorated porous VO_2 NRs measured with external bias of 10 V plotted as a function of light intensity. The graph is fitted by the power law $I_{photo} \propto L_{light}^{0.51}$

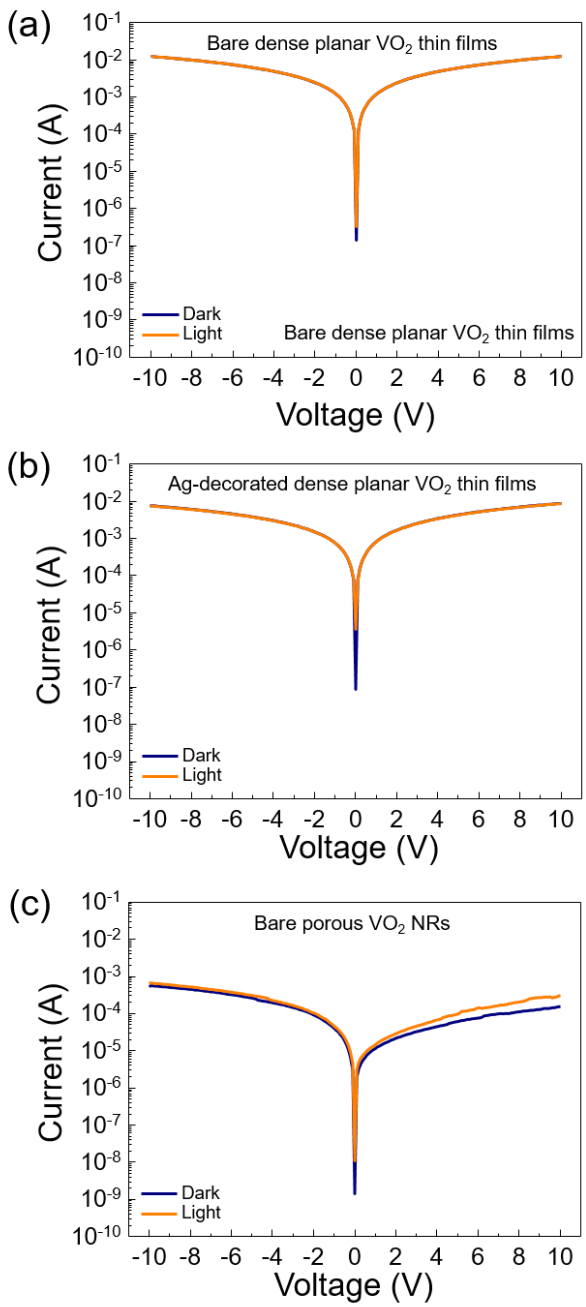

Figure 3.18. The dark and photo *I-V* characteristics under the illumination of white light 5 mW cm^{-2}: (a) Bare dense planar VO_2 thin film, (b) Ag-decorated dense planar VO_2 thin film, and (c) bare porous VO_2 NRs.

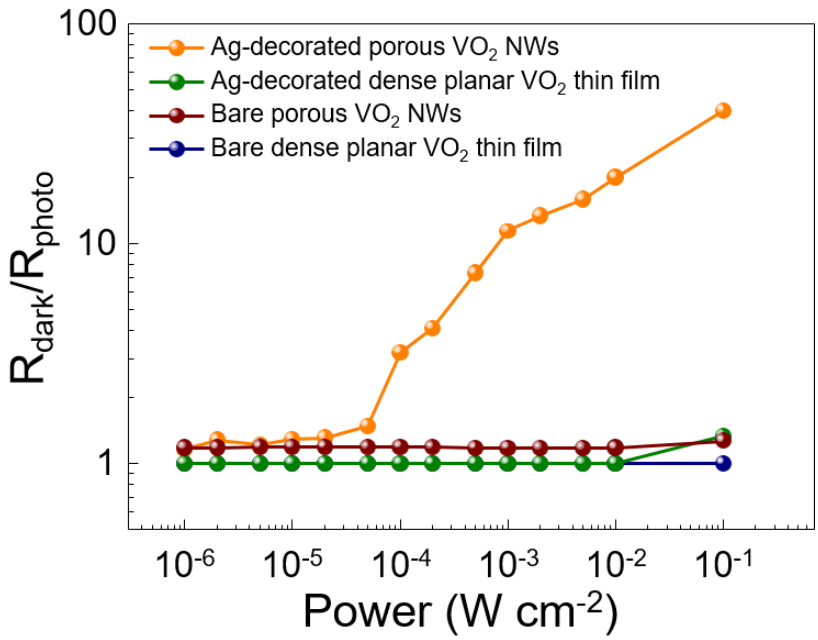

Figure 3.19. The R_{dark}/R_{photo} of the devices as a function of light intensity

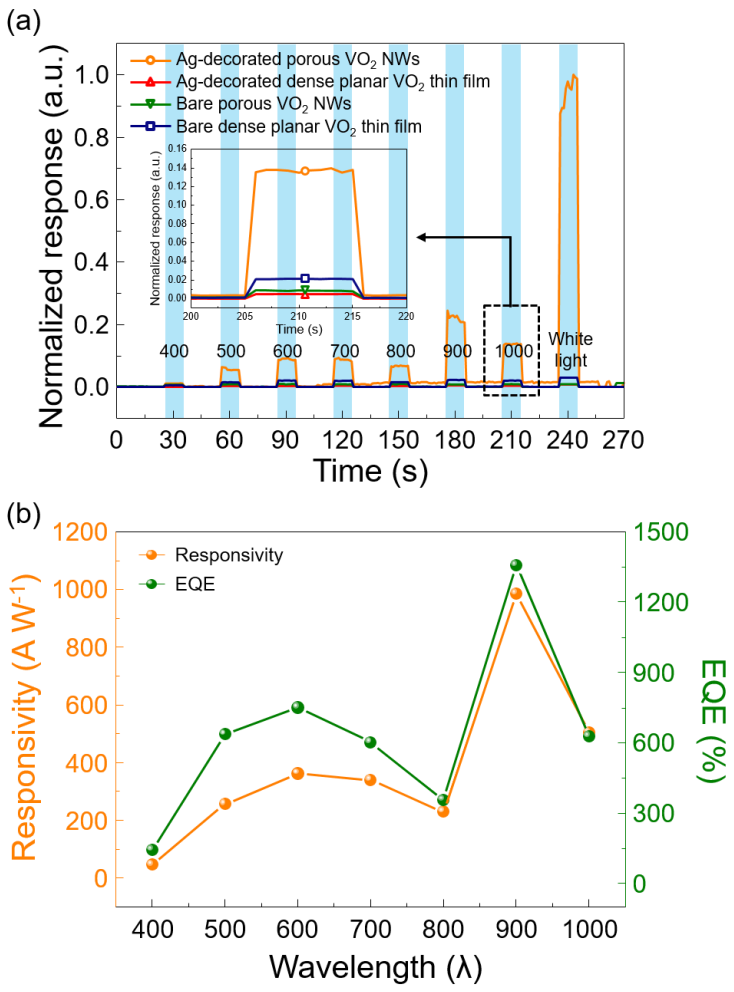

Figure 3.20. (a) The transient photocurrent of our devices with incident light of various wavelengths. (b) Spectral responsivity and EQE of the device based on the Ag-decorated porous VO_2 NRs.

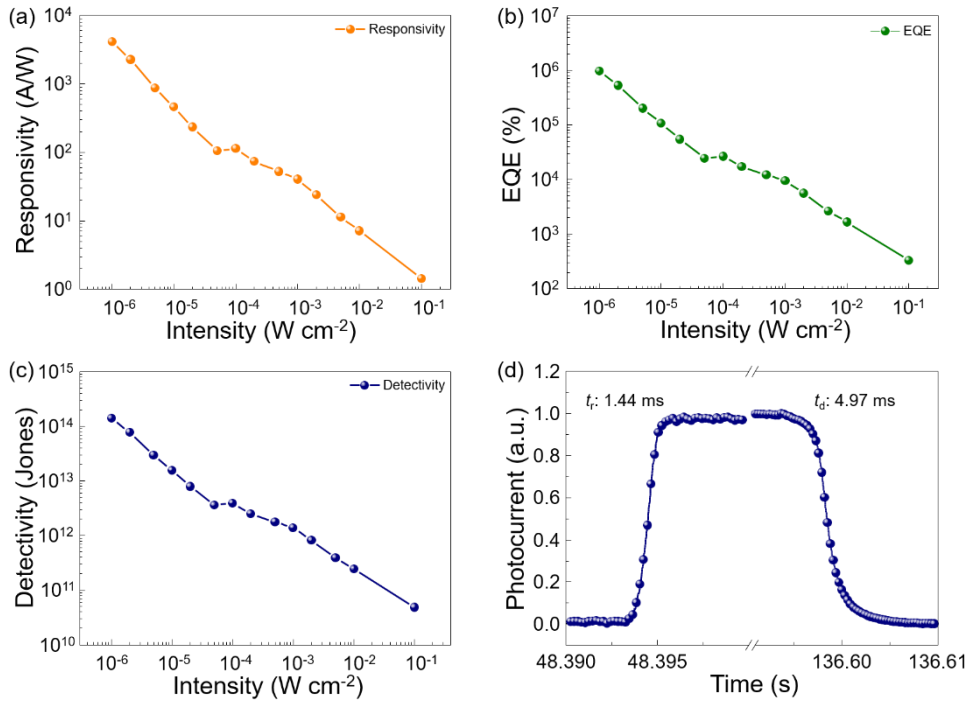

Figure 3.21. (a) The responsivity, (b) external quantum efficiency, and (c) detectivity of the Ag-decorated porous VO_2 NRs under 532 nm laser illumination as a function of light intensities. (d) Time resolved photoresponse of the Ag-decorated porous VO_2 NRs.

Table 3.1. Comparison of the figure-of-merits for broadband photodetectors and vanadium oxide based photodetector from previous reports and the present work.

Materials	Detectable wavenlength	Responsivity (A W^{-1})	EQE (%)	Response Time	Recovery time	Specific Detectivity (Jones)	Ref.
Graphene	532 nm ~ 10 μm	8.61	2×10^{3}	8×10^{4} ms	1.5×10^{5} ms	N/A	45
MoS_2	400 nm ~ 600 nm	3.0	7×10^{2}	N/A	N/A	8×10^{11}	46
Graphene oxide	IR	4×10^{-3}	3×10^{-1}	26	29	N/A	47
$CH_3NH_3PbI_3$ thin film	365 nm ~ 780 nm	7.0	1.1×10^{3}	t < 200 ms	t < 200 ms	N/A	48
$CH_3NH_3PbI_3$ nanowire array	400 nm ~ 780 nm	8×10^{-1}	1.5×10^{2}	0.2 ms	0.3 ms	3.0×10^{12}	49
$Cs_x(CH_3NH_3)_{1-x}PbI_3$ nanowire	500 nm ~ 850 nm	23.0	5.3×10^{3}	N/A	N/A	2.5×10^{11}	50
$CH_3NH_3PbI_3$ network	400 nm ~ 780 nm	9×10^{-1}	1.7×10^{2}	0.3 ms	0.4 ms	N/A	51
CdS nanorod array/rGO	530 nm ~ 1450 nm	5.8×10^{-4}	1.9×10^{-1}	1.3 ms	1.7 ms	7.2×10^{11}	52
$CH_3NH_3PbI_3$/ZnO nanorod array	400 nm ~ 600 nm	24.3	6.0×10^{3}	700 ms	600 ms	3.5×10^{14}	53
VO_2 single microwire	365 nm	7×10^{3}	3.6×10^{7}	126 ms	N/A	1.0×10^{14}	23
VO_2/V_2O_5 core-shell single nanorod	990 nm	2.08×10^{3}	3.5×10^{5}	230 ms	55 ms	9.23×10^{12}	26
V_2O_5 single nanowire	405 nm	4.8×10^{2}	1.3×10^{5}	N/A	N/A	N/A	54
Ag-decorated porous VO_2 NWs	**400 nm ~ 1000 nm**	**4.1×10^{3}**	**9.6×10^{5}**	**1.4 ms**	**4.97 ms**	**1.4×10^{14}**	**This work**

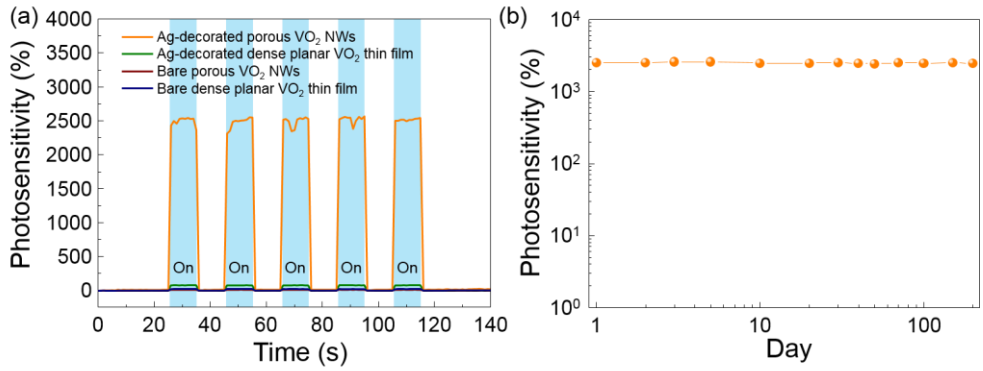

Figure 3.22. (a) Photo-switching characteristics of the device under alternating dark and light illumination (white light, 5 mW cm^{-2}). (b) The long-term stability test of the Ag-decorated porous VO_2 NRs in air for 200 days.

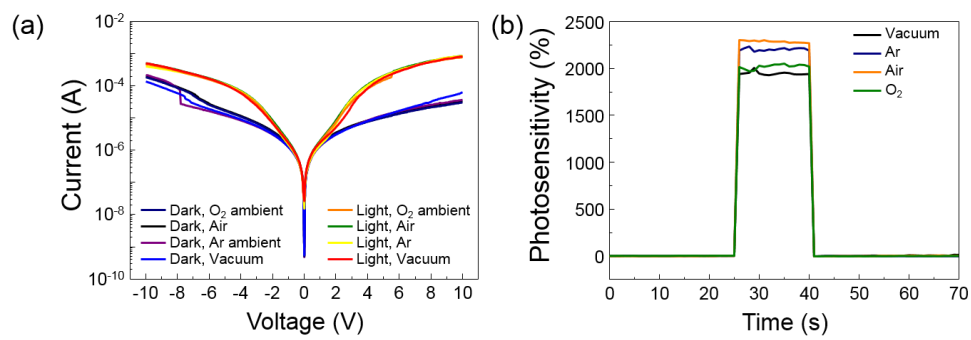

Figure 3.23. (a) The *I-V* characteristics of the Ag-decorated VO_2 porous NRs in various gas ambient. (b) The photo transient curve of the Ag-decorated porous VO_2 NRs in gas various ambient.

Table 3.2. Comparison of the power consumption per unit area and switching time of smart windows.

Materials	Power consumption per unit area	Switching time for blocking state	Switching time for transparent state	Ref
VO_2/Al:ZnO heterojuction	1×10^{4} mW cm^{-2}	-	-	63
Vanadium oxide	-	7 s	9.9 s	64
$W_{18}O_{49}$ powder	8.0×10^{-1} mW cm^{-2}	2.7 s	8 s	65
WO_3 nanoparticles	3 mW cm^{-2}	2.8 s	1.9 s	66
WO_3 nanorods	1.5 mW cm^{-2}	80 s	188 s	67
$[PSS(PEI/PSS)_3(PEI/W_{18}O_{49})_{30}/(PEI/P_8W_{48})_{20}]$	3.5×10^{-1} mW cm^{-2}	26 s	86 s	68
NiO and WO_3	-	10 s	13.1 s	69
vacancy-doped WO_3 and amorphous Nb_2O_5	4.5×10^{-1} mW cm^{-2}	180 s	30 s	70
Al:ZnO	3×10^{-3} mW cm^{-2}	0.19 s	0.16 s	71
π-conjugated polymers	5×10^{-2} mW cm^{-2}	0.7 s	1.7 s	72
Ag-decorated porous VO_2 NWs	1.5×10^{-2} mW cm^{-2}	1.4×10^{-3} s	4.97×10^{-3} s	This work

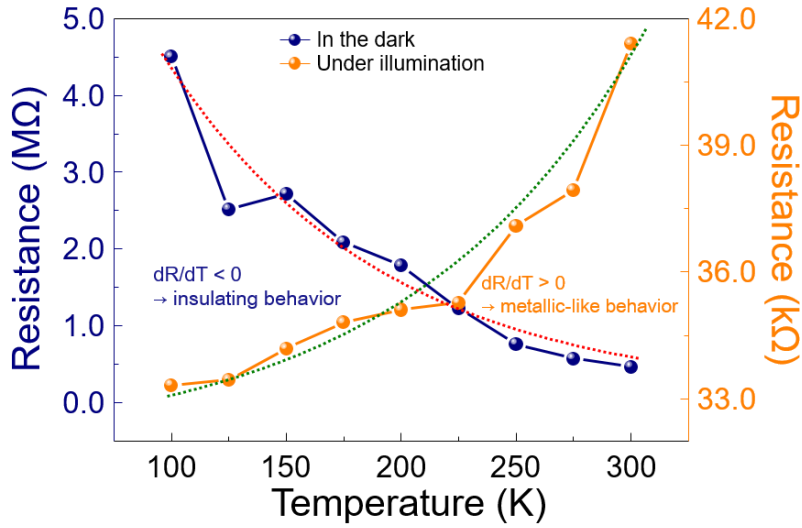

Figure 3.24. The resistance of the Ag-decorated porous VO_2 NRs with thickness of 250 nm in the dark and under the illumination as a function of temperature.

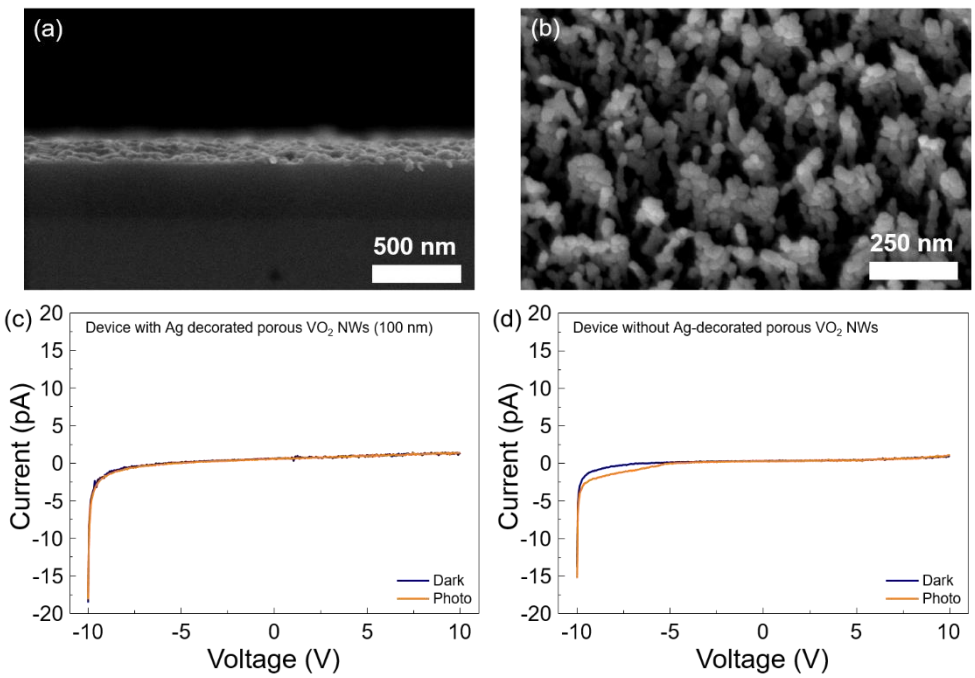

Figure 3.25. Top view and cross-sectional view SEM images of Ag-decorated porous VO_2 NRs deposited less than 100 nm. The completely destroyed nanostructure of Ag-decorated porous VO_2 NRs were observed. Dark and photo *I-V* characteristics of 100 nm thick of (c) Ag-decorated porous VO_2 NRs and (d) SiO_2/Si substrate.

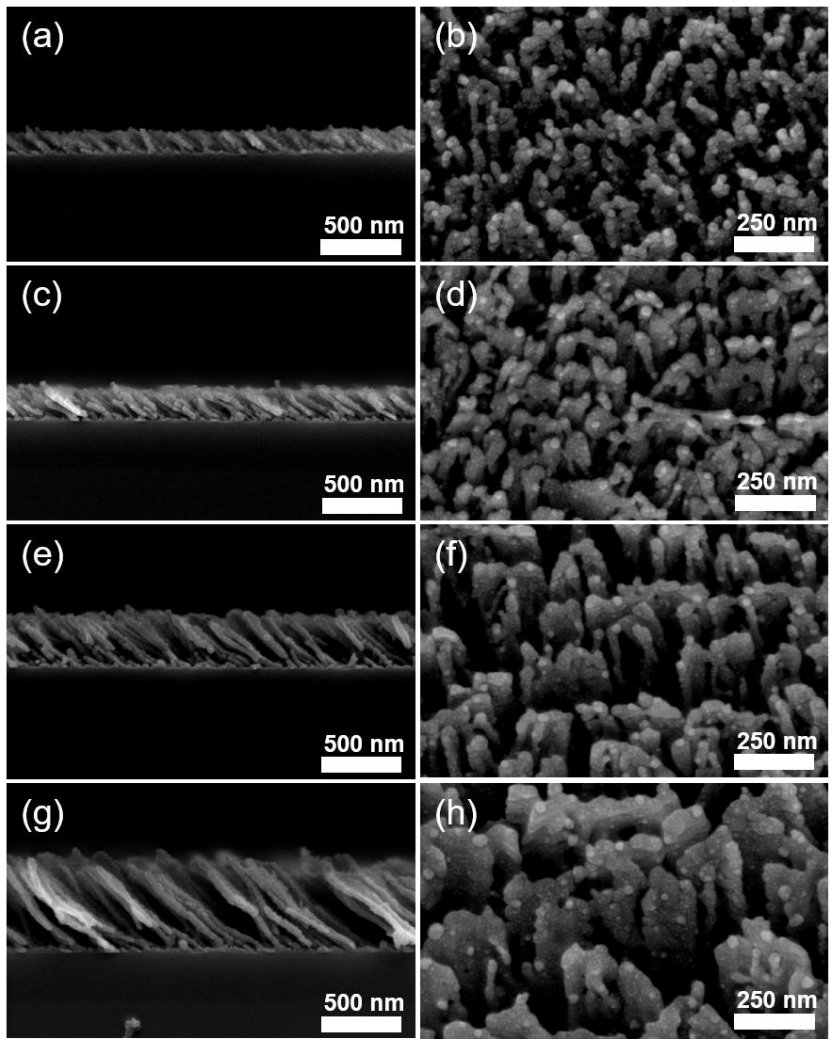

Figure 3.26. Top and cross-sectional view SEM images of Ag-decorated porous VO_2 NRs. (a,b) 150 nm, (c,d) 250 nm, (e,f) 350 nm, and (g,h) 700 nm-thick Ag decorated porous VO_2 NRs.

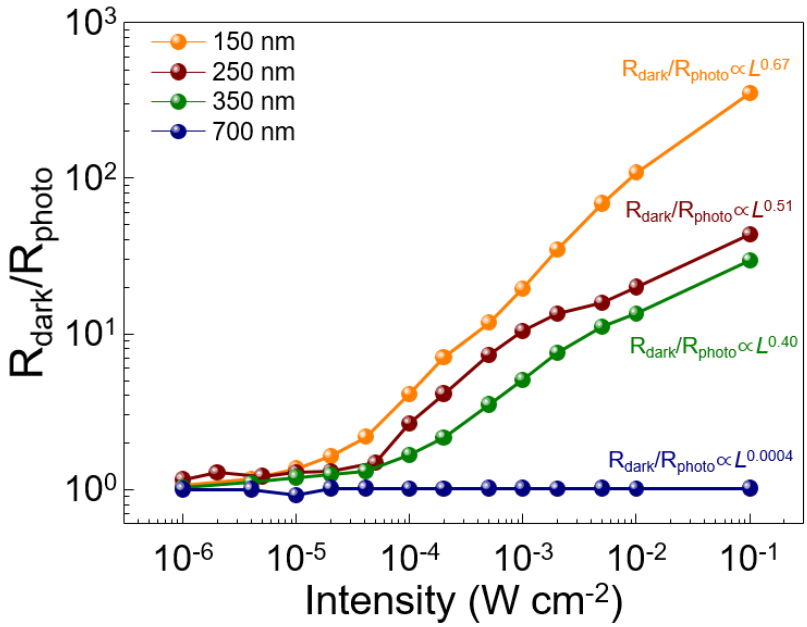

Figure 3.27. The R_{dark}/R_{photo} of the devices with the thicknesses of Ag-decorated porous VO_2 NRs ranging from 150 nm to 700.

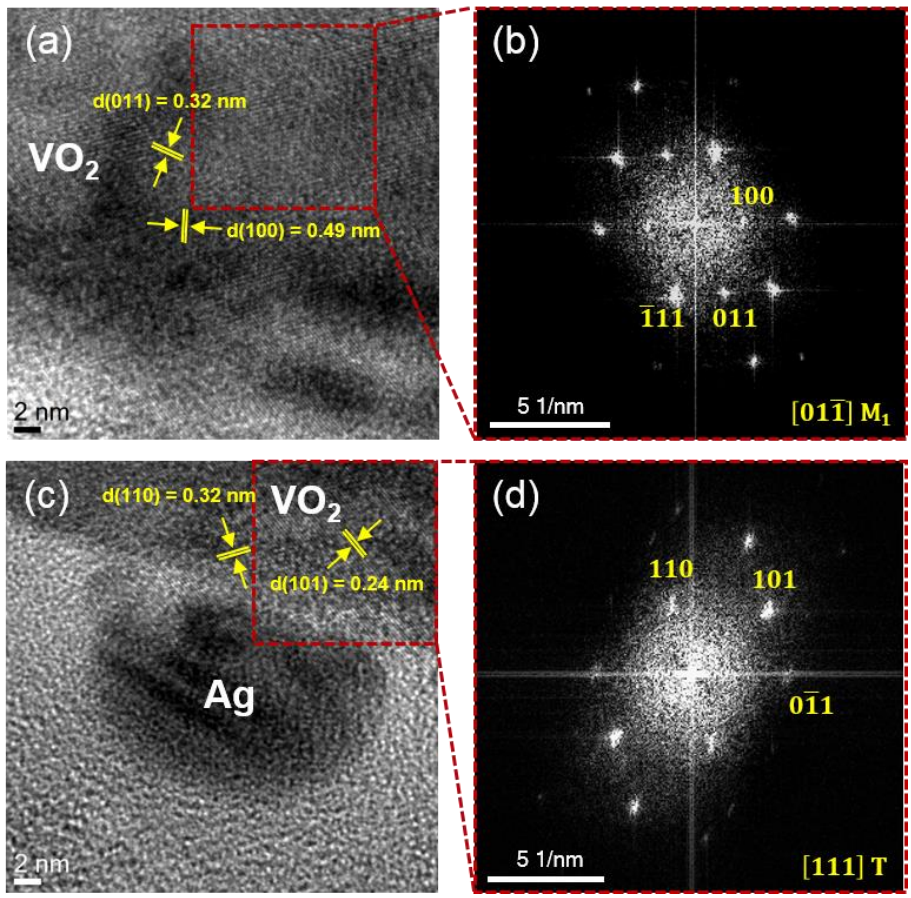

Figure 3.28. (a) A typical high magnification TEM image of VO_2 nanorod and (b) Monoclinic M_1 $[\mathbf{01\bar{1}}]$ (red rectangle) zone axis FFT. (c) A typical high magnification TEM image of Ag-decorated VO_2 nanorod. (d) Tetragonal R$[\mathbf{111}]$ (orange rectangle) zone axis FFT.

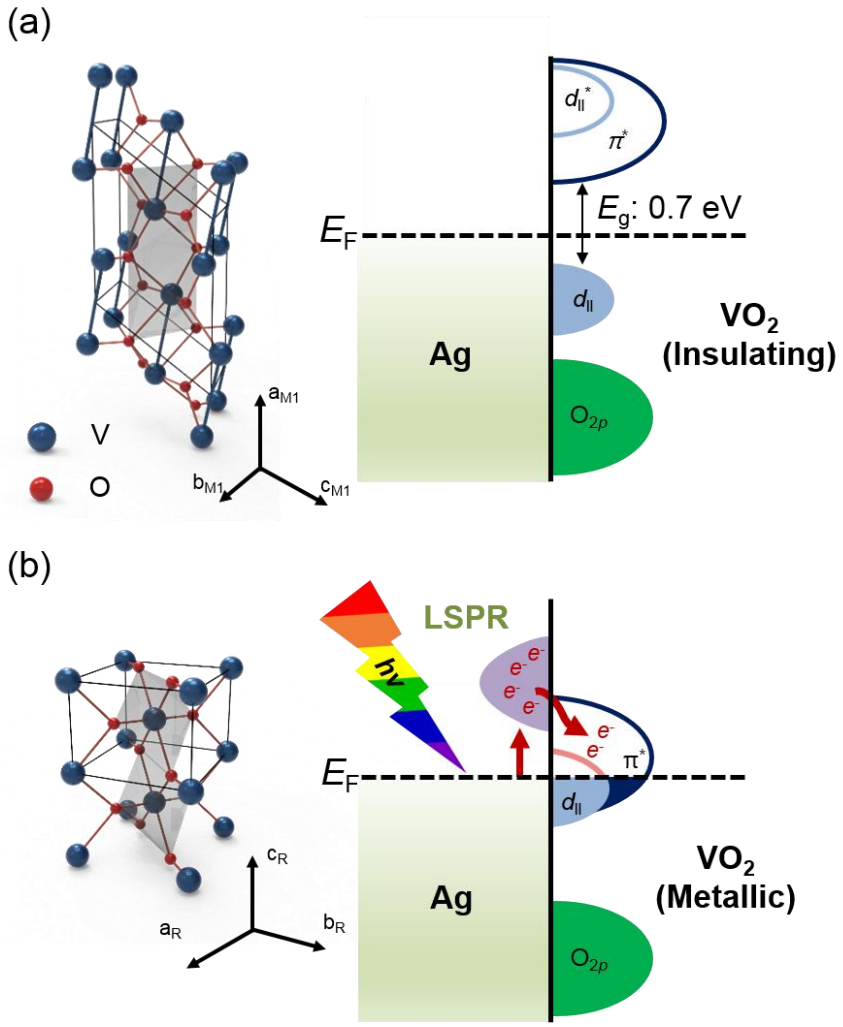

Figure 3.29. Schematics for the electronic structure of the Ag-decorated porous VO_2 NRs (a) in the dark and (b) under the illumination.

3.4. Conclusion

A novel broadband photodetector that operates via a LSPR assisted photo-induced MIT mechanism was demonstrated. The strong electric field at the interface between Ag NPs and VO_2 thin films, which originates from LSPR, causes VO_2 to response to a wide wavelength of incident light, spanning a wide range from 400 nm to 1000 nm. With porous VO_2 NRs, Ag NPs were well distributed throughout the film, so that the strong electric fields at the interface of Ag NPs and VO_2 thin films can affect the entire film to provoke photo-induced MIT in VO_2 NRs. This is the first report on broadband photodetectors based on VO_2 thin films and opens up the way to VO_2 in future optoelectronics.

3.5. Reference

[1] A. I. Bizdin, *Rev. Mod. Phys.* **2005**, *77*, 935.

[2] N. Banerjee, C. B. Smiet, R. G. J. Smits, A. Ozaeta, F. S. Bergeret, M. G. Blamire, J. W. A. Robinson, *Nat. Commun*. **2014**, 5, 3048.

[3] M. B. Salmon, M. Jaime, *Rev. Mod. Phys.* **2001**, *73*, 583.

[4] M. Imada, A. Fujimori, Y. Tokura, *Rev. Mod. Phys*. **1998**, *70*, 1039.

[5] J. B. Goodenough, *J. Solid state Chem.* **1971**, *3*, 490.

[6] M. Nakano, K. Shibuya, D. Okuyama, T. Hatano, S. Ono, M. Kawasaki, Y. Iwasa, Y. Tokura, *Nature* **2012**, *487*, 459.

[7] J. Jeong, N. Aetukuri, T. Graf, T. D. Schladt, M. G. Samant, S. S. P. Parkin, *Science* **2013**, *339*, 1402.

[8] A. O'Hara, A. A. Demkov, *Phys. Rev. B.* **2015**, *91*, 094305.

[9] T. Yajima, T. Nihimura, A. Toriumi, *Nat. Commun*. **2015**, *6*, 10104.

[10] A. Cavalleri, Cs. Tóth, C.W. Siders, J. A. Squier, F. Ráksi, P. Forget, J. C. Kieffer, *Phys. Rev. Lett.* **2001**, *87*, 237401.

[11] A. Cavalleri, Th. Dekorsy, H. H. W. Chong, J. C. Keffer, R. W. Schoenlein, *Phys. Rev. B*, **2004**, *70*, 161102(R).

[12] G. Xu, C.-M. Huang, M. Tazawa, P. Jin, D.-M. Chen, L. Miao, *Appl. Phys. Lett.* **2008**, *93*, 061911.

[13] G. Xu, Y. Chen, M. Tazawa, P. Jin, *J. Phys. Chem. B*, **2006**, *110*, 2051.

[14] L. Pellegrino, N. Manca, T. Kanki, H. Tanaka, M. Biasotti, E. Bellingeri, A. S. Siri, D. Marré, *Adv. Mater.* **2012**, *24*, 2929.

[15] G. Stefanovich, A. Pergament, D. Stefanovich, *J. Phys.: Condens. Matter*. **2000**, *12*, 8837.

[16] M.-J. Lee, Y. Park, D.-S. Suh, E.-H. Lee, S. Seo, D.-C. Kim, R. Jung, B.-S. Kang, S.-E. Ahn, C. B. Lee, D. H. Seo, Y.-K. Cha, I.-K. Yoo, J.-S. Kim, B, H, Park, *Adv. Mater.* **2007**, *19*, 3919.

[17] J. Cao, E. Ertekin, V. Srinivasan, W. Fan, S. Huang, H. Zheng, J. W. L. Yim, D. R. Khanal, D. F. Ogletree, J. C. Grossman, J. Wu, *Nat. Nanotech.* **2009**, *4*, 732.

[18] J. Wu, Q. Gu, B. S. Guiton, N. P. de Leon, L. Ouyang, H. Park, *Nano Lett*. **2006**, *10*, 2313.

[19] J. M. Baik, M. H. Kim, C. Larson, C. T. Yavuz, G. D. Stucky, A. M. Wodtke, M. Moskovits, *Nano Lett.* **2009**, *9*, 3980.

[20] E. Strelcov, Y. Lilach, A. Kolmakov, *Nano Lett*. **2009**, *9*, 2322.

[21] H. Kim, Y. Kim, K. S. Kim, H. Y. Jeong, A.-R. Jang, S. H. Han, D. H. Yoon, K. S. Suh, H. S. Shin, T. Kim, W. S. Yang, *ACS. Nano*, **2013**, *7*, 5769

[22] H. Coy, R. Cabrera, N. Sepulveda, F. E. Fernandez, *J. Appl. Phys.* **2010**, *108*, 113115.

[23] J. M. Wu, W. E. Chang, *ACS Appl. Mater. Interfaces* **2014**, *6*, 14286.

[24] J. M. Wu, L. B. Liou, *J. Mater. Chem.* **2011**, *21*, 5499.

[25] M. M. Qazilbash, K. S. Burch, D. Whisler, D. Shrekenhamer, B. G. Chae, H. T. Kim, D. N. Basov, *Phys. Rev. B.* **2006**, *74*, 205118.

[26] Z. Li, Z. Hu, J. Peng, C. Wu, Y. Yang, F. Feng, P. Gao, J. Yang, Y. Xie, *Adv. Funct. Mater.* **2014**, *24*, 1821.

[27] C. Clavero, *Nat. Photon.* **2014**, *8*, 95.

[28] M. L. Brongersma, N. J. Halas, P. Nordlander, *Nat. Nanotechnol.* **2015**, *10*, 25.

[29] G. Xu, C.-M. Huang, P. Jin, M. Tazawa, D.-M Chen, *J. Appl. Phys.* **2008**, *104*, 053101.

[30] G. Xu, C.-M. Huang, P. Jin, M. Tazawa, D.-M Chen, *J. Appl. Phys.* **2008**, *104*, 053102.

[31] H. Zheng, J. Wang, S. E. Lofland, Z. Ma, L. Mohaddes-Ardabili, T. Zhao, L. Salamanca-Riba, S. R. Shinde, S. B. Ogale, F. Bai, D. Viehland, Y. Jia, D. G. Schlom, M. Wuttig, A. Roytburd, R. Ramesh, *Science* **2004**, *303*, 661.

[32] Y. J. Chang, C. H. Koo, J. S. Yang, Y. S. Kim, D. H. Kim, J. S. Lee, T. W. Noh, H.-T. Kim, B. G. Chae, *Thin Solid Films* **2005**, *486*, 46.

[33] S. Naoki, T. Hidekazu, Y. Satoru, K. Masaki, L. B. Kuk, L. H. Yeon, K. Tomoji, *Small* **2008**, *4*, 1661.

[34] J. Z. Sun, D. J. Webb, M. Naito, K. Char, M. R. Hahn, J. W. P. Hsu, A. D. Kent, D. B. Mitzi, B. Oh, M. R. Beasley, T. H. Geballe, R. H. Hammond, A. Kapitulnik, *Phys. Rev. Lett*. **1987**, *58*, 1574.

[35] Z. Yang, C. Ko, S. Ramanathan, *Ann. Rev. Mater. Res.* **2011**, *41*, 337.

[36] N. B. Aetukuri, A. X. Gray, M. Drouard, M. Cossale, L. Gao, A. H. Reid, R. Kukreja, H. Ohldag, C. A. Jenkins, E. Arenholz, K. P. Roche, H. A. Dürr, M. G. Samant, S. S. P. Parkin, *Nat. Phys.* **2013**, *9*, 661.

[37] F. Nakamura, M. Sakaki, Y. Yamanaka, S. Tamaru, T. Suzuki, Y. Maeno, *Sci. Rep.* **2013**, *3*, 2536.

[38] Y. Tokura, *Phys. Today* **2003**, *56*, 50.

[39] J. Cao, E. Ertekin, V. Srinivasan, W. Fan, S. Huang, H. Zheng, J. W. L. Yim, D. R. Khanal, D. F. Ogletree, J. C. Grossman , J. Wu, *Nat. Nanotechnol.* **2009**, *4*, 732.

[40] J.-M. Jeon, Y.-S. Shim, S. D. Han, D. H. Kim, Y. H. Kim, C.-Y. Kang, J.-S. Kim, M. Kim, H. W. Jang, *J. Mater. Chem. A*. **2015**, *3*, 17939.

[41] H. G. Moon, Y.-S. Shim, D. H. Kim, H. Y. Jeong, M. Jeong, J. Y. Jung, S. M. Han, J. K. Kim, J.-S. Kim, H.-H. Park, J.-H. Lee, H. L. Tuller, S.-J. Yoon, H. W. Jang, *Sci. Rep.* **2012**, *2*, 588.

[42] A. Barranco, A. Borras, A. R. Gonzalez-Elipe, A. Palmero, *Prog. Mater. Sci.* **2016**, *76*, 59.

[43] Y. Sun, X. Xiao, G. Xu, G. Dong, G. Chai, H. Zhang, P.engyi Liu, H. Zhu, Y. Zhan, *Sci. Rep.* **2013**, *3*, 2756.

[44] S. D. Ganichev, E. Ziemann, W. Prettl, I. N. Yassievich, A. A. Istratov, E. R. Weber, *Phys. Rev. B* **2000**, *61*, 10361.

[45] Y. Zhang, T. Liu, B. Meng, X. Li, G. Liang, X. Hu, J. Wang, Nat. Commun. 2013. 4, 1811

[46] S. Mukherjee, R. Maiti, A. K. Katiyar, S. Das, S. K. Ray, *Sci. Rep.* **2016**, *6*, 29016.

[47] B. Chitara, L. S. Panchakarla, S. B. Krupanidhi, C. N. Rao, *Adv. Mater.* **2011**, *23*, 5419.

[48] X. Hu, X. Zhang, L. Liang, J. Bao, S. Li, W. Yang, Y. Xie, *Adv. Funct. Mater.* **2014***, 24*, 7373.

[49] H. Deng, D. Dong, K. Qiao, L. Bu, B. Li, D. Yang, H.-E. Wang, Y. Cheng, Z. Zhao, J. Tang, H. Song, *Nanoscale* **2015**, *7*, 4163.

[50] D. Dong, H. Deng, C. Hu, H. Song, K. Qiao, X. Yang, J. Zhang, F. Cai, J. Tang, H. Song, *Nanoscale* **2017**, 9, 1567.

[51] H. Deng, X. Yang, D. Dong, B. Li, D. Yang, S. Yuan, K. Qiao, Y.-B. Cheng, J. Tang, H. Song, *Nano Lett.* **2015**, 15, 7963.

[52] J. Yu, X. Chen, Y. Wang, H. Zhou, M. Xue, Y. Xu, Z. Li, C. Ye, P. A. v. Aken, P. D. Lund, H. Wang, *J. Mater. Chem. C* **2016**, 4, 7302.

[53] T. Zhai, H. Liu, H. Li, X. Fang, M. Liao, L. Li, H. Zhou, Y. Koide, Y. Bando, D. Golberg, *Adv. Mater.* **2010**, 22, 2547.

[54] B. Shougaijam, R. Swain, C. Ngangbam, T. R. Lenka, *IEEE Trans. Nanotechnol.* **2016**, *15*, 389.

[55] M. Tyagi, M. Tomar, V. Gupta, *J. Mater. Chem. C.* **2014**, *2*, 2387.

[56] M. Liu, B. Su, V. Y. Kaneti, Z. Chen, Y. Tang, Y. Yuan, Y. Gao, L. Jiang, X. Jiang, A. Yu, *ACS Nano* **2017**, 11, 407-415.

[57] Y. Ke, X. Wen, D. Zhao, R. Che, Q. Xiong, Y. Long, *ACS Nano* **2017**, 11 7542-7551.

[58] H. Kim, Y. Kim, K. S. Kim, H. Y. Jeong, A. R. Jang, S. H. Han, D. H. Yoon, K. S. Suh, H. S. Shin, T. Y. Kim, W. S. Yang, *ACS Nano* **2013**, 7, 5769-5776.

[59] J. Zhou, Y. Gao, Z. Zhang, H. Luo, C. Cao, Z. Chen, L. Dai, X. Liu, *Sci. Rep.* **2013**, 3, 3029.

[60] Y. Gao, C. Cao, L. Dai, H. Luo, M. Kanehira, Y. Ding, Z. L. Wang, *Energy & Envrion. Sci.* **2012**, 5, 8708-8715.

[61] Q. Hao, W. Li, H. Xu, J. Wang, Y. Yin, H. Wang, L. Ma, F. Ma, X. Jiang, O. G. Schmidt, P. K. Chu, *Adv. Mater.* **2018**, 30, 1705421.

[62] M. Nakano, K. Shibuya, N. Ogawa, T. Hatano, M. Kawasaki, Y. Iwasa, Y. Tokura, *Appl. Phys. Lett.* **2013**, 103, 153503.

[63] P. Zhang, W. Zhang, J. Wang, K. Jiang, J. Zhang, W. Li, J. Wu, Z. Hu, J. Chu, *Sci. Rep.* **2017**, 7, 4425.

[64] W. Kang, C. Yan, X. Wang, C. Y. Foo, A. W. Ming Tan, K. J. Zhi Chee, P. S. Lee, *J. Mater. Chem. C* **2014**, 2, 4727-4732.

[65] G. Li, S. Zhang, C. Guo, S. Liu, *Nanoscale* **2016**, 8, 9861-9868.

[66] G. Cai, P. Darmawan, M. Cui, J. Wang, J. Chen, S. Magdassi, P. S. Lee, *Adv. Energy Mater.* **2016**, 6, 1501882.

[67] P. Pattathil, R. Scarfiello, R. Giannuzzi, G. Veramonti, T. Sibillano, A. Qualtieri, C. Giannini, P. D. Cozzoli, M. Manca, *Nanoscale* **2016**, 8, 20056-20065.

[68] H. Gu, C. Guo, S. Zhang, L. Bi, T. Li, T. Sun, S. Liu, *ACS Nano* **2018**, 12, 559-567.

[69] G. Cai, P. Darmawan, M. Cui, J. Chen, X. Wang, A. L.-S. Eh, S. Magdassi, P. S. Lee, *Nanoscale* **2016**, 8, 348-357.

[70] J. Kim, G. K. Ong, Y. Wang, G. LeBlanc, T. E. Williams, T. M. Mattox, B. A. Helms, D. J. Milliron, *Nano Lett*. **2015**, 15, 5574-5579.

[71] G. Garcia, R. Buonsanti, A. Llordes, E. L. Runnerstrom, A. Bergerud, D. J. Milliron, *Adv. Opt. Mater.* **2013**, 1, 215-220.

[72] H. Shin, S. Seo, C. Park, J. Na, M. Han, E. Kim, *Energy & Environ. Sci.* **2016**, 9, 117-122.

[73] H.G. Moon, Y. R. Choi, Y.-S. Shim, K.-I Choi, J.-H. Lee, J.-S. Kim, S.-J. Yoon, H.-H. Park, C.-Y. Kang, H. W. Jang, *ACS Appl. Mater. Interfaces* **2013**, 5, 10591.

[74] J.-C. Lin, V. T. Tra, D.-S. Tsai, T.-T. Lin, P.-C. Huang, W.-L. Hsu, H. J. Wu, R. Huang, N. V. Chien, R. Yoshida, J.-Y. Lin, Y. Ikuhara, Y.-P. Chiu, S. Gwo, D. P. Tsai, J.-H. He, Y.-H. Chu, *Adv*. *Mater*. **2016**, 28, 764.

[75] F.J. G. De Abajo, *Rev. Mod. Phys.* **2010**, 82, 209

[76] Y. Yan, L. Liu, Z. Cai, J. Xu, Z. Xu, D. Zhang, X. Hu, *Sci*. *Rep*. **2016**, 6, 31328.

[77] L. Liu, P. Peng, A. Hu, G. Zou, W. W. Duley, Y. N. Zhou, *Appl*. *Phys*. *Lett*. **2013**, 102, 073107.

Reliable Operation of Hybrid Perovskite-Based Broadband Photodetectors by Inhibition of Defect Migration

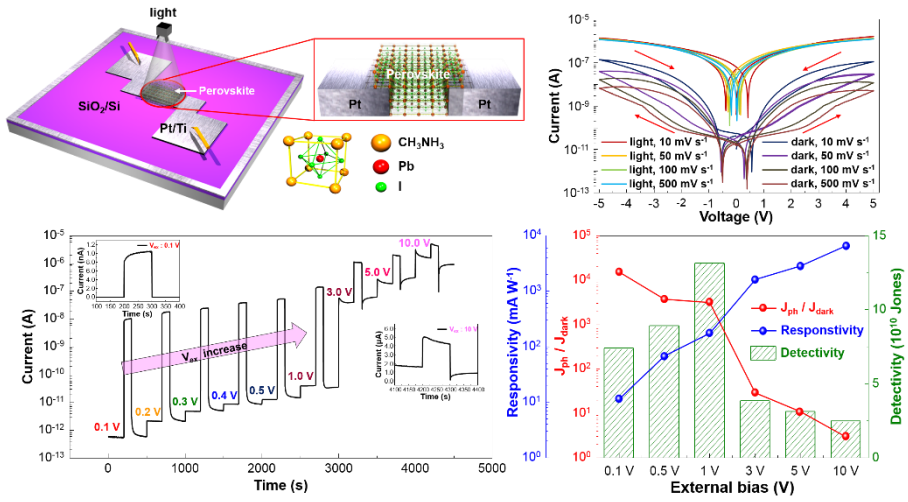

4.1. Introduction

Organometallic halide perovskites (OHPs, such as $CH_3NH_3X_3$, X: Cl, Br, I or mixed halides) are fascinating and emerging optoelectronic materials not only for frequently studied photovoltaic cells[1-5] but also for photodetectors,[6-9] light-emitting diodes,[10] and lasers(Figure 4.1 and Figure 4.2).[11] Optoelectronic devices with OHPs show high performance and efficiency, and thus OHPs lead to future applications due to their notable advantages such as high external quantum efficiency,[12] excellent light absorption coefficient, long charge carrier diffusion length, and long life time (Figure 4.3).[13] Despite rapid progress in OHP-based optoelectronics, the current–voltage (*I–V*) hysteresis behavior of OHPs makes it difficult to obtain reliable device performance, an issue that has not been intensively studied (Figure 4.4). Recently, several theoretical[14-17] and experimental studies[18-21] have proposed that the migration of defect ions is the origin of the hysteretic behavior in OHPs (Figure 4.5). In order to prevent the degradation of performance in OHP-based optoelectronic devices via the migration of defect ions, some have proposed applying interface engineering using buffer layers[22-24] or solvent engineering methods.[25,26] Although the hysteresis in OHP-based optoelectronic devices is somewhat alleviated using these approaches, such methods have drawbacks in terms of cost. In this respect, careful investigation of the migration of unintentionally formed defects in OHP films and of methods for inhibiting defects and ion migration should be carried out.

Here, we report reliable $CH_3NH_3PbI_3$ ($MAPbI_3$) broadband photodetectors with a buffer-layer-free simple metal/semiconductor/metal (MSM) lateral structure and a

high on/off ratio ($I_{on}/I_{off} = 10^4$ under 0.05 sun conditions). The *I–V* characteristics of photodetectors clearly exhibit sweep rate-dependent hysteresis, especially in the dark, due to the migration of defect ions in $MAPbI_3$ films. The migration of defect ions is generated by external bias, and it more severely affects dark current behavior as the external bias increases. Thus, photodetectors show poor on/off ratios and spikes of dark currents and photocurrents at high external bias. We show that the proposed photodetector displays high on/off ratios and reliable operation at low voltages where the migration of defect ions is inhibited. More interestingly, it is revealed that the electrical history of the device such as poling significantly affects device performance and should be controlled for reliable operation.

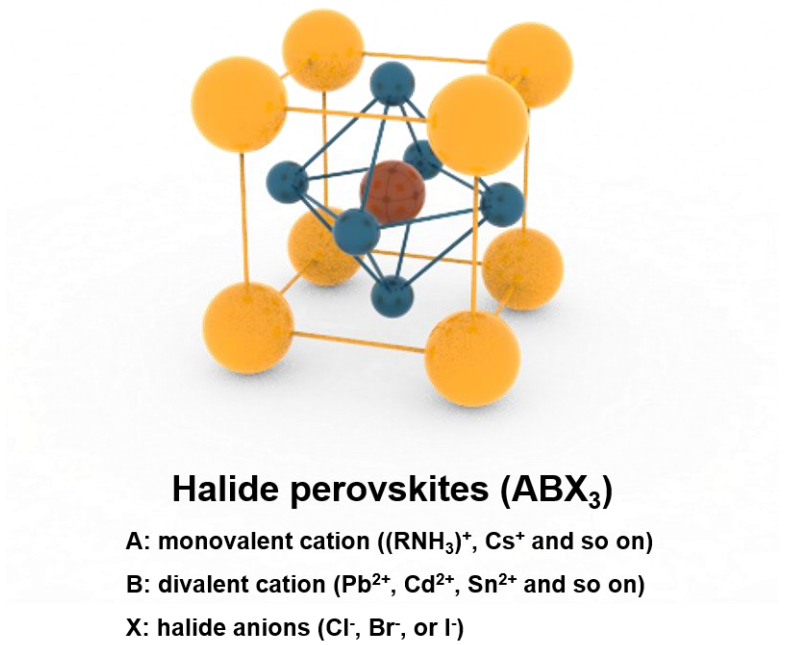

Figure 4.1. Crystal structure of halide perovskite (ABX_3).

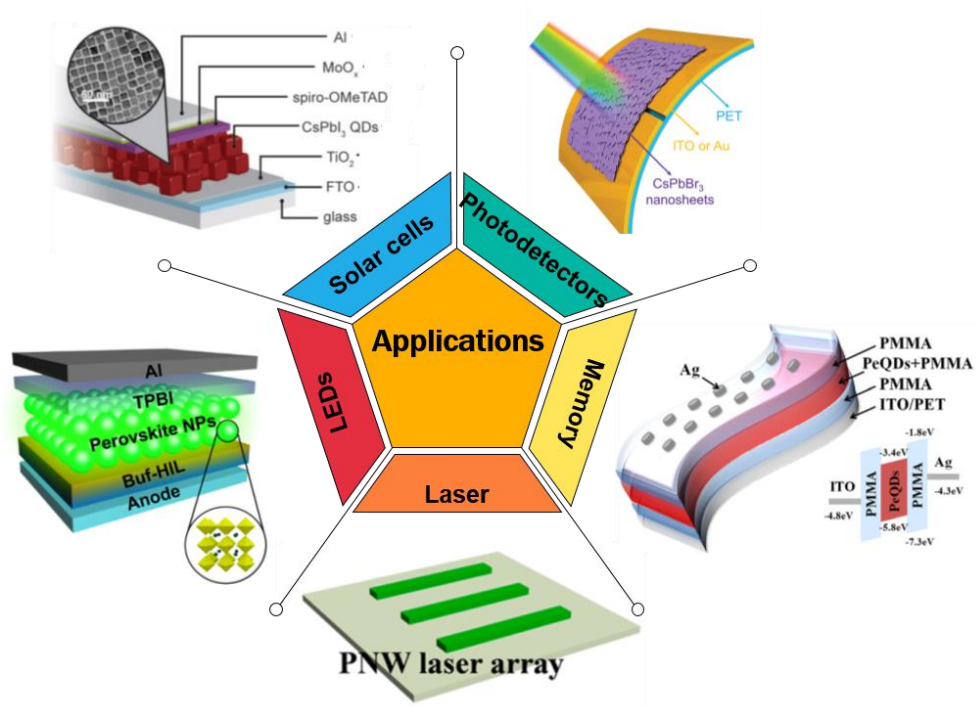

Figure 4.2. Schematic diagram showing the various application of halide perovskites. Figures from Ref. [27-31].

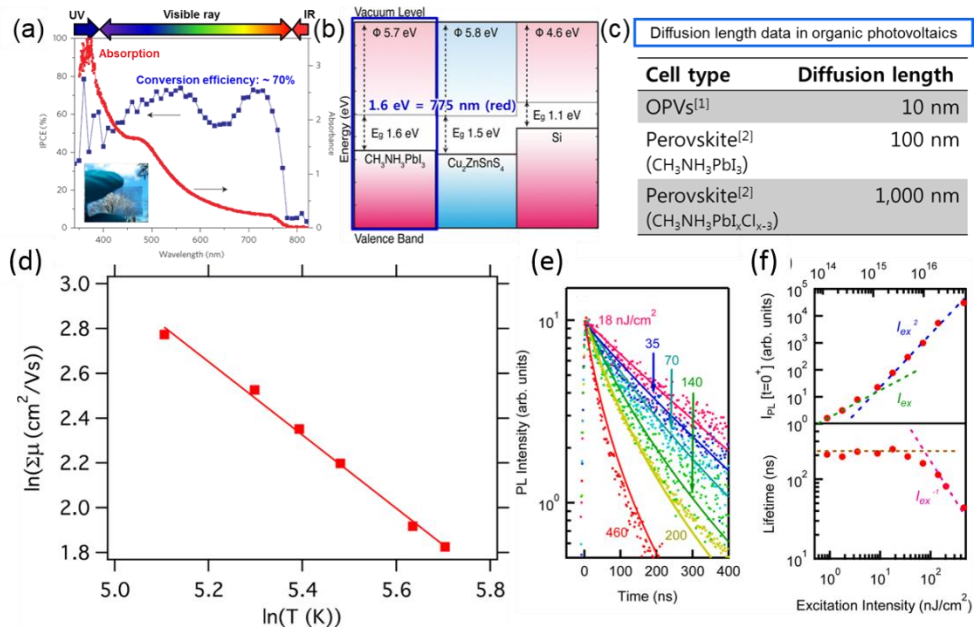

Figure 4.3. Optical properties of halide perovskites: (a) high absorption coefficient and light harvesting characteristics (b) good band alignment with TiO_2 and Au in photovoltaic devices, (c) long carrier diffusion length (d) fast carrier mobility (e, f) slow recombination rate. Figures from Ref. [32-36].

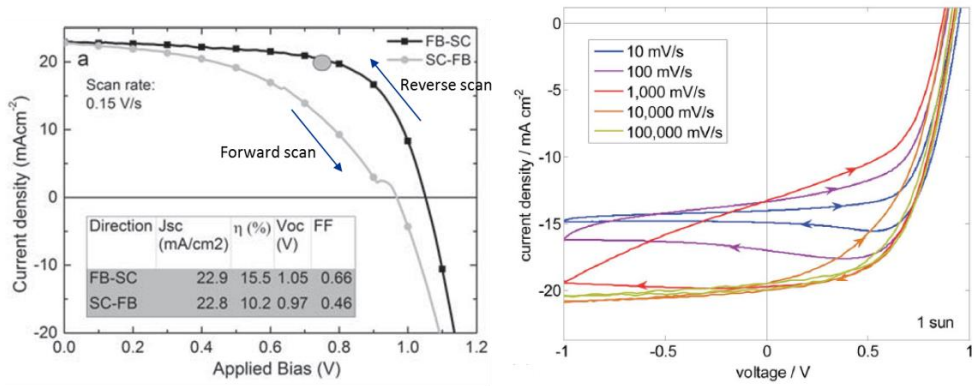

Figure 4.4. Power conversion efficiency deteriorate in solar cell by defect migration. Figures from Ref. [19, 23].

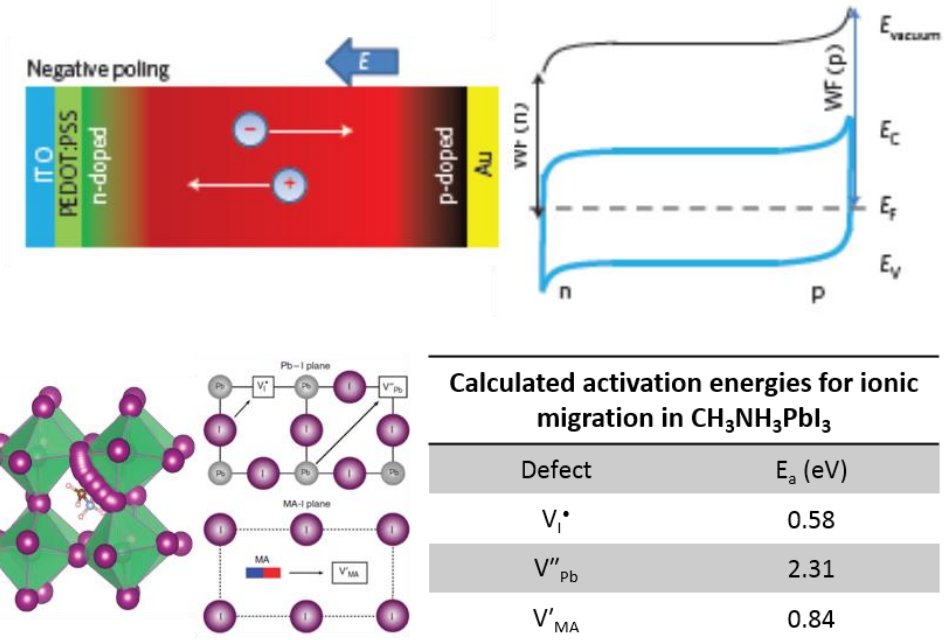

Calculated activation energies for ionic migration in $CH_3NH_3PbI_3$

Defect	E_a (eV)
$V_I^{\bullet}$	0.58
V''_{Pb}	2.31
V'_{MA}	0.84

Figure 4.5. (a) Schematics of ion drift in perovskites during positive and negative poling, respectively, showing that the accumulation of ions in the perovskite near the electrodes induced p- and n-doping. (b), Energy diagram of the p–i–n structure after poling (WF = work function). (c) Calculated migration path indicating a slightly curved path and local relaxation/tilting of the octahedra. (d) Calculated activation energies for ionic defect migration in $CH_3NH_3PbI_3$. Figures from Ref. [15, 18].

4.2. Experimental procedures

4.2.1. Materials preparation

To synthesize the methylammonium iodide (MAI) precursor, methylamine (44 mL, 33 wt% in absolute ethanol, Sigma-Aldrich) and hydroiodic acid (20 mL, 57 wt% in water, Alfa Aesar) were mixed under 0 °C and stirred for 2 h. The yellow-brown precipitate was recovered by rotary evaporation at 80 °C for 1 h to completely evaporate the water. The precipitate was washed with diethyl ether more than three times and dried at 60 °C in a vacuum oven for 24 h. To make the 40 wt% $MAPbI_3$ precursor solution, lead iodide (PbI_2, 99.999% metal basis, Sigma-Aldrich) was mixed with the MAI at a molar ratio of 1:1 in DMF solvent. The mixed precursor solution was stirred for 24 h under 70 °C on a hot plate.

4.2.2. Device fabrication

The Pt interdigitated electrodes (IDEs) were fabricated on SiO_2/Si substrates using photolithography and dry etching. Before spin coating of the perovskite solution, the Pt-IDE/SiO_2/Si substrate was subjected to ultraviolet (UV)–O_3 surface oxidation to make the surface of the substrate hydrophilic in order to obtain a uniform and large-grain $MAPbI_3$ film. The pre-heated precursor solution at 70 °C was used for fabricating the $MAPbI_3$ thin film in order to minimize the formation of large voids. Finally, the $MAPbI_3$ perovskite film was spin coated onto the fabricated Pt-IDEs at a rate of 4000 rpm (67 s^{-1}) for 30 s. The perovskite film was then annealed on a hot

plate at various temperatures (70–130 °C) to complete the crystallization process (Figure 4.6).

4.2.3. Device characterization

The diffraction patterns of the crystallized $MAPbI_3$ films were identified by XRD measurements (New D8-Advance, Cu Kα). Field emission scanning electron microscope (FE-SEM, JEOL, JSM-5410LV, Japan) images of the $MAPbI_3$ films were also obtained. The absorption spectra of the crystallized $MAPbI_3$ films on glass substrate were measured by an ultraviolet-visible photospectrometer (JASCO V-740) with a wavelength range from 250 nm to 850 nm. The steady-state photocurrent curves were measured under simulated AM 0.05G irradiation (5 mW cm^{-2}) using a xenon lamp with various filters (Oriel 66902). A homemade 4-probe station with an Agilent 4156C semiconductor parameter analyzer was used to apply a scanning bias and test the output current simultaneously. All of the electrical tests were performed at a vacuum of 4 mTorr, wherein light (AM 1.5G of 5 mW cm^{-2} and 3 μW cm^{-2}, 532 nm of 65 μW cm^{-2}, and 75 nW cm^{-2}) was incident through a fiber in a vacuum chamber. The poling bias lasted for approximately 300 s at ± 1 V. After poling, the *I–V* curves were measured by using the Agilent 4156C semiconductor parameter analyzer (Figure 4.7). To evaluate the device performance parameters, the on/off ratio, responsivity, and detectivity were calculated by the following equations. The on/off ratio is the ratio of the photocurrent to the dark current. It is expressed by $I_{ph}/I_d = J_{ph}/J_d$, where I_{ph} is the photocurrent, I_d is the dark current, J_{ph} is the photocurrent density, and J_d is the dark current density. Responsivity is the ratio of the photocurrent to the incident light on the effective area. It is given by $R = I_{ph}/AL_{light}$,

where A is the effective area and L_{light} is the incident light intensity. Detectivity can be expressed as $D^* = R/(2qJ_d)^{1/2}$, where R is the responsivity, q is the elementary charge, and J_d is the dark current density.

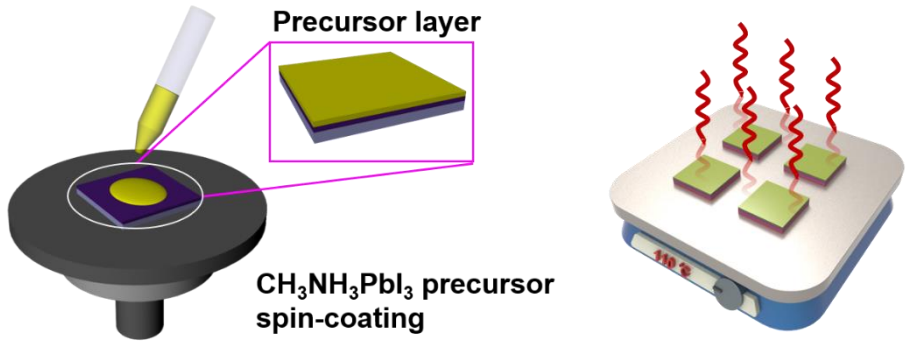

Figure 4.6. Schematic illustration for fabrication process of $CH_3NH_3PbI_3$ ($MAPbI_3$) thin films and $CH_3NH_3PbI_3$ -based photodetector.

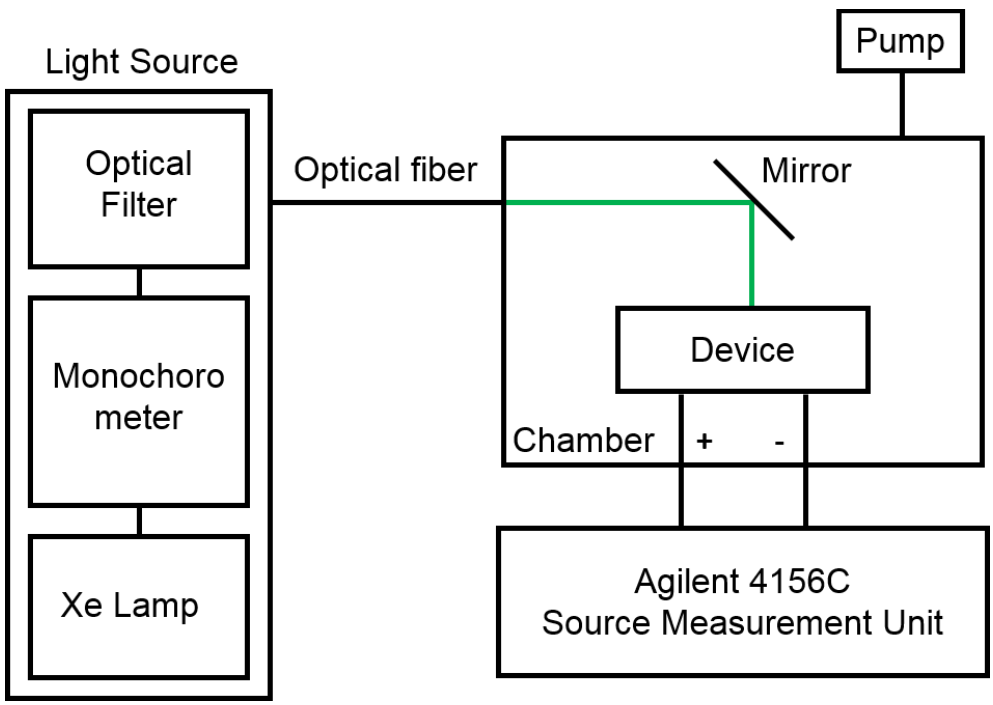

Figure 4.7. Measurement set-up for photoresponse of $CH_3NH_3PbI_3$-based photodetector.

4.3. Results and Discussion

4.3.1. Device fabrication and optimization

The $MAPbI_3$-based photodetectors investigated in this work had an MSM lateral structure, as shown in Figure 4.8. The simple MSM structure without any expensive additional layers or gates so that it can be the remarkable advancement in terms of processability and cost. We selected Pt for the electrodes which do not react with chemical reagent because it is inert noble metal. Compared to ITO based lateral structure, the ITO makes the electron injection at ultraviolet regions.[6] Pt electrode is not absorbed the UV light and even visible light, so it is suitable for electrode material for photodetector application. Methylammonium iodide (MAI) and lead iodide (PbI_2) precursors dissolved in N,N-dimethylformamide (DMF) were spin coated onto Pt interdigitated electrodes (IDEs), which had 20 fingers and the same interspacing distance of 5 μm (see the Experimental Section).[37-38] The spin-coated solution was crystallized by annealing at 70−130 °C. The crystallized $MAPbI_3$ films were polycrystalline, with grains consisting of a tetragonal $MAPbI_3$ phase as determined by X-ray diffraction (XRD) measurements (Figure 4.9).[39] The thickness of the crystallized $MAPbI_3$ films was approximately 450 nm (Figure 4.10). In order to clarify the surface morphology of prepared $MAPbI_3$ films with various annealing temperatures, the atomic force microscopy (AFM) measurement was performed. The root-mean square (RMS) roughness of the $MAPbI_3$ films annealed at 70, 90, 110, and 130 °C were 103.87, 99, 76.71, and 118 nm, respectively (Figure 4.11). Although the crystal structure and thickness of the prepared $MAPbI_3$ films at various annealing temperatures were similar to each other, the 110 °C-annealed $MAPbI_3$ films showed

slightly higher absorbance than other temperature annealed samples at 400–900 nm (Figure 4.12). Based on these experimental measurements, the 110 °C-annealed $MAPbI_3$ film has the larger size grain and smaller voids in the film than other temperature annealed ones. From this, we concluded that 110 °C was the optimum annealing temperature for the $MAPbI_3$ film.

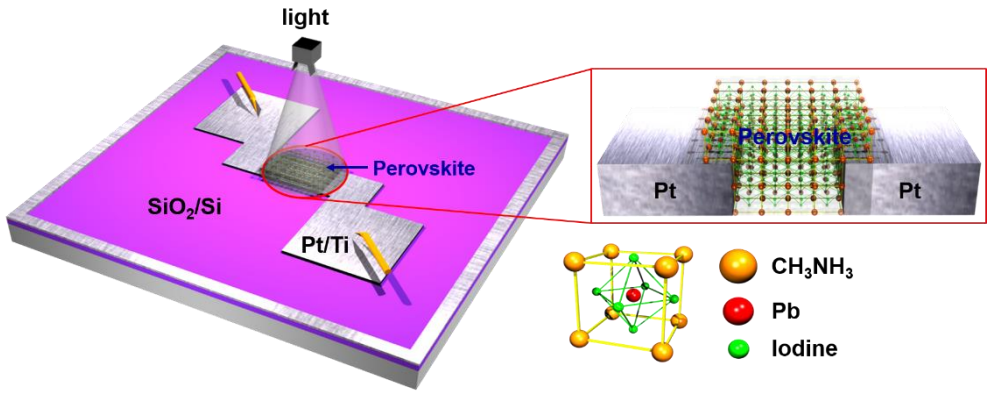

Figure 4.8. Schematic diagram of $MAPbI_3$-based perovskite photodetector and crystal structure of $MAPbI_3$ perovskite.

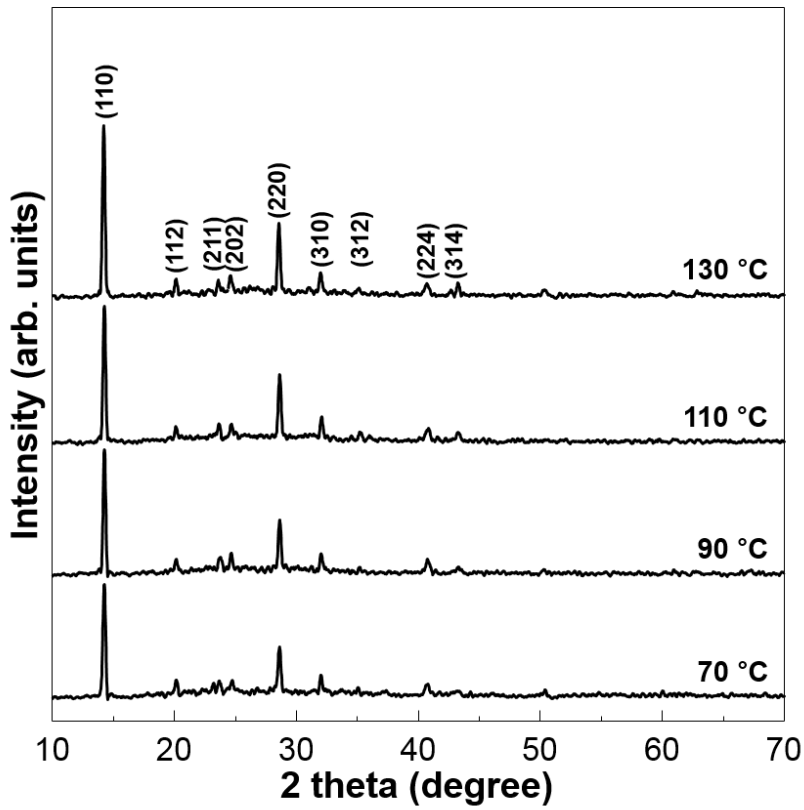

Figure 4.9. XRD data from crystallized $MAPbI_3$ films annealed at various temperatures. The shapes and peak positions did not change significantly with crystallization, regardless of annealing temperature.

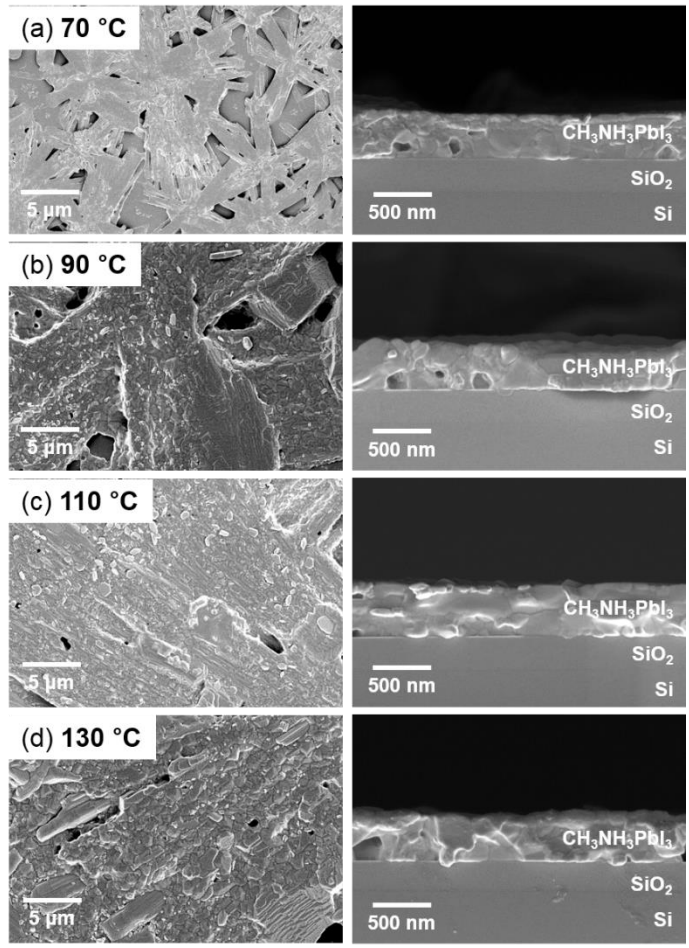

Figure 4.10. SEM images of crystallized $MAPbI_3$ film on SiO_2/Si wafer. The crystallization of the $MAPbI_3$ film was performed at annealing temperatures of (a) 70, (b) 90, (c) 110, and (d) 130 °C.

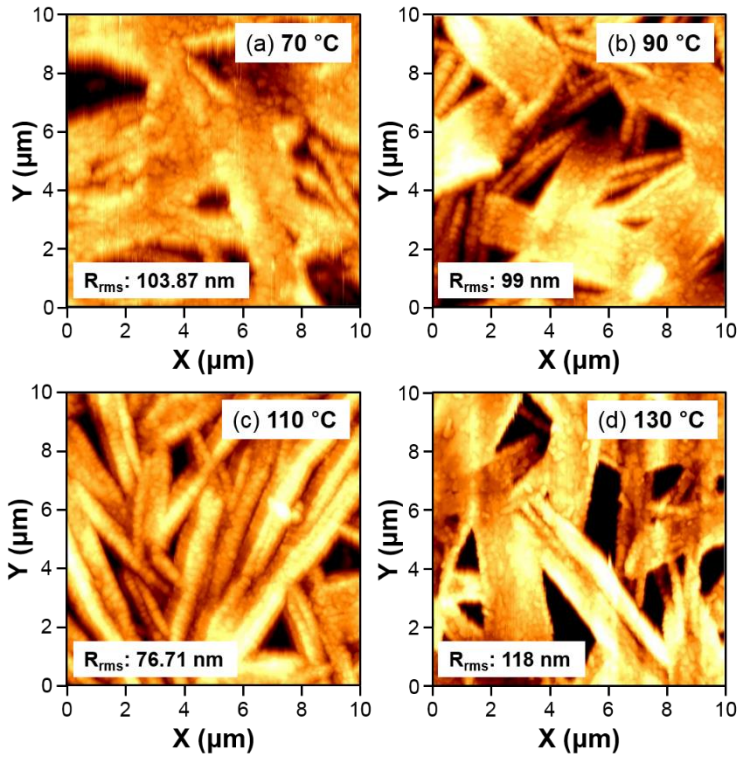

Figure 4.11. The AFM measurements of prepared $MAPbI_3$ with various annealing temperatures. The root-mean square (RMS) roughness of the $MAPbI_3$ films annealed at (a) 70 °C (R_{rms} =103.87 nm) (b) 90 °C (R_{rms} =99 nm), (c) 110 °C (R_{rms} =76.71 nm), and (d) 130 °C (R_{rms} =118 nm), respectively.

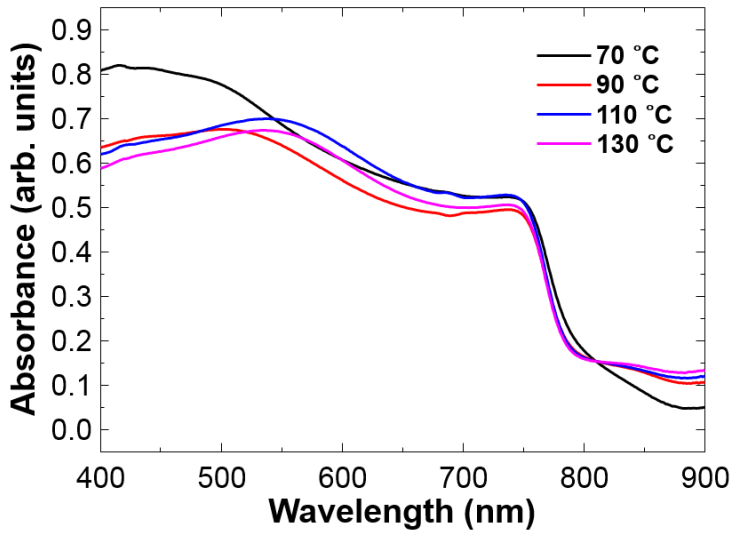

Figure 4.12. Absorption spectra of $MAPbI_3$ film annealed at various temperatures. The absorption edge and the intensity of absorbance spectra are almost same for the all samples.

4.3.2. Figure of merits of Pt/$CH_3NH_3PbI_3$/Pt photodetector

There are several significant figure-of-merit parameters for evaluating the optical properties of photodetectors, such as on/off ratio, responsivity (R), and detectivity (D^*) (see Experimental Section), although the primary parameter to be considered may be different depending on the application. We evaluated the parameters of the fabricated photodetector with various external voltage (V_{ex}) values, as shown in Figure 4.13. As V_{ex} increases, the on/off ratio decreases, whereas the responsivity increases. For the on/off ratio, the dark current is the limiting factor as it rapidly degrades with increasing V_{ex}. Our photodetector operated at low external bias showed a remarkable on/off ratio as compared to a simple MSM-structured photodetector,[40-42] and a previously reported solution-processed photodetector.[6, 43-46] This high on/off ratio is also more remarkable than that of a previously reported lateral-structured $MAPbI_3$-based photodetector operated at high external bias. [6, 43-46] For evaluating the responsivity, only photocurrents were considered. Thus, the highest responsivity was achieved at 10 V. The calculated responsivity of our device is similar to that of previously reported lateral-structured $MAPbI_3$-based photodetectors[6, 43-46] and lower than that of vertical-structured $MAPbI_3$-based photodetectors owing to larger electrode spacing.[6,43, 45] For the detectivity, it can be expressed as $D^* = R\,(2qJ_d)^{-1/2}$, where R is the responsivity, q is the elementary charge, and J_d is the dark current density when the dark current is dominated by the shot noise.[9] In order to investigate which noise is dominant in dark current for our fabricated device, the noise (dark) current was measured by using the Axopatch 200B measurement system, as shown in Figure 4.14. Because the noise current shows the frequency-independent behavior in the dark, we could conclude that the

shot noise is dominant in our fabricated devices. Because the dark currents and photocurrents should both be considered to determine the detectivity, the photodetector showed the highest detectivity (1.3×10^{11} Jones) at 1 V. The response time (t_r) and recovery time (t_d) are also significant figure-of-merit for a photodetector. To identify the t_r and t_d for our device, the transient photocurrent was measured under the illumination with white light of 5 mW/cm^2, as shown in Figure 4.15a. Although the exact t_r and t_d could not be measured because of the measurement limitation of our equipment, it is clear that the t_r is shorter than 90 ms and the t_d is shorter than 20 ms. In order to compare the photo-response performance of our device with that of previously reported lateral structured devices, the responsivity, detectivity, and response time were summarized in Table 4.1.. The responsivity and detectivity of our device measured at 1 V are higher than those of other lateral-structure photodetectors.[6,43-46] Moreover, our device shows the faster t_d and t_r values than previously reported ones.[44-46] The stability of hybrid perovskite is important issue in practical applications. In the previous reports, the stability of the hybrid perovskite-based devices could be enhanced with appropriate passivation layers such as CYTOP and PMMA.[7,8,45,46] In order to evaluate the stability of our fabricated $MAPbI_3$-based photodetector, the stability test was performed in rough vacuum condition (50 mTorr) over 14 days. The photocurrent of fabricated device was maintained the initial value without perceptible changes over the period as shown in Figure 4.15b. Broad spectral detection is beneficial for extending the application range of photodetectors to include imaging and monitoring devices, chemical sensors, and biosensors. To determine the detectable wavelength of our photodetector, the photoresponse to wavelength was measured from 300 nm to 1000 nm at V_{ex} of 1 V.

The wavelength-dependent photocurrent and the responsivity are plotted in Figure 4.15c. Our device displayed photoresponses to a wide range of spectra, and the photocurrent and photoresponse of our photodetector showed good agreement with the absorption spectrum. Moreover, the rejection ratio of visible-to-infrared was approximately 10^2 to 10^3. Based on these results, it is apparent that the $MAPbI_3$-based photodetector operating at low V_{ex} shows remarkable performance and can detect a wide range of light wavelengths.

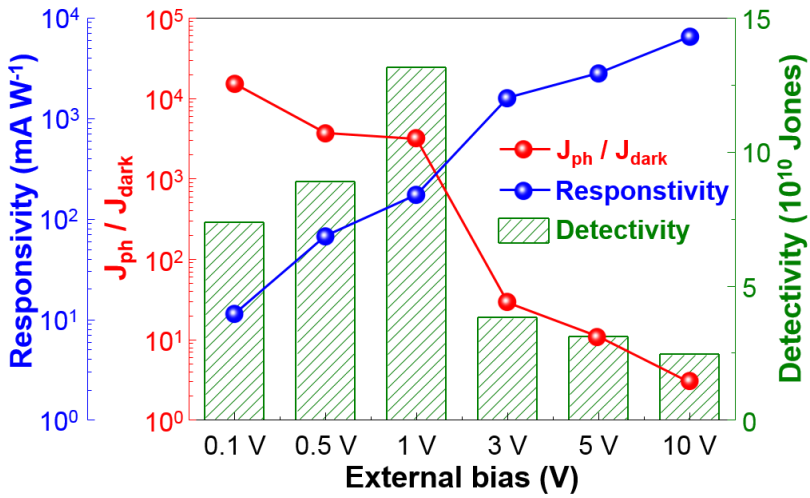

Figure 4.13. Device performance plotted against external bias. The highest on/off ratio was obtained at 0.1 V (lowest dark current and highest photocurrent). The highest detectivity was obtained at 1 V (relatively low dark current and high photocurrent).

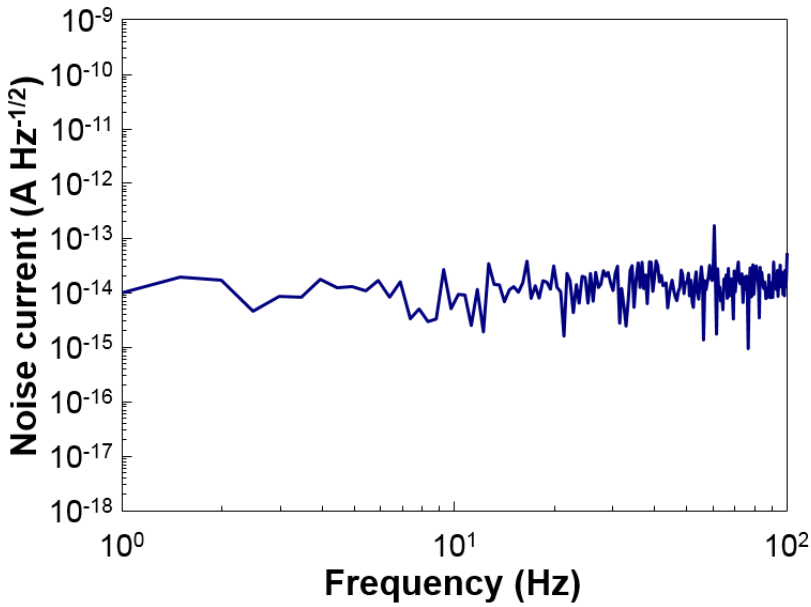

Figure 4.14. The noise current analysis of the fabricated perovskite-based photodetector. The noise current shows the frequency-independent behavior in the dark, indicating that the shot noise was dominant in our fabricated devices.

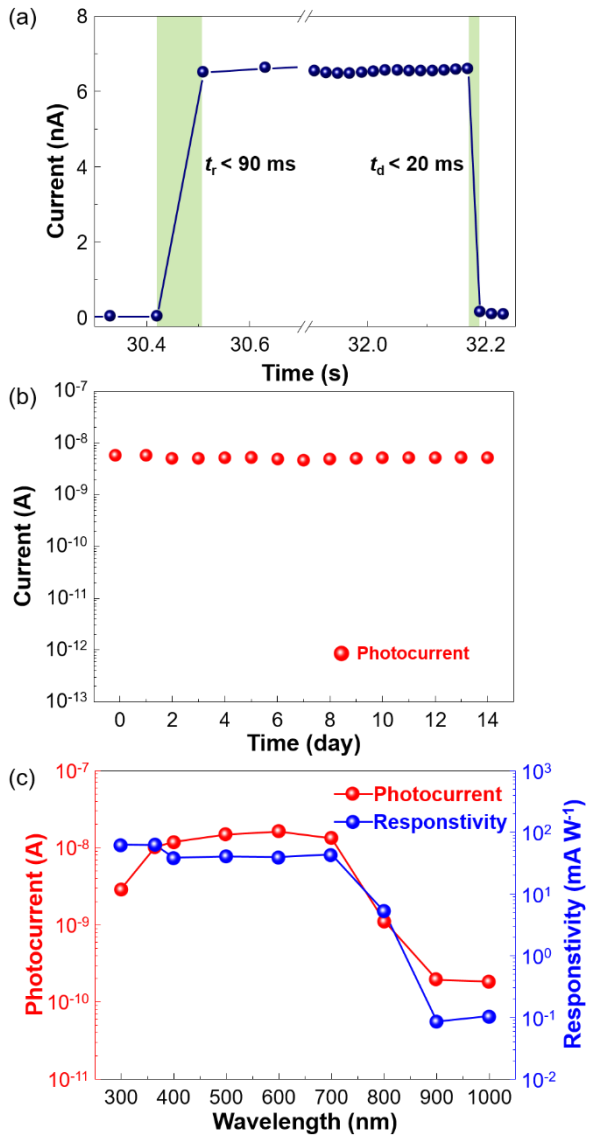

Figure 4.15. (a) The response and recovery time analysis of the fabricated perovskite-based photodetectors. The response time and recovery time is shorter than 90 and 20 ms, respectively. (b) The stability test in rough vacuum condition over 14 days. (c) Photocurrent and responsivity properties with respect to wavelength.

Table 4.1. Comparison of the device performances, including responsivity and detectivity, between our lateral MSM structure and previously reported lateral structured devices. The performances of our device are comparable to previously reported lateral structured ones.

Device structure	Device type	Responsivity	Detectivity	Response time	Recovery time
Au/graphene/Au on $MAPbI_3$ (Lateral)	Phototransistor	0.3 A W^{-1} (V_D = 0.1 V, V_G = 0 V) (1 mW cm^{-2})	5 × 10^7 Jones	87 ms	540 ms
Au/$MAPbI_{3-x}Cl_x$/Au on PMMA (Lateral)	Phototransistor	0.9 A W-1 (V_D = 30 V, V_G= 0 V) (10 mW cm^{-2})	N/A	6.5 μs	5 μs
Au/$MAPbI_{3-x}Cl_x$/Au on CYTOP (Lateral)	Photodiode	0.5 A W^{-1} (V = 2 V) (200 μW cm^{-2})	N/A	N/A	N/A
ITO/$MAPbI_3$/ITO (Lateral)	Photodiode	0.2~0.5 A W^{-1} (450 ~ 800 nm) (V = 3 V) 0.01 mW cm^{-2})	N/A	t < 0.2 s	t < 0.2 s
Pt/$MAPbI_3$/Pt (This work)	Photodiode	0.01 A W^{-1} (V = 0.1 V, 5mW cm^{-2}) 0.18 A W^{-1} (V = 1 V, 5mW cm^{-2})	5.42643× 10^{10} Jones (V = 0.1 V) 9.67041× 10^{10} Jones (V = 1 V)	t < 90 ms	t < 20 ms

4.3.3. *I-V* hysteresis

As seen in previous reports,[16-24] OHP-based devices can show hysteretic behavior which frustrates to obtain reliable performance. The hysteretic behavior is attributed to the migration of point defects such as negatively charged Pb (V_{Pb}'') and methylammonium vacancies (V_{MA}') and positively charged I vacancies ($V_I^{\bullet}$) that can exist in solution-processed $MAPbI_3$ films due to their low formation energies.[14,15]. The hysteric behavior of our device has been estimated by measuring the photo and dark *I-V* characteristics with changing the scan rate, as shown in Figure 4.16a. In the various scan rates, the voltage was swept in the sequence 0 V → +5 V → 0 V → −5 V → 0 V, and the measured current values were plotted on a logarithmic scale. The device showed butterfly-shaped hysteresis loops in the dark and under illumination (white light of 5 mW cm^{-2}), and hysteresis was more pronounced in the dark. As the voltage sweep rate increased, the hysteresis became more severe and the saturation current decreased. Since charged defect ions such as V_{Pb}'', V_{MA}', and $V_I^{\bullet}$ can migrate under external bias, $MAPbI_3$ is called a mixed ionic–electronic conductor.[15] Due to the migration of defect ions by external electric fields, $MAPbI_3$ exhibited hysteresis in its *I–V* characteristics, as reported in previous studies.[18,47] In the dark, *I–V* curves with slower sweep rates showed larger open circuit voltages (the difference of voltage between two current minimum points) and less pronounced hysteresis. Charged defect ions are less mobile than electronic carriers such as electrons and holes. Thus, the migration of charged defect ions is more favorable at slower sweep rates than at faster sweep rates. Therefore, hysteresis is more severe and the saturation current is lower with faster sweep rates. Under illumination, the hysteresis seems to be relatively low because the current resulting from photogenerated carriers

is higher than that from ionic carriers. The energy-band diagram of the fabricated device is illustrated in Figure 4.17a. Owing to the large difference between the work function of the Pt electrode (5.3 eV) and the electron affinity of the $MAPbI_3$ film (3.9 eV),[39] the fabricated device showed back-to-back Schottky (rectifying) *I–V* characteristics in the dark (Figure 4.16b). Ideally, the fabricated device should have equal Schottky barriers for the contacts between the Pt/$MAPbI_3$ and $MAPbI_3$/Pt interfaces, as shown in Figure 4.17a, leading to symmetric *I–V* characteristics. However, the charged defect ions migrated to the metal/$MAPbI_3$ interfaces by external bias during the *I–V* measurements, as illustrated in Figure 4.17b. The ion migration resulted in unequal Schottky barriers for the contacts between the Pt/$MAPbI_3$ and $MAPbI_3$/Pt interfaces, and the resulting *I–V* characteristics were asymmetric. Because of the unequal Schottky barriers, the voltage for the minimum current was not 0 V. We emphasize that hysteric *I–V* characteristics with a non-zero built-in potential (V_{bi}) are typical phenomena observed in mixed ionic–electronic conductors.[48] It is clear that the interfacial region dominant with negatively charged defect ions becomes *p*-type and the region with positively charged defect ions becomes *n*-type. Hence, *p*-i-*n* or *n*-i-*p* homojunctions would be formed in the MSM lateral structure, as demonstrated in the previous report.[48] In these *p*-i-*n* homojunctions by self-doping, the generated V_{bi} can screen the external bias and hinder the transport of photogenerated electron and holes.

Since the migration of charged defect ions is a thermally activated process, the hysteric behavior can be affected by temperature. We measured the *I-V* characteristics of the device in the dark and under the illumination (white light, 5 $mWcm^{-2}$) at various temperature with the scan rate of 100 mV s^{-1}, as shown in Figure

4.18. The dark *I-V* still shows hysteric behavior even at the low temperature, meaning that the migration of defects ions occurred. However, it is apparent that the current level in the dark at 123 K is much lower than that at 298 K (Figure 4.18c). Since $MAPbI_3$ is a semiconductor, the concentration of electronic carriers should be lower at 123 K than 298 K. Also, the migration of charged defect ions becomes less favorable at the low temperature. Thus, the dark current was quite low even though there was hysteresis in the *I-V* curve. In contrast, the photo *I-V* curve at 123 K does not show hysteretic behavior, which indicates that the transport of photogenerated carriers is more predominant than the migration of charged defect ions.

We have measured the *I-V* characteristics at various temperatures to see how temperature has an effect on charge transport in the $MAPbI_3$ film. The saturation current in the dark significantly increased as a function of temperature. For the forward scan (0 V → 5 V), the *I-V* curves could be divided into two regions. In the region where the dark current was quite flat without change, the electronic transport was dominant. After the dark current increased steeply, the ionic transport (migration of charged defect ions) became predominant. The flat region was reduced as temperature was increased because the number of charged defect ions could be thermally activated for migration even at low voltage biases (Figure 4.18 c-h). For the photo *I-V* curves, hysteretic behavior was not observed below 150 K due to the reduced number of thermally activated charged defect ions (Figure 4.18c-d). As the temperature increased, the number of thermally activated charged defect ions was increased so that hysteretic behavior was observed above 150 K (Figure 4.18e-h). In order to summarize the hysteretic behavior of our device with various temperatures, the ln (*J*) values are plotted against $1000/T$ in the dark and under the illumination at

1 V with different scan directions as shown in Figure 4.19. The current density values from forward scan (0 V → 5 V) are lower than that from reverse scan (5 V → 0 V). It is due to V_{bi} which is generated by high external bias (3 V – 5 V) of the forward scan. In the reverse scan, the polarity in the film generated by the V_{bi} can enhance charge transport through the Pt electrodes. It is clearly shown that the forward scanned and reverse scanned current densities in the dark decrease as temperature decrease.

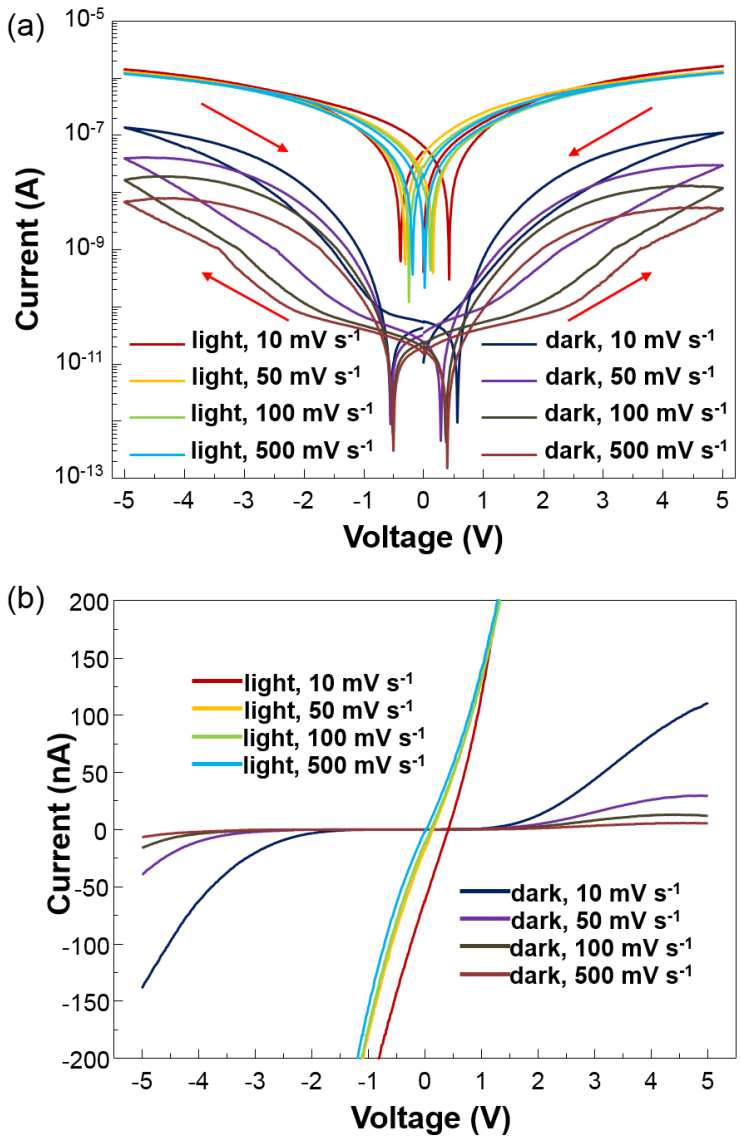

Figure 4.16. Dark and photocurrent hysteresis curves in (a) log scale and (b) linear scale with various sweep voltage rates.

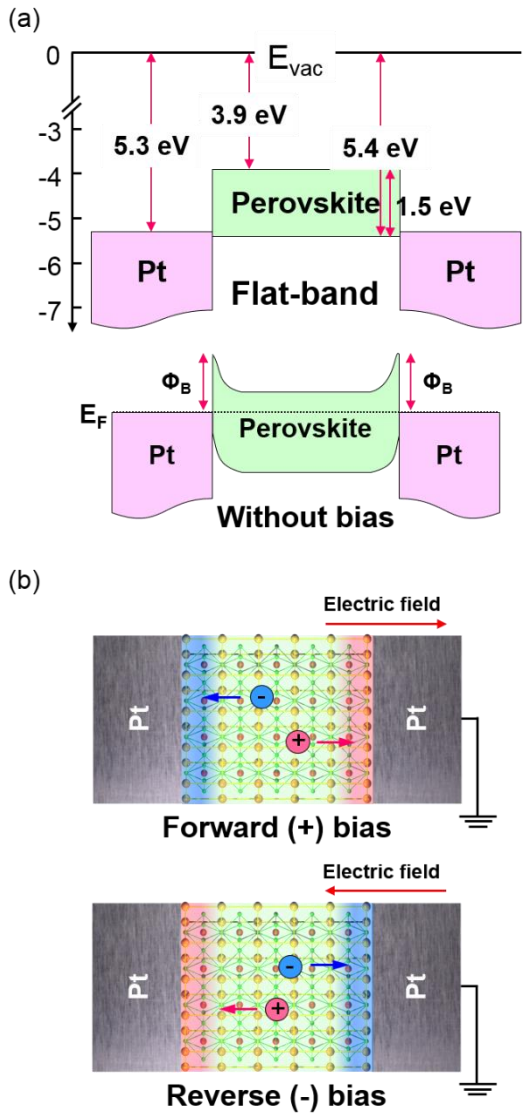

Figure 4.17. (a) The flat-band diagram and equilibrium state of the Pt/$MAPbI_3$/Pt device without external bias. (b) Schematic diagram of ion drift in the $MAPbI_3$ film with forward and reverse bias. The negatively charged defect ions make a p-type self-doping region and the positively charged defect ions make an n -type self-doping region under the external electric field, result in p-i-n or n-i-p homojunctions.

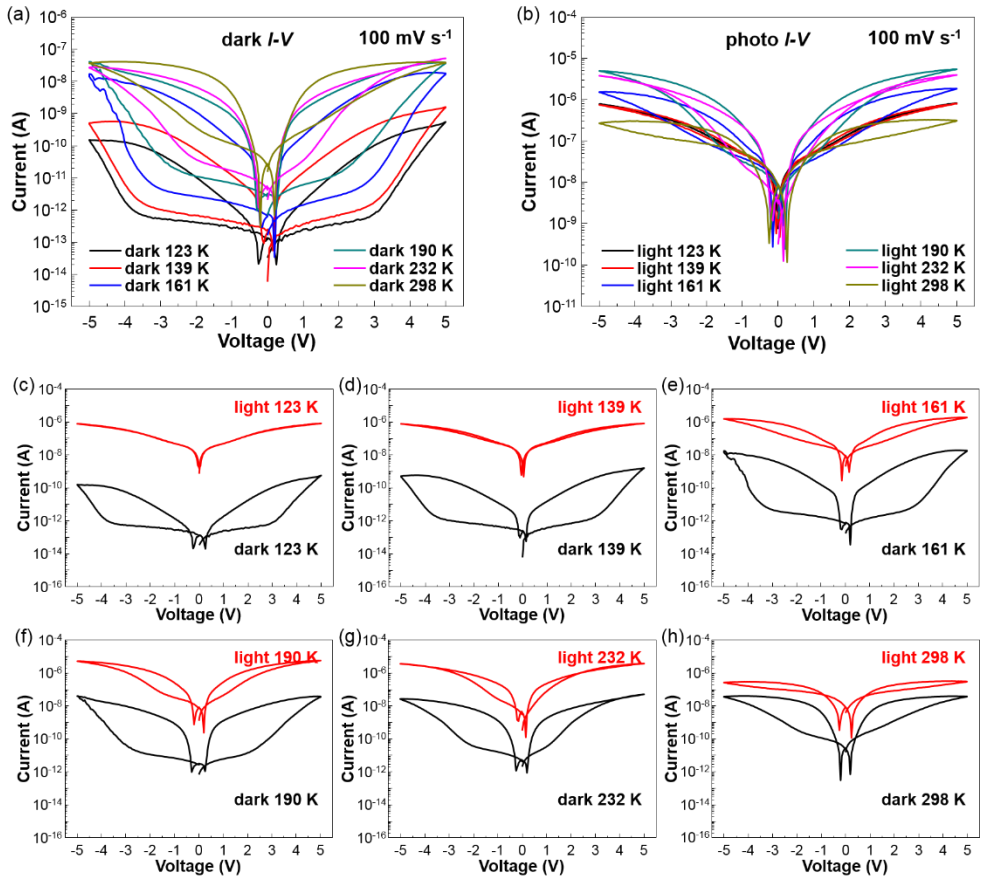

Figure 4.18. (a) Dark and (b) photo *I-V* curves with different temperatures at a scan rate of 100 mV s^{-1}. The dark *I-V* clearly shows the temperature-dependent hysteretic behavior by electronic transport. The dark and photo *I-V* curves under (c) 123 K, (d) 139 K, (e) 161 K, (f) 190 K, (g) 232 K, and (h) 298 K.

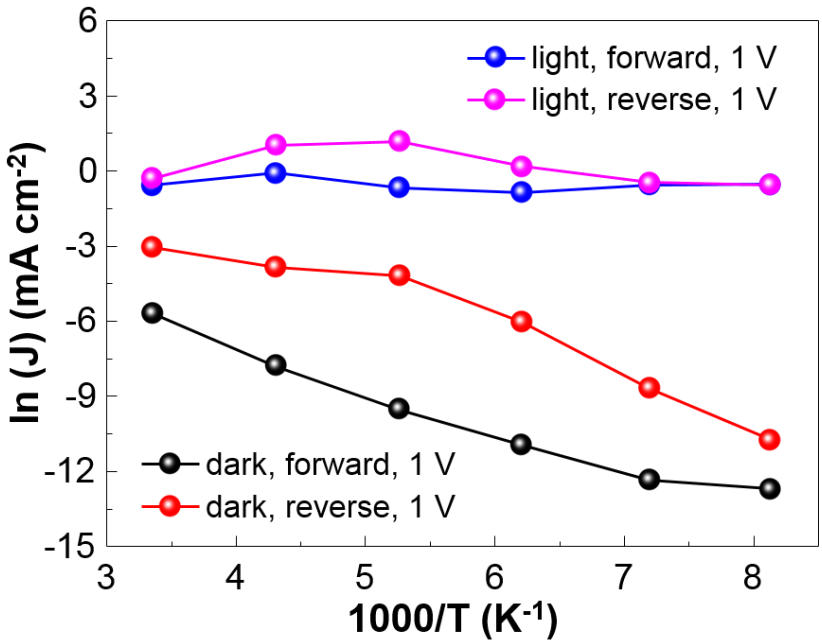

Figure 4.19. The log (current density) plotted against 1000T to summarize the hysteric behavior of Figure 4.18. The higher current density values in reverse scan (5 → 0 V) originate from the formation of built-in potential. The hysteric behavior of photocurrent is negligible because the transport of photogenerated carrier is more dominant than electrical transport.

4.3.4. Transient photoresponse characteristics

In general, the migration of charged ions in a solid is strongly influenced by external bias. In order to determine whether the migration of charged defect ions had an impact on device performance, the photoresponse transient of the device under illumination (white light 5 mW cm^{-2}) with varying the external biases (V_{ex}) from 0.1 V to 10 V was obtained and the results are shown in Figure 4.20a. The on/off current ratios were 10^3–10^4 for $V_{ex} < 3$ V, whereas those for $V_{ex} \geq 3$ V were 3–30 due to a significant increase in the dark current. The drastic change in the dark current with external bias can be explained as follows. Because the $MAPbI_3$ film is a mixed ionic–electronic conductor,[14,15,18] the total dark current (I_t) can be expressed as

$$I_t = I_e + I_i \quad (1)$$

where I_e is the current originating from electron transport and I_{ion} is that from ionic transport. With low external biases from 0.1 V to 0.4 V (Regions I–II, Figures 4.20b–e), the dark currents are on the order of picoamperes and show small variation with time. In these regions, I_t is almost equal to I_e, because the external bias is too small to drift the defect ions ($I_i \approx 0$). Thus, high on/off ratios could be achieved as a result of low dark currents. When V_{ex} is larger than 0.4 V, the dark currents show spikes at the beginning (Regions II–III, Figures 4.20f–j). This behavior could be explained by the migration of defects ions (V_{Pb}'', V_{MA}', and $V_I^{\bullet}$).[15,18] At first, the dark currents increased rapidly due to the migration of defect ions after applying V_{ex}, and s peaks appeared. The charged defect ions accumulated near the Pt electrodes, forming V_{bi}, which screened the external bias and reduced the ionic and electronic currents. As V_{bi} approached the maximum values, the total currents reached saturated values. It is

estimated that $I_e \approx I_i$ for V_{ex} between 0.5 V and 1 V and $I_i \gg I_e$ for $V_{ex} > 1$ V. Because of the predominant ion migration with $V_{ex} > 1$ V, the spikes are sharper for high V_{ex} values. For $V_{ex} \geq 3$ V, severe ion migration affects the photocurrents,[23] leading to the occurrence of spikes in the photocurrents under illumination. After turning off the light at $V_{ex} \geq 3$ V, the downward spikes in the dark currents are related to light-induced poling, which originates from a photovoltage-induced electric field.[49] Under illumination, the photodetector is subjected to additional bias originating from photogenerated carriers, which break the equilibrium state of the photodetector established in the dark. The additional bias further drives the migration of the charged defect ions to the electrodes. After turning off the light, the additional bias is removed and a back-diffusion current is generated. The back-diffusion current becomes strong as V_{ex} increases. These downward spikes appeared repeatedly in multicycle transient curves (Figure 4.21). Therefore, to obtain reliable performance from $MAPbI_3$-based photodetectors, the ionic current originating from defect migration should be inhibited, and thus $MAPbI_3$-based photodetectors should be operated at low V_{ex}.

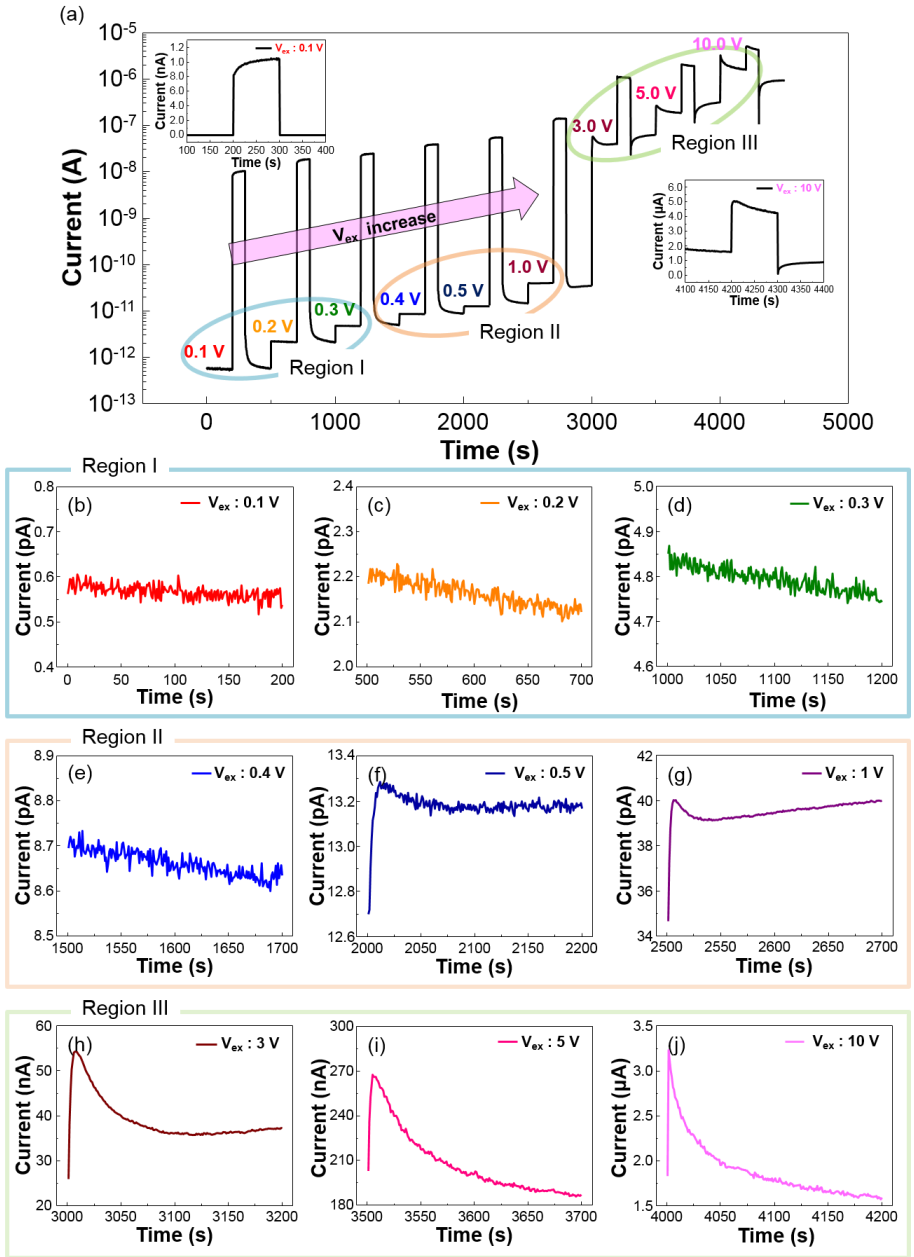

Figure 4.20. *I–t* characteristics of fabricated perovskite photodetector with various external biases. (a) Transient photocurrent plotted against time with various external biases. The dark current behavior at the beginning of each measurement with V_{ex} of (b) 0.1, (c) 0.2, (d) 0.3, (e) 0.4, (f) 0.5, (g) 1, (h) 3, (i) 5, and (j) 10 V. Significant spikes were revealed at 0.5–10 V.

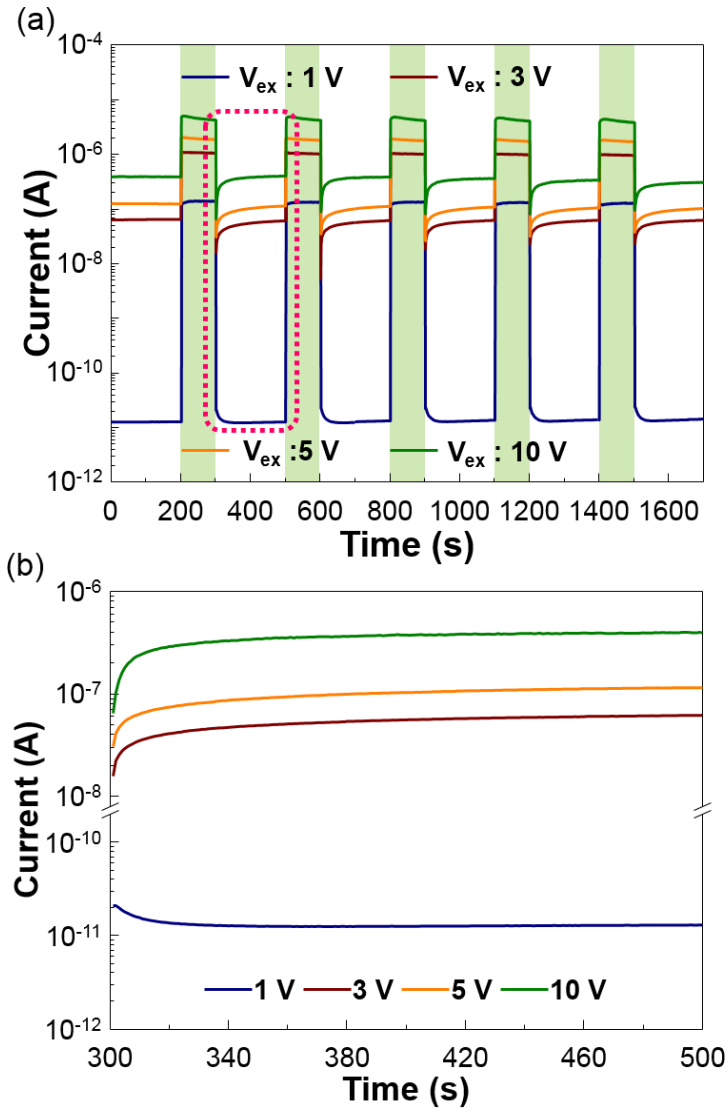

Figure 4.21. (a) Multiple *I–t* characteristics of fabricated device in the dark and under illumination at various external biases. (b) Current behavior in the dark plotted against time is magnified data from (a).

4.3.5. Poling effect

One can speculate that the electrical history could influence the performance of the $MAPbI_3$-based photodetector due to the fact that $MAPbI_3$ is a mixed ionic–electronic conductor. When the device was subjected to an external bias over 0.5 V, as seen in Figure 5, the charged defect ions could migrate in the $MAPbI_3$ film, leading to the formation of V_{bi} in the film. To investigate how the electrical history affects the performance of the photodetector, the photoresponse of pristine and poled devices was measured at V_{ex} of ± 0.1 V during repetitive switching of light illumination of 5 mW cm^{-2}, as shown in Figures 4.22a-b, respectively. At V_{ex} of ± 0.1 V, the pristine device showed a high on/off ratio of approximately 10^4, whereas the poled device showed the lowest dark current, which resulted from the counterbalance between V_{bi} and V_{ex}. As expected, the lateral-structured photodetector showed identical performance regardless of the sign of V_{ex}. For the poled sample, the transient photocurrent was measured after poling at ± 1 V for 300 s, which generated ionic current behavior in the $MAPbI_3$ film even though the film showed the highest detectivity. The poled sample showed an enhanced on/off ratio (10^6) mainly due to the extremely low dark current on the order of femtoamperes, although the photocurrent was reduced somewhat. This can be explained by the fact that V_{bi}, which is generated by poling, screens V_{ex}, resulting in a reduction of the charge collection efficiency.[23]

In general, photodetector devices with higher on/off ratios can detect weaker light than photodetectors with lower on/off ratios. In order to compare the weak light-sensing ability of the pristine photodetector and the poled photodetector, we

measured the illumination-dependent photoresponse transients of the devices and the results are plotted in Figure 4.23. The photocurrent of the pristine device is higher than that of the poled device. Under high-intensity illumination, both devices show stable and reliable photocurrents. However, the poled device shows turbulent and noisy photocurrents under low-intensity illumination. This result clearly shows that electrical history affects the performance of the $MAPbI_3$ photodetector and that poling at high external bias should be avoided in order to obtain high signal-to-noise ratios from $MAPbI_3$ photodetectors, especially for detecting low-intensity light.

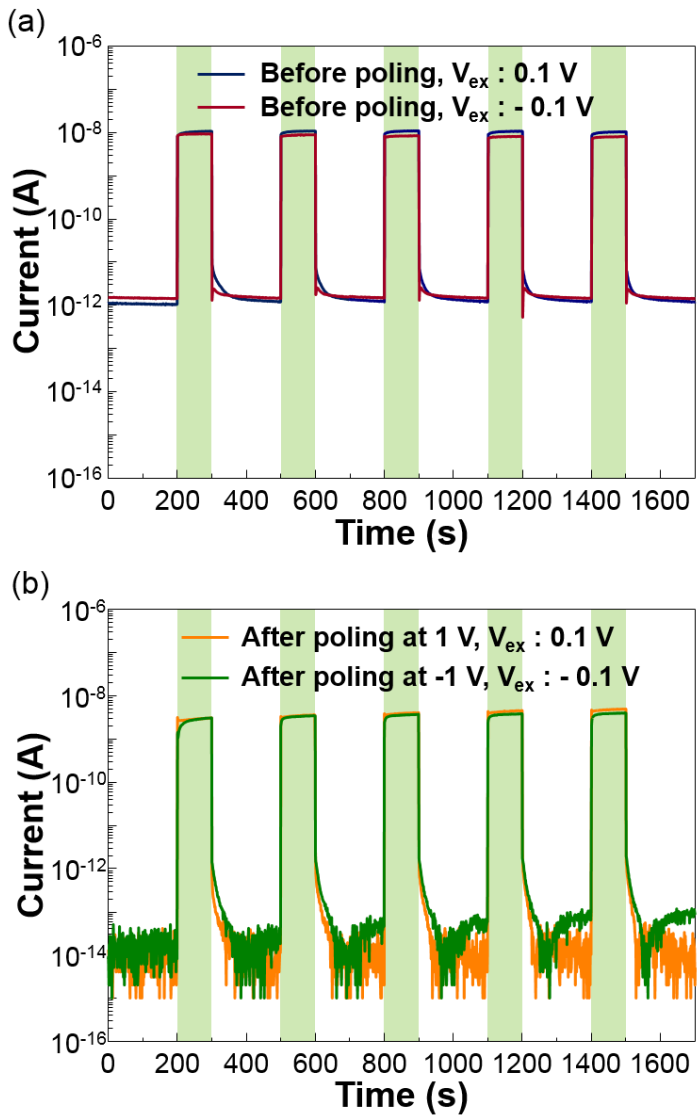

Figure 4.22. Device characteristics both before and after poling. *I–t* curves (a) before poling with external biases of −0.1 and 0.1 V and (b) after poling (−1 and 1 V poling) with external biases of −0.1 and 0.1 V.

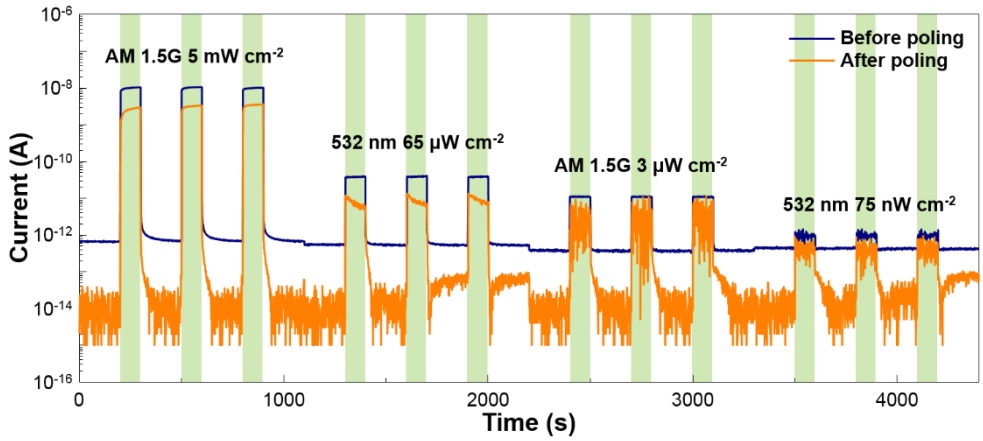

Figure 4.23. *I–t* characteristics both before and after poling at various incident light intensities and wavelengths.

4.3.6. Schematic illustration of mechanisms

The observed *I–V* characteristics of our device can be explained by schematic energy-band diagrams, as illustrated in Figure 4.24 and Figure 4.25. When the pristine device operates in the dark, a Schottky barrier between Pt and $MAPbI_3$ is present. By applying external bias during the *I–V* measurements, the defect ions can migrate to the interfaces between Pt and $MAPbI_3$, leading to asymmetric Schottky barriers (Figure 4.24a). When incident light is illuminated on the fabricated device, the $MAPbI_3$ film absorbs photons to generate a large number of electrons and holes. Due to the high density of the photogenerated carriers in the $MAPbI_3$ film, the effective Schottky barrier heights are significantly lowered, and thus the photogenerated electrons and holes can be easily transported to the metal contacts without extensive recombination (Figure 4.24b). For the poled device in the dark, the defect ions accumulate at the metal/$MAPbI_3$ interfaces, indicating the formation of *p*-i-*n* homojunctions, which creates V_{bi} in the $MAPbI_3$ film (Figure 4.25a). The poled device shows a lower dark current than the pristine device due to the compensation between V_{ex} and V_{bi}. Similar to the pristine device, the Schottky barriers in the poled device can be reduced under illumination. However, the existing V_{bi} compensates V_{ex}, resulting in a reduction of the photocurrent due to a decrease in the charge collection efficiency (Figure 4.25b). This is in good agreement with our experimental results in Figure 4.19 and with previous reports.[6,15] By measuring the built-in potentials in the $MAPbI_3$ film before and after poling, we identified the transport of photogenerated carriers in the fabricated device, as shown in Figure 4.26. When the pristine device is illuminated without V_{ex}, the photogenerated carriers are almost evenly transported to adjacent Pt electrodes. Thus, V_{bi} is close to zero. For the

poled device, the photogenerated carriers are preferentially transported to one of the adjacent Pt electrodes due to the presence of V_{bi}, resulting in an increase of V_{bi}. It has been reported that photogenerated carriers can create a photovoltage-induced electric field in $MAPbI_3$ films when sufficient incident light illuminates the device.[40] The V_{bi} value gradually decreased under illumination because the photovoltage-induced electric field screens V_{bi}.

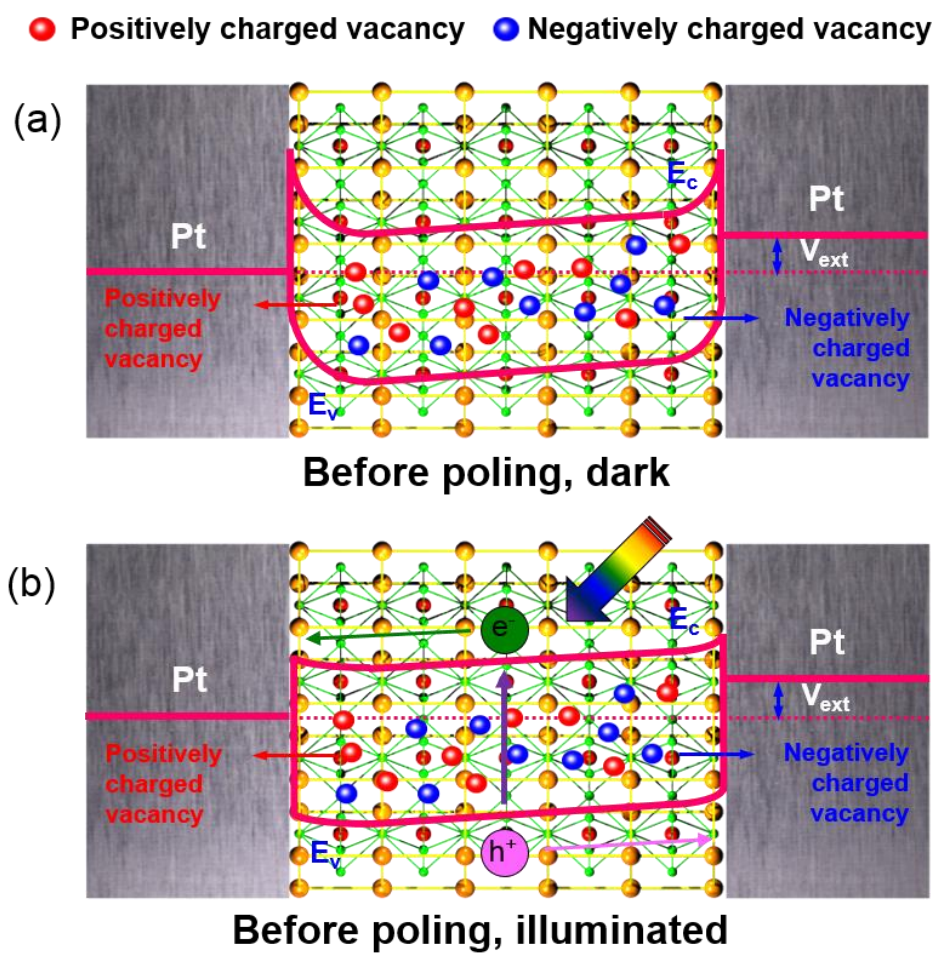

Figure 4.24. Energy-band diagram of $MAPbI_3$-based photodetector (a) before poling in the dark, (b) before poling under illumination. The solid red dots and solid blue dots indicate the positively and negatively charged vacancies, respectively.

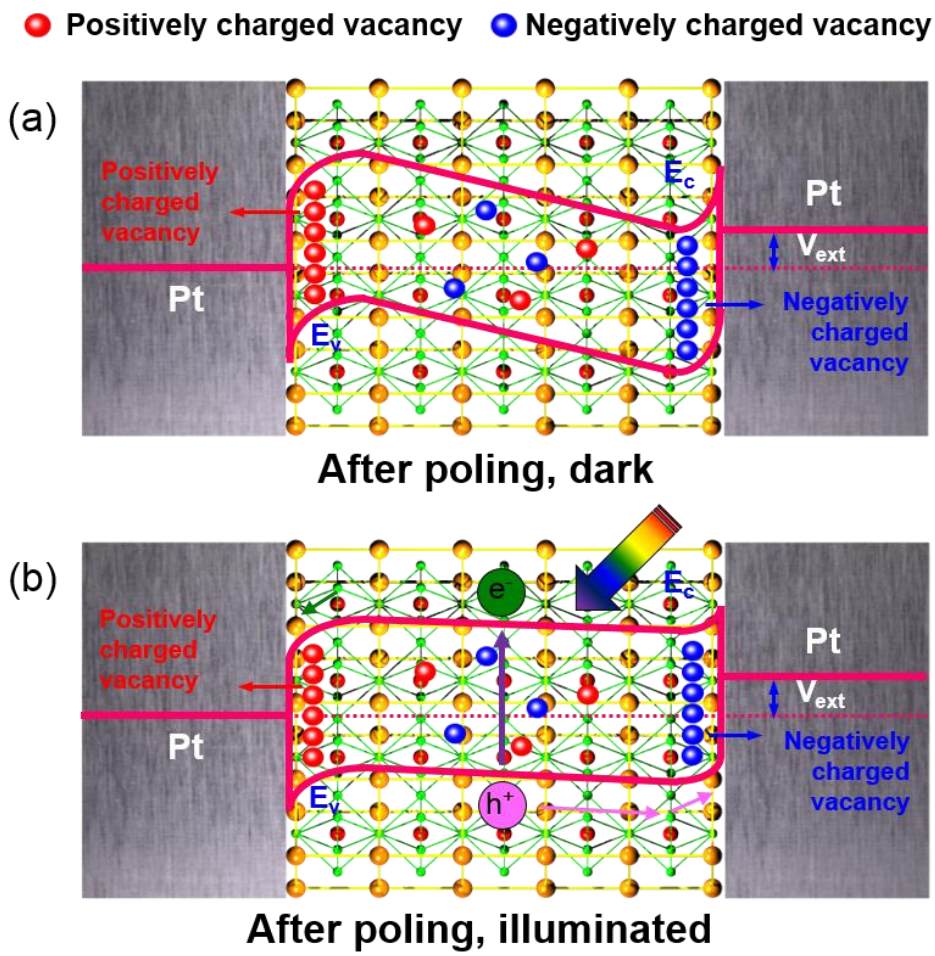

Figure 4.25. Energy-band diagram of $MAPbI_3$-based photodetector (a) After poling in the dark and (b) after poling under illumination. The solid red dots and solid blue dots indicate the positively and negatively charged vacancies, respectively.

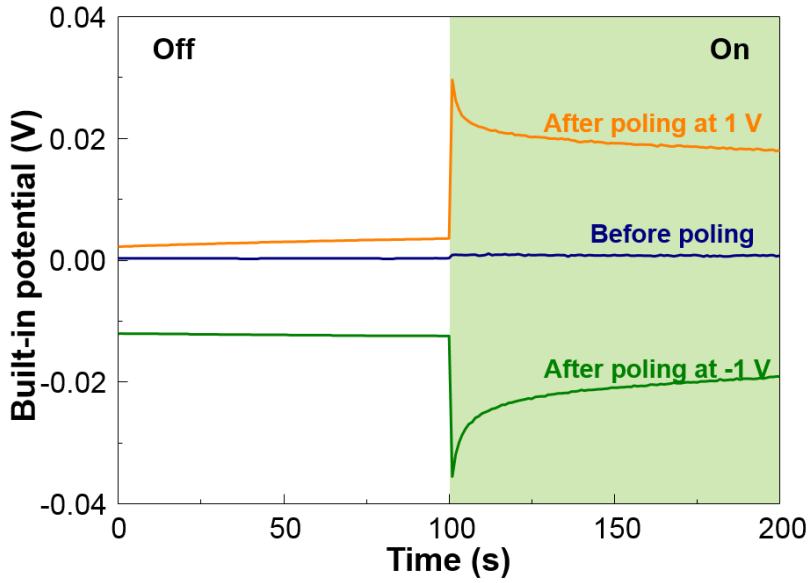

Figure 4.26. Changes of built-in potential in the dark and under illumination.

4.4. Conclusion

In summary, we demonstrated a reliable, high on/off ratio of a $MAPbI_3$-based MSM lateral-structure photodetector via inhibiting the migration of charged defect ions. The photodetector provided a high on/off ratio (~10^4 at V_{ex} of 0.1 V) under the illumination of 5 mW cm^{-2}. By measuring the transient photocurrent with various V_{ex} values, the device showed reliable performance at low V_{ex} that did not trigger remarkable ionic transport. Once the charged defect ions migrated, the device showed poor performance, even operating at low V_{ex}. Inhibiting the migration of charged defect ions in $MAPbI_3$ films is the key factor for acquiring and retaining high device performance. We emphasize that inhibiting charged defect ion migration in $MAPbI_3$ films as described in this work makes it possible to obtain higher device efficiencies in optoelectronics based on $MAPbI_3$ films, where the formation of charged defect ions are energetically favorable, but the defects can be electrically cleaned by controlling the electrical history.

4.5. Reference

[1] K. Deng, L. Li, *Adv. Mater.* **2014**, *26*, 2619.

[2] G. Konstantatos, I. Howard, A. Fischer, S. Hoogland, J. Clifford, E. Klem, L. Levina, E. H. Sargent, *Nature* **2006**, *442*, 180.

[3] Q. Yang, Y. Liu, Z. Li, Z. Yang, X. Wang, Z. L. Wang, *Angew. Chem. Int. Ed.* **2012**, *51*, 6443.

[4] X. Gong, M. Tong, Y. Xia, W. Cai, J. S. Moon, Y. Cao, G. Yu, C.-L. Shieh, B. Nilsson, A. J. Heeger, *Science* **2009**, *325*, 1665.

[5] Y. Jin, J. Wang, B. Sun, J. C. Blakesley, N. C. Greenham, *Nano Lett.* **2008**, *8*, 1649.

[6] X. Hu, X. Z. L. Liang, J. Bao, S. Li, W. Yang, Y. Xie, *Adv. Funct. Mater.* **2014**, *24*, 7373.

[7] R. Dong, Y. Fang, J. Chae, J. Dai, Z. Xiao, Q. Dong, Y. Yuan, A. Centrone, X. C. Zeng, J. Huang, *Adv. Mater.* **2015**, *27*, 1912.

[8] Y. Fang, J. Huang, *Adv. Mater.* **2015**, *27*, 2804.

[9] L. Dou, Y. M. Yang, J. You, Z. Hong, W. Chang, G. Li, Y. Yang, *Nat. Commun.* **2014**, *5*, 5404.

[10] Y. H. Kim, H. Cho, J. H. Heo, T.-S. Kim, N. Myoung, C.-L. Lee, S.H. Im, T.-W. Lee, *Adv. Mater.* **2014**, *27*, 1248.

[11] Q. Hong, Y. Cao, J. Xu, H. Lu, J. He, J.-L. Sun, *ACS Appl. Mater. Interfaces* **2014**, *6*, 20887.

[12] B. S. Passmore, J. Wu, M. O. Manasreh, G. J. Salamo, *Appl. Phys. Lett.* **2007**, *91*, 233508.

[13] M. Buscema, D. J. Groenendijk, S. I. Blanter, G. A. Steele, H. S. J. van der Zant, A. Castellanos-Gomez, *Nano Lett.* **2014**, *14*, 3347.

[14] A. Walsh, D. O. Scanlon, S. Chen, X. G. Gong, S.-H. Wei, *Angew. Chem. Int. Ed.* **2015**, *54*, 1791.

[15] C. Eames, J. M. Frost, P. R. F. Barnes, B. C. O'Regan, A. Walsh, M. S. Islam, *Nat. Commun.* **2015**, *6*, 7497.

[16] J. Xu, A. Buin, A. H. Ip, W. Li, O. Voznyy, R. Comin, M. Yuan, S. Jeon, Z. Ning, J. J. Mcdowell, P. Kanjanaboos, J.-P. Sun, X. Lan, L. N. Quan, D. H. Kim, I. G. Hill, P. Maksymovych, E. H. Sargent, *Nat. Commun.* **2015**, *6*, 7081.

[17] J. M. Frost, K. T. Butler, A. Walsh, *APL Mater.* **2014**, *2*, 081506.

[18] Z. Xiao, Y. Yuan, Y. Shao, Q. Wang, Q. Dong, C. Bi, P. Sharma, A. Gruverman, J. Huang, *Nat. Mater.* **2015**, *14*, 193.

[19] H. J. Snaith, A. Abate, J. M. Ball, G. E. Eperon, T. Leijtens, N. K. Noel, S. D. Stranks, J. T.-W. Wang, K. Wojciechowski, W. Zhang, *J. Phys. Chem. Lett.* **2014**, *5*, 1511.

[20] E. L. Unger, E. T. Hoke, C. D. Bailie, W. H. Nguyen, A. R. Bowring, T. Heumuller, M. G. Christoforo, M. D. McGehee, *Energy Environ. Sci.* **2014**, *7*, 3690.

[21] J. Wei, Y. Zhao, H. Li, G. Li, J. Pan, D. Xu, Q. Zhao, D. Yu, *J. Phys. Chem. Lett.* **2014**, *5*, 3937.

[22] Y. Shao, Z. Xiao, C. Bi, Y. Yuan, J. Huang, *Nat. Commun.* **2014**, *5*, 5784.

[23] W. Tress, N. Marinova, T. Moehl, S. M. Zakeeruddin, M. K. Nazeeruddin,

M. Gratzel, *Energy Environ. Sci.* **2015**, *8*, 995.

[24] H.-S. Kim, N.-G. Park, *J. Phys. Chem. Lett.* **2014**, *5*, 2927.

[25] N. J. Jeon, J. H. Noh, Y. C. Kim, W. S. Yang, S. Ryu, S. I. Seok, *Nat. Mater.* **2014**, *13*, 897.

[26] F. Hao, C. C. Stoumpos, P. Guo, N. Zhou, T. J. Marks, R. P. H. Chang, M. G. Kanatzidis, *J. Am. Chem. Soc.* **2015**, *137*, 11445.

[27] S. Jizhong, X. Leimeng, L. Jianhai, X. Jie, D. Yuhui, L. Xiaoming, Z. Haibo, *Adv. Mater.* **2016**, *28*, 4861.

[28] E. M. Sanehira, A. R. Marshall, J. A. Christians, S. P. Harvey, P. N. Ciesielski, L. M. Wheeler, P. Schulz, L. Y. Lin, M. C. Beard, J. M. Luther, *Sci. Adv.* **2017**, *3*, eaao4204

[29] Y.-H. Kim, C. Wolf, Y.-T. Kim, H. Cho, W. Kwon, S. Do, A. Sadhanala, C. G. Park, S.-W. Rhee, S. H. Im, R. H. Friend, T.-W. Lee, *ACS Nano* **2017**, *11*, 6586.

[30] K. Yang, F. Li, C. P. Veeramalai, T. Guo, Applied Physics Letters, **2017**, *110*, 083102.

[31] P. Liu, X. He, J. Ren, Q. Liao, J. Yao, H. Fu, *ACS Nano* **2017**, *11*, 5766.

[32] O. Malinkiewicz, A. Yella, Y. H. Lee, G. M. Espallargas, M. Graetzel, M. K. Nazeeruddin, H. J. Bolink, *Nat. Photon.* **2013**, *8*, 128.

[33] J. M. Frost, K. T. Butler, F. Brivio, C. H. Hendon, M. van Schilfgaarde, A. Walsh, *Nano Lett.* **2014**, *14*, 2584.

[34] S. Günes, H. Neugebauer, N. S. Sariciftci, *Chem. Rev.* **2007**, *107*, 1324.

[35] S. D. Stranks, G. E. Eperon, G. Grancini, C. Menelaou, M. J. P. Alcocer, T. Leijtens, L. M. Herz, A. Petrozza, H. J. Snaith, *Science* **2013**, 342, 341.

[36] C. Bert, B. Linny, D. D. Christopher, D. H. Jan, M. Jean, B. Hans-Gerd, *Adv. Mater*. **2014**, *26*, 2041.

[37] D. H. Kim, Y.-S. Shim, J.-M. Jeon, H. Y. Jeong, S. S. Park, Y.-W. Kim, J.-S. Kim, J.-H. Lee, H. W. Jang, *ACS Appl. Mater. Interfaces* **2014**, *6*, 14779.

[38] Y.-S. Shim, L. Zhang, D. H. Kim, Y. H. Kim, Y. R. Choi, S. H. Nahm, C.-Y. Kang, W. Lee, H. W. Jang, *Sens. Actuators, B* **2014**, *198*, 294.

[39] S. A. Bretschneider, J. Weickert, J. A. Dorman, L. Schidt-Mende, *APL Mater.* **2014**, *2*, 040701.

[40] C.-H. Lin, C. W. Liu, *Sensors* **2010**, *10*, 8797.

[41] Z. Alaie, S. M. Nejad, M. H. Yousefi, *Mater. Sci. Semicond. Proc.* **2015**, *29*, 16.

[42] K.-J. Baeg, M. Binda, D. Natali, M. Caironi, Y.-Y. Noh, *Adv. Mater.* **2013**, *25*, 4267.

[43] H.-R. Xia, J. Li, W.-T. Sun, L.-M. Peng, *Chem. Commun.* **2014**, *50*, 13695.

[44] Y. Lee, J. Kwon, E. Hwang, C.-H. Ra, W. J. Yoo, J.-H. Ahn, J. H. Park, J. H. Cho, *Adv. Mater.* **2015**, *27*, 41.

[45] Y. Guo, C. Liu, H. Tanaka, E. Nakamura, *J. Phys. Chem. Lett.* **2015**, *6*, 535.

[46] F. Li, C. Ma, H. Wang, W. Hu, A. D. Sheikh, T. Wu, *Nat. Commun.* **2015**, *6*, 8238.

[47] J. J. Yang, M. D. Pickett, X. Li, D. A. A. Ohlberg, D. R. Stewart, R. S. Williams, *Nat. Nanotechnol.* **2008**, *3*, 429.

[48] H. Lim, H. W. Jang, D.-K. Lee, I. Kim, C. S. Hwang, D. S. Jeong, *Nanoscale* **2013**, *5*, 6363.

[49] Y. Deng, Z. Xiao, J. Huang, *Adv. Energy Mater.* **2015**, *5*, 1500721.

Chapter 5

Summary

In this study, the high on/off ratio and reliable performance under the wide range of wavelength from UV to NIR of broadband photodetector have been investigated. By surface functionalization and control of defect migration, broadband photodetection, efficient optoelectronic transfer efficiency, and reliable operation of devices were obtained.

The broadband photodetection by daylight-induced metal-to-insulator transition in surface functionalized VO_2 are demonstrated. We fabricated Ag-decorated porous VO_2 NRs through surface functionalization. The strong electric field at the interface between Ag NPs and VO_2 thin films, which originates from LSPR, causes VO_2 to response to a wide wavelength of incident light, spanning a wide range from 400 nm to 1000 nm. With porous VO_2 NRs, Ag NPs were well distributed throughout the film, so that the strong electric fields at the interface of Ag NPs and VO_2 thin films can affect the entire film to provoke photo-induced MIT in VO_2 NRs. This is the first report on broadband photodetectors based on VO_2 thin films and opens up the way to VO_2 in future optoelectronics.

The reliability and on/off ratio of $MAPbI_3$-based broadband photodetector are improved by control of charged defect migration. The photodetector provided a high on/off ratio ($\approx 10^4$ at V_{ex} of 0.1 V) under the illumination of 5 mW cm^{-2}. By measuring the transient photocurrent with various V_{ex} values, the device showed reliable performance at low V_{ex} that did not trigger remarkable ionic transport. Once the

charged defect ions migrated, the device showed poor performance, even operating at low V_{ex}. Inhibiting the migration of charged defect ions in $MAPbI_3$ films is the key factor for acquiring and retaining high device performance. We emphasize that inhibiting charged defect ion migration in $MAPbI_3$ films as described in this work makes it possible to obtain higher device efficiencies in optoelectronics based on $MAPbI_3$ films, where the formation of charged defect ions are energetically favorable, but the defects can be electrically cleaned by controlling the electrical history.

Our approach to enhance broadband photodetection performance of devices will open up the way to future devices (i) by introducing functional layers or particles on the surface of correlated oxide that affect electronic-electronic interactions in correlated oxide and (ii) by preparing correlated oxide in form of nanostructured thin films to maximize the influence from the functional layer or particles. (iii) by controlling defect migraion in halide perovskies for enhancing optoelectronic transfer efficiency. This study serves as a valuable proof-of-concept for next generation optoelectronic devices with fast response, low power consumption, high performance. and high relibility. I hope my work can provide a solution for further design, and fabrication of optoelectronic device with high on/off ratio and eventually promote the develop of the area.

List of Publications

[1] J. Park, H. Kim, K. Jin, B. J. Lee, Y.-S. Park, H. Kim, I. Park, K. D. Yang, H.-Y. Jeong, J. Kim, **K. T. Hong,** H. W. Jang, K. Kang, K. T. Nam, *J. Am. Chem. Soc.* **2014**, *136*, 4201.

[2] D. H. Kim, D. M. Andoshe, Y.-S. Shim, C.-W. Moon, W. Sohn, S. Choi, T. L. Kim, M. Lee, H. Park, **K. Hong,** K. C. Kwon, J. M. Suh, J.-S. Kim, J.-H. Lee, H. W. Jang, *ACS Appl. Mater. & Interfaces* **2016**, *8*, 23793.

[3] K. C. Kwon, **K. Hong,** Q. V. Le, S. Y. Lee, J. Choi, K.-B. Kim, S. Y. Kim, H. W. Jang, *Adv. Funct. Mater.* **2016**, *26*, 4213.

[4] J. Choi, S. Park, J. Lee, **K. Hong,** K.-H kim, C. W. Moon, G. D. Park, J. M. Suh, J. Hwang, S. Y. Kim, H. S. Jung, M.-G. Park, S. Han, K. T. Nam. H. W. Jang, *Adv. Mater.* **2016**, *28*, 6562.

[5] K. C. Kwon, S. Choi, **K. Hong,** C. W. Moon, Y.-S. Shim, D. H. Kim, T. Kim, W. Sohn, J.-M. Jeon, C.-H. Lee, K. T. Nam, S. Han, S. Y. Kim, H. W. Jang, *Energy & Environ. Sci.* **2016**, *9*, 2240.

[6] Y. G. Kim, K. C. Kwon, Q. V. Le, **K. Hong,** H. W. Jang, S. Y. Kim, *J. Power Sources* **2016**, *319*, 1.

[7] J. Choi, Q. V. Le, **K. Hong,** C. W. Moon, J. S. Han, K. C. Kwon, P.-R. Cha, Y. Kwon, S. Y. Kim, H. W. Jang, *ACS Appl. Mater. & Interfaces* **2017**, *9*, 30764.

[8] J. M. Suh, Y.-S. Shim, D. H. Kim, W. Sohn, Y. Jung, S, Y. Lee, S. Choi, Y. H. Kim, J.-M. Jeon, **K. Hong,** K. C. Kwon, S. Y. Park, C. Kim, J.-H. Lee, C.-Y. Kang, H. W. Jang, *Adv, Mater. Technol.* **2017**, *2*, 1600259.

[9] K. C. Kwon, S. Choi, J. Lee, **K. Hong,** W. Sohn, D. M. Andoshe, K. S. Choi, Y. Kim, S. Han, S. Y. Kim, H. W. Jang, *J. Mater. Chem. A* **2017**, *5*, 15534.

[10] K. C. Kwon, S. Choi, **K. Hong,** D. M. Andoshe, J. M. Suh, C. Kim, K. S. Choi, J. H. Oh, S. Y. Kim, H. W. Jang, *MRS Commun.* **2017**, *7*, 272.

[11] C. W. Moon, S. Y. Lee, W. Sohn, D. M. Andoshe, D. H. Kim, **K. Hong,** and H. W. Jang, *Part. Part. Syst. Charact.* **2017**, *34*, 1600340.

[12] J. S. Han, Q. V. Le, J. Choi, **K. Hong,** C. W. Moon, T. L. Kim, H. Kim, S. Y. Kim and H. W. Jang *Adv. Funct. Mater.* **2018**, *28*, 1705783.

[13] **K. Hong,** T. H. Lee, J. M. Suh, J.-S. Park, H.-S. Kwon, J. Choi, H. W. Jang, *Electron. Mater. Lett.* **2018**, DOI: 10.1007/s13391-018-0066-6.

[14] **K. Hong,** Q. V. Le, S. Y. Kim, H. W. Jang, *J. Mater. Chem. C* **2018**, 6, 2189.

[15] D. M. Andoshe, K. Yim, W. Sohn, C. Kim, T. L. Kim, K. C. Kwon, **K. Hong,** S. Choi, C. W. Moon, S.-P. Hong, S. Han, H. W. Jang, *Appl. Catal., B* **2018**, *234*, 213.

[16] S. B. Kang, K. C. Kwon, K. S. Choi, R. Lee, **K. Hong**, J. M. Suh, M. J. Im, A. Sanger, I. Y. Choi, S. Y. Kim, J. C. Shin, H. W. Jang K. J. Choi, Nano Energy **2018**, 50, 649.

List of Presentation

International:

1. **Kootak Hong**, Seok Hoon Choi, Jaeho Choi, Taemin Kim, and Ho Won Jang, "Substantially enhanced insulator-to-metal transition in self-assembled porous VO_2 thin films with 1-dimensional nanorods", **2014 MRS Spring meeting, San Francisco**, USA (2014)

2. **Kootak Hong**, Seok Hoon Choi, Taemin Kim, and Ho Won Jang, "Substantially enhanced metal-to-insulator transition in self-assembled porous VO_2 thin films with nanorods", **International Nanophotonics and Nanoenergy Conference**, Seoul, Republic of Korea (2014)

3. **Kootak Hong**, Jun Min Suh, Jong-Myeong Jeon, Miyoung Kim, and Ho Won Jang, "Surface Plasmon Induced Broadband Photodetectors based on Ag Decorated VO_2 Nanostructures", 2015 EMRS Spring meeting, Lille, France (2015)

4. **Kootak Hong**, Ki Chang Kwon, Soo Young Kim, and Ho Won Jang, "Inhibition of Ion Migration for Reliable Operation of Hybrid Perovskite-Based Metal/Semiconductor/Metal Broadband Photodetectors" 4^{th} International Conference on Electronic Materials and Nanotechnology for Green Environment (ENGE), Jeju, Republic of Korea (2016)

5. **Kootak Hong**, Ki Chang Kwon, Junmin Suh, Jaeho Choi, and Ho Won Jang, "Inhibition of Ion Migration for Reliable Operation of $CH_3NH_3PbI_3$-Based

Metal/Semiconductor/Metal Broadband Photodetectors" Nano Korea, Ilsan, Republic of Korea (2017)

6. **Kootak Hong**, Junmin Suh, and Ho Won Jang, "Reliable Operation of Hybrid Perovskite-Based Broadband Photodetectors by Suppression of Ion Migration" 2017 MRS Fall meeting, Boston, USA (2017)

Domestic:

1. **Kootak Hong**, Do Hong Kim, Cheon Woo Moon, Migyuong Lee, Jong-Heun Lee, and Ho Won Jang, "Synthesis-in-place of highly ordered hematite nanotube thin films and their applications to chemical sensors", 한국표면공학회 (2014)
2. **Kootak Hong**, Jun Min Suh, Jong-Myeong Jeon, Miyoung Kim, and Ho Won Jang, "Broadband Photodetectors based on Metal-insulator Transition in Ag Decorated VO_2 Nanostructures", 대한금속재료학회 (2015)
3. **Kootak Hong**, Jun Min Suh, and Ho Won Jang, "Surface Plasmon Induced Broadband Photodetectors based on Ag Decorated VO_2 Nanostructured Thin films" 한국공업화학회 (2017)
4. **Kootak Hong**, Jun Min Suh, and Ho Won Jang, "Reliable Operation of Hybrid Perovskite-Based Broadband Photodetectors by Suppression of Ion Migration" 첨단기능재료 학술대회 (2017)

국문 초록

광검출기는 광신호를 전기적 신호로 바꾸는 소자로써, 다양한 분야에서 사용되고 있다. 최근 자외선부터 근적외선 영역 빛의 장점이 (주파수 사용료 무료, 높은 전달 속도와 용량, 인체에 대한 무해성) 부각되면서, 광대역 광검출이 미래 핵심 기술로 부상하고 있다. 하지만, 근적외선 영역까지 빛을 검출하면서 높은 광전자효율과 신뢰성을 보이는 물질의 부재로 고성능 광대역 광검출기 개발에 큰 어려움이 있다. 고성능 광대역 광검출기 소자를 개발하기 위해서, 본 연구에서는 광전자 재료의 표면기능화 및 결함 조절을 통해서 광대역의 빛에 높은 고점멸비, 고신뢰성을 보이는 소자 개발을 진행하였다.

표면기능화 기법을 통해서, 이산화바나듐 (VO_2) 기반 고점멸비 광대역 광검출기를 개발하였다. 은 나노입자로 장식된 이산화바나듐 나노막대들은 (Ag-decorated VO_2 NRs) 표면 플라즈몬 공명 효과의 도움으로 빛에 의해서 금속-절연체 전이 현상을 보이며, 광대역 검출기에 적용한 결과 매우 높은 점멸비와 뛰어난 성능을 보였다. 표면 플라즈몬 공명 현상에 의해서, Ag 나노입자와 VO_2 의 계면에서 강한 전자력 커플링 현상이 나타나고, 이로 인해서 VO_2 에 광유도 금속-절연체 현상이 나타났다. Ag 나노입자와 VO_2 NRs 계면에서 발생되는 표면 플라즈몬 현상은 400 nm~1000 nm 영역의 빛 아래에서 나타나기

때문에 Ag 나노입자로 장식된 VO_2 NRs 고성능 광대역 광검출을 가능하게 한다.

결함 이동 조절을 통해서, 고신뢰성, 고점멸비를 갖는 메틸암모늄납요오드화물 ($CH_3NH_3PbI_3$)기반 광대역 검출기에 대해서 연구를 수행하였다. 높은 인가 전압에서는 $CH_3NH_3PbI_3$기반 소자는 박막 내 결함 이동으로 인해서 낮은 점멸비를 보인다. 결함 이동은 낮은 전압을 인가하는 것으로 효과적으로 방지할 수 있으며, $CH_3NH_3PbI_3$기반 소자는 0.1 V에서 10^4 이상의 높은 점멸비를 보이며 결함 이동으로 인한 성능 저하를 보이지 않았다. 또한, 저전압 인가로 인한 폴링 방지를 통해서 $CH_3NH_3PbI_3$기반 소자의 신호대비잡음비율을 높이고, 약한 세기의 빛도 감지할 수 있었다. 이 결과는 $CH_3NH_3PbI_3$기반 소자의 성능을 향상시키기 위해서 $CH_3NH_3PbI_3$ 박막 내 결함 이동을 최소화 해야 된다는 것을 의미한다.

본 연구에서 사용한 광대역 광검출 소자의 성능 향상 접근 법은 미래 소자 개발하는 방법의 좋은 예시가 될 것이다. 또한, 본 연구 결과는 빠른 응답속도, 저소비전력, 고성능, 고신뢰성을 가지는 차세대 광전자 소자의 개념 증명으로 역할을 수행할 수 있을 것으로 예상된다.

주요어: 광대역 광검출기, 바나듐 이산화물, 금속-절연체 전이현상, 플라즈모닉 나노입자, 표면기능화, 유무기 복합 페로브스카이트, 이온결함 이동, 이력 특성

학번: 2013-20632